Applications of Electrochemically Exfoliated Graphene-based Nanomaterials

By

Omer Sadak

A dissertation submitted in partial fulfillment of

the requirements for the degree of

Doctor of Philosophy

(Materials Science)

at the

UNIVERSITY OF WISCONSIN-MADISON

2019

Date of final oral examination: 05/07/2019

The dissertation is approved by the following members of the Final Oral Committee:
Sundaram Gunasekaran, Professor, Biological System Engineering
Michael S. Arnold, Professor, Materials Science and Engineering
Donald Stone, Professor, Materials Science and Engineering
Lih-sheng Turng, Professor, Mechanical Engineering
Xudong Wang, Professor, Materials Science and Engineering

Acknowledgements

I would like to express my sincere gratitude and appreciation to my supervisor, Prof. Sundaram Gunasekaran, for his continuous support, patience, motivation, and immense knowledge. Dr. Gunasekaran provided me the opportunity to be a part of his research group and provided me freedom to explore new ideas and methods. Without his mentorship and advising, I could not have reached my full potential and abilities for my Ph.D study.

I would like to acknowledge and thank my dissertation committee members: Prof. Michael Arnold, Prof. Xudong Wang, Prof. Donald Stone and Prof. Lih-sheng Turng for reviewing and commenting my thesis which improved my research work and widened my research from various perspectives. I would also like to thank Dr. Ashok K Sundramoorthy, and Dr. MU Anu Prathap, for their scientific advice, insightful comments, encouragement, and knowledge. This thesis cannot be completed without their contributions.

I am also extremely thankful for my former and current colleagues in Dr. Gunasekaran's lab: Drs. Rajesh Seenivasan, Sundaramurthy Anandhakumar, Yuanjie Teng, Yi-Cheng Wang, Lin Lu, Dilek Cokeliler Serdaroğlu, Pelin Onsekizoglu Bagci, Zong Liu, Himan Nourbakhsh, Youngsang You, Sheng Gong, Taeyun Kwon, Kaiyu He, and fellow students and visitors Jiehao Guan, Kari Jordan, Hilary Urena Saborio, Deyler Castilla Caballero, Batul Kachwala, Yaoqi Yin, Weizheng Wang, Bhagya S Premkumar, Dasol Choi, Gozde Kabay, Sercan Dede, Khadija Malik, Farhan Bukhari, and Lala Rukh for their kind support and assistance and I greatly enjoyed their friendship. I am also thankful to undergraduate students Robert Hackney, Haoming Yu, and Qiyuan Chen for their invaluable help. I also greatly benefited from Prof. Sarah Gong's lab during my stay at the University of Wisconsin-Madison. I learned great deal of research and writing skills. I would like to thank Dr. Gong as well as Drs. Goujon Chen, Qifeng Zheng, Srikanth Pilla, Alireza Javadi,

Wenjin Xu, Virendra Gajbhiye, Manju Saraswathy and Yasin Altin for their kind support and assistance.

I am obliged to Republic of Turkey-Ministry of National Education and Office of Education Attaché to The Turkish Consulate General in New York for their financial support during my Ph.D study.

Last but not the least, I would like to acknowledge Professors Abdurrahman Sengul, Ozden Ozel Guven, Sadi Sen, Hulya Arslan, Turkan Kopac, Baki Hazer, Assoc. Professor Hasan Cabuk, Asst. Professors Julide Yener, Taner Erdogan, Fatma Oguz Erdogan, Drs. Ufuk Yildiz, Kadriye Bozgeyik, and Mrs.Halide Isiksungur and Sevil Balpazari for preparing me academic and professional career. Special thanks to Hakan Agac for being a role model for me who unexpectedly passed away in 2011. He will be always remembered in my heart.

Special thanks for my parents, brothers and sisters back in Turkey and England. I am forever indebted to them for their endless support and encouragement throughout my life. I also would like to thank Galip Yilmaz, Firat Yasar, Idris Demirsoy, Amelie Marie, Funda Guven, Tayfun Soysal, Pinar Fedakar, Selami Fedakar, Thevaa Chandereng, Jolene Jaquays, Emily Kr and her family, and all other wonderful friends in Michigan and Wisconsin for their friendship and wonderful times during my stay in the United States.

Finally, I dedicate my Ph.D dissertation to my wife, Zuhal and my three lovely kids: Beril, Demir, and Selen for their never-ending love and support during this study.

Abstract

Graphene (Gr) and its derivates have ignited tremendous research interest for a wide range of applications in the fields of electricity, energy generation and storage, sensors, water purification, medicine and more due to its superior properties. Gr can be prepared from graphite in many ways: mechanical cleavage, chemical exfoliation, thermal decomposition, or electrochemical exfoliation. Among these, electrochemical exfoliation, which is performed without the use of toxic, corrosive oxidizing/reducing agents, is a simple, rapid, and green method to produce graphene flakes. By taking advantage of its unique properties, electrochemically exfoliated graphene (EG)-based nanomaterials were fabricated for energy applications, specifically to be used in supercapacitor.

A free-standing, highly flexible and conductive graphene paper (GrP) was fabricated via a simple, green, and inexpensive method. The fabrication process starts with electrochemical exfoliation of graphite as partially oxidized graphene suspension, which is then vacuum-filtered and air-dried. The thickness of GrP is controlled by adjusting the volume and/or concentration of partially oxidized graphene suspension used for filtration. The procedure does not warrant any binders, toxic and corrosive agents, or high temperature compared to common methods for fabrication of paper-like graphene platforms. The GrP possesses excellent mechanical and electrical properties. The GrP exhibits excellent electrochemical performance and superior capacitance retention compared to other paper-like graphene materials reported in the literature. Moreover, the GrP is an excellent absorbent of oils and organic solvents and is reusable. Therefore, this environmentally friendly GrP fabrication method can be used for large-scale fabrication for applications such as energy-storage devices, flexible/wearable electronics, and removal of oil or toxic organic spills (Chapter II).

In order to improve capacitance behavior of GrP, a pseudocapacitive material, manganese dioxide (MnO_2), was electrochemically deposited on GrP with different number of MnO_2 cycles. After electrochemical deposition process, MnO_2 nanoflowers were formed, which enhanced transfer of electrolyte ions. After 10 cycles of electrodeposition, MnO_2-coated GrP (GrP/10-MnO_2) electrode exhibited an excellent capacitive performance and outstanding cyclic stability. Flexible solid-state supercapacitor made of GrP (negative electrode) and GrP/10-MnO_2 (positive electrode) was tested, which showed outstanding capacitance behavior (Chapter III).

A facile strategy for the fabrication of EG intercalated with polyaniline (PANI) via one-step interfacial polymerization technique on a heterogeneous biphasic system under acidic condition was studied. EG and the PANI formed a uniform nanocomposite with the PANI nanoparticles grafted at the EG surface. Results revealed that the fabricated EG-PANI nanocomposite exhibited a high specific capacitance and good capacity retention after 1000 galvanostatic charge–discharge cycles. A solid-state asymmetrical supercapacitor (SASc) device was fabricated using EG (negative electrode) and EG-PANI (positive electrode), to demonstrate its energy storage application (Chapter IV).

Table of Contents

List of Figures

List of Tables

CHAPTER I

1 Introduction

Graphene (Gr) is monolayer of sp^2 hybridized carbon atoms that bind with each other in 2D hexagonal honeycomb-like structure [1, 2]. The delocalized electrons are freely moving from one side of the plane to the other which generates high electronic conduction [3]. Gr acts as the building block for 0D fullerenes (wrapped up into spherical shape), 1D nanotubes (rolled into a cylindrical shape) or 3D graphite (stacked in layers) as illustrated in **Figure 1.1** [1, 4, 5].

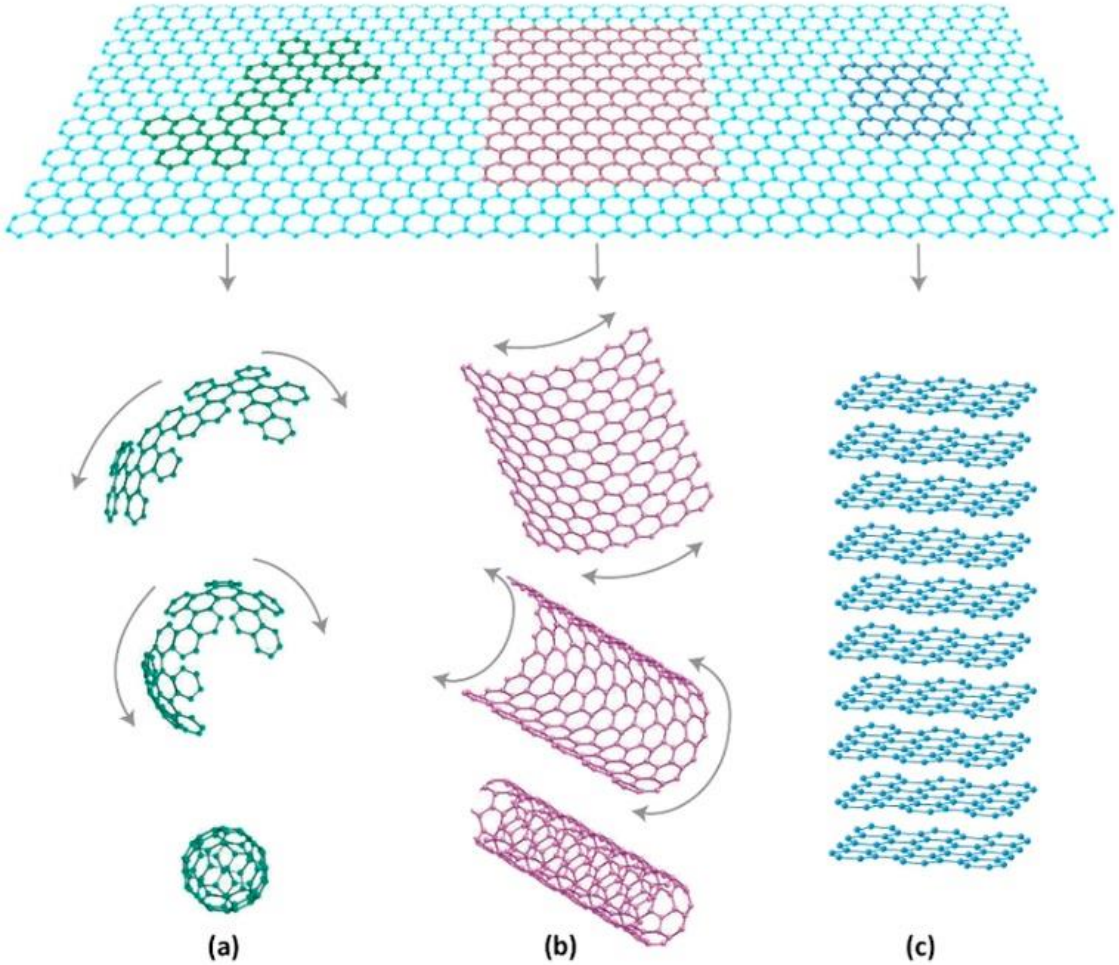

Figure 1.1 Graphitic based nanomaterials. Starting from 2D graphene, other carbon nanomaterials (a) buckyballs, (b) 1D nanotubes or (c) 3D graphite) can be formed [1].

In the last three decades, Gr and its derivatives have ignited increasing research interest in energy storage devices, sensors, electronics, transistors, photonics, and biomedical applications due to high thermal conductivity (~5000 $W\ m^{-1}\ K^{-1}$), high carrier concentration (up to $1\times10^{13}\ cm^{-2}$), outstanding carrier mobility (>20,000 $cm^2\ V^{-1}\ s^{-1}$), large theoretical specific surface area (2630 $m^2\ g^{-1}$), high Young's modulus (~1 TPa), and high optical transmittance (~97.7%) [6, 7]. In addition, Gr is the most used 2D nanomaterial because of its biocompatibility, lightweight, high electrical conductivity, and chemical stability [8, 9].

1.1 History of graphene

Although Gr, single-atom thick plane of sp^2-bonded carbon, was not known until the 1960s, the usage of graphite began with Marica-Karanovo V culture in southern Bulgaria over 6000 years ago to paint and decorate wares [10]. However, the first documented scientific method towards exfoliation of graphite started in 1859 by a professor at the University of Oxford, B.C. Brodie [11]. He mixed graphite with potassium chlorate ($KClO_3$) and solubilized in fumic nitric acid to oxidize the sample, graphite of Ceylon and the water-soluble graphene/graphite oxide turn in to light-yellow color. He noticed an increase in weight and made the elemental analysis which revealed a composition of 60% C, 38% O and 2% H. Then, Brodie's study was improved in 1898 by Staudenmaier with an addition of sulfuric acid (H_2SO_4), and $KClO_3$ [12]. However, both Brodie's and Staudenmaier's methods generate a toxic and potentially explosive vapor, ClO_2. Alternatively, Hummers and Offeman proposed a novel method in 1958 to produce graphite oxide by mixing graphite with concentrated H_2SO_4, sodium nitrate ($NaNO_3$) and potassium permanganate ($KMnO_4$) and then hydrogen peroxide (H_2O_2) was added for further oxidation of graphite [13]. The advantage of this method is to produce graphite oxide in safe operational conditions (no

explosive gases) and get a higher oxidation degree. However, it suffers from excessive use of water, high cost and time-consuming processes such as separation and purification. After the Hummers and Offeman's method, some reports published such as reduction of graphite oxide in 1962, and monolayer of Gr using silicon carbide substrates in 1975 [14]. However, the unique properties of Gr were discovered in 2004 (around 150 years after the discovery of graphite oxide) by researchers at the University of Manchester (Andre Geim and Kostya Novoselov) by isolating single-layer pristine Gr from graphite using a scotch tape [15].

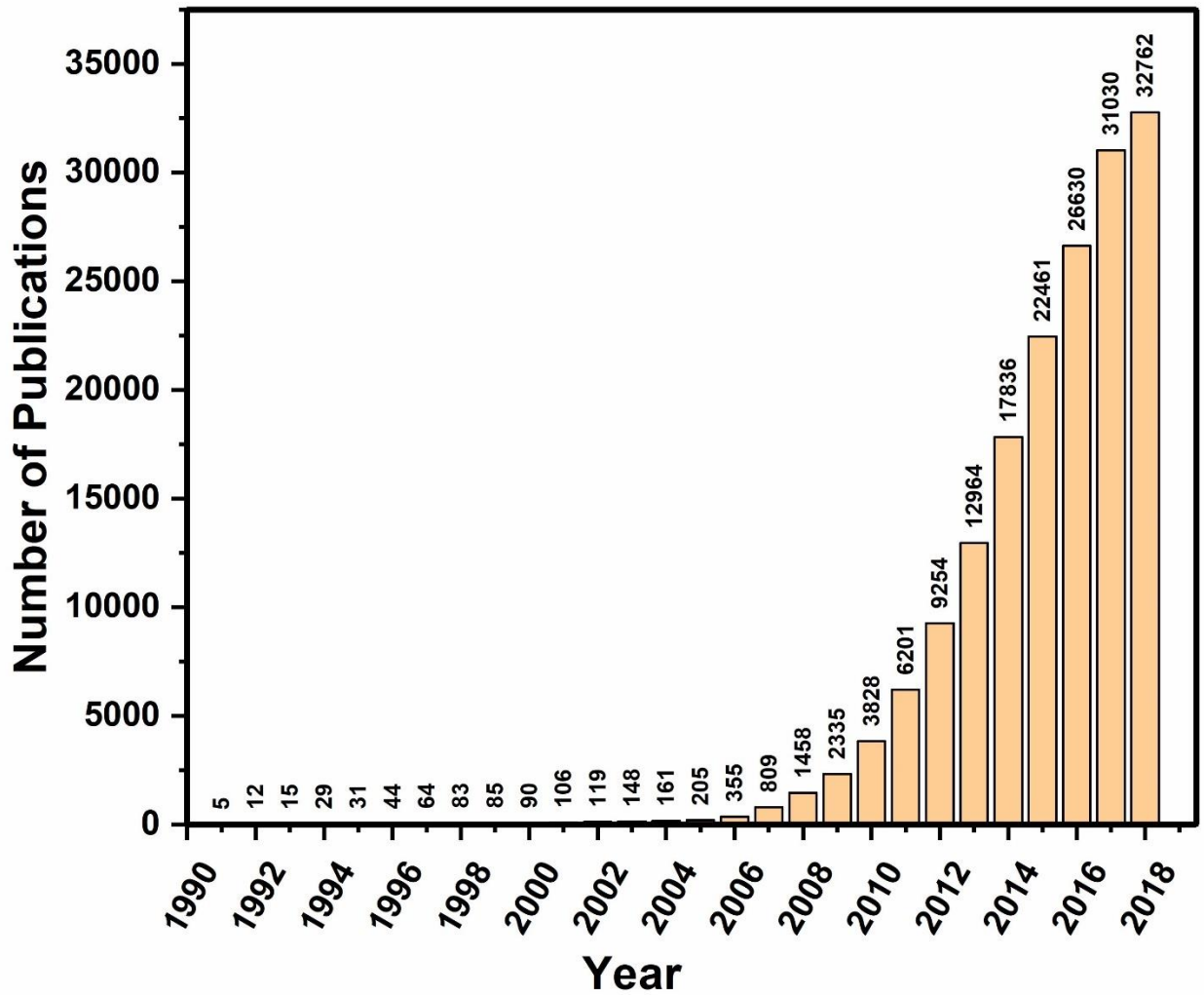

Figure 1.2 Number of academic publications on graphene related research for last 28 years (Source: ISI Web of Knowledge^{SM}, 02/01/19)

This pioneering work regarding two-dimensional atomic crystals was awarded with the Nobel Prize for physics in 2010. Since then, Gr has received the world-wide attention due to its exceptional properties. **Figure 1.2** shows number of graphene-related academic publications from 1990 to 2018 with the keyword 'graphene' (ISI Web of Knowledge^{SM}). As can be seen that there is a dramatic increase after 2004 due to ground breaking experiments of Geim and Novoselov.

1.2 Synthesis approaches for graphene

As illustrated in **Figure *1.3*** graphene can be prepared through top-down and bottom-up approaches [16]. Bottom-up approaches (e.g., chemical vapor deposition (CVD), arc-discharge, epitaxial growth on Silicon carbide (SiC), chemical conversion, reduction of CO, and unzipping carbon nanotubes (CNTs)) consider mainly a chemical production and small molecules as precursors are combined to form various sizes of carbonaceous clusters which condense to form Gr. Due to the small production scale, it is not used widely for industrial production. The starting material for top-down approaches (e.g., micromechanical exfoliation, chemical exfoliation, thermal decomposition and electrochemical exfoliation) is graphite and using physical, chemical, or electrochemical procedures, it can be converted to single layer of Gr. These approaches are widely used in the industry, but the materials that exfoliate graphene from graphite are costly.

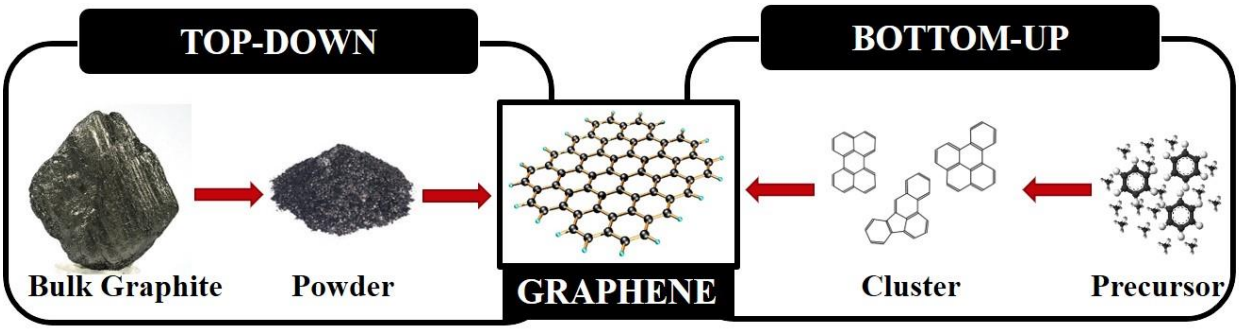

Figure 1.3 Schematic illustration of top-down and bottom-up synthesis approaches for graphene [16]

1.2.1 Bottom-up approaches

Among the bottom-up approaches, CVD is a promising candidate to produce high-quality single- or multi-layer of Gr samples. Gr can be grown on different substrates such as Copper (Cu), Nickel (Ni), Palladium (Pd), Platinum (Pt), Cobalt (Co), Ruthenium (Ru), Iridium (Ir) and Germanium (Ge) and Cu is the one of the most popular metal substrates used in CVD to grow Gr layers because of the low solubility of carbon in Cu [17-19]. Commonly, a chemical etching process is used to remove metal substrate from the synthesized Gr layers and transfer onto a sacrificial substrate such as polymethyl-methacrylate (PMMA) film to prevent them from folding [20].

A typical CVD process shown in **Figure 1.4** consists of several basic components: mass flow controllers (MFC) to provide precursors to the reactor chamber with a necessary flow rate, high temperature tube furnace, a quartz vacuum chamber, and a pressure and vacuum control system [21]. In this process, hydrocarbon sources are transferred into the reaction chamber at the ambient temperatures and as they contact with a heated substrate, carbon atoms dissolve into the substrate to form thin films of carbon precipitates. Upon cooling the substrate, carbon solubility decreases, and carbon atoms diffuse out from thin surface to form graphene film [22].

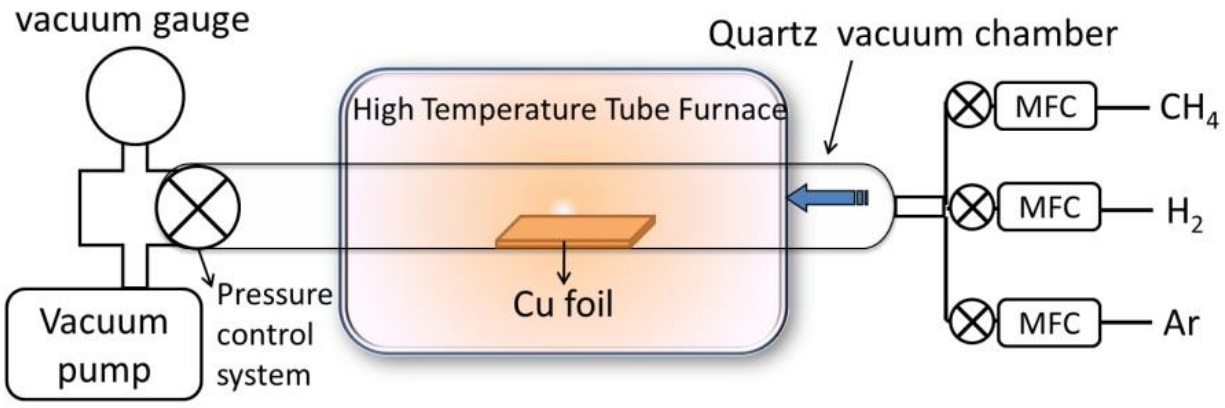

Figure 1.4 Schematic illustration of a common setup for graphene synthesis via CVD method [21].

Epitaxial growth of graphene on SiC by thermal decomposition is another promising bottom-up approach. When SiC crystals are annealed at elevated temperatures in a vacuum, silicon atoms from SiC crystals sublimates and the carbon atoms reconstruct into hexagonal graphene [23]. Epitaxial growth of Gr on SiC has a high potential because direct processing on a wide band gap semiconductor SiC can serve as a substrate for electronic application [24, 25]. However, it suffers from lack of understanding and scalability [26, 27].

The polycyclic aromatic hydrocarbons (PAHs) are considered to be well-defined two-dimensional Gr pieces terminated with hydrogen atoms at the edges which can be formed from either combustion of biomass such as oil, petrol, coal, wood, and other organic materials or as result of anthropogenic activities [28-30]. PAHs are receiving noteworthy attention due to their versatile synthesis nature and substitution of aliphatic chains around the aromatic cores which helps to control their solubility and thermal behaviors [2, 31]. The challenge in synthesizing graphene-like PAHs is preserving dispersibility and a planar morphology [10].

There are several other bottom-up approaches exist with some advantageous and limitations such as arc discharge [32], reduction of carbon monoxide [33], using a template route [34]. For example, using arc discharge method, large amount of high-quality Gr can be produced, but carbonaceous impurities and low yield of production remains the biggest challenge. Likewise, direct reduction of carbon monoxide using Aluminum Sulfide (Al_2S_3) forms good quality of few layers of Gr in large scale, but this method is facing the challenge of high impurities (α-Al_2O_3 particles) on Gr sheets. Despite all efforts made till now, developing a simple bottom-up method to produce single-layer high-grade Gr in large scale is still highly desirable but challenging.

1.2.2 Top-down approaches

Top-down approaches have been widely used to derive Gr by cleaving multi-layer graphite which are held together by weak Van der Waals forces, into single layers via mechanical, chemical, thermal or electrochemical methods [35]. The first method to isolate monolayer Gr achieved via micromechanical exfoliation of highly oriented pyrolytic graphite (HOPG) by Geim and Novoselov in 2004 [15]. This method is also called "scotch tape" or "mechanical cleavage" method [36]. An adhesive tape is applied to peel off thin layer of Gr from HOPG and this process is repeated to eventually give monolayer Gr layers which is transferable to a silicon wafer as illustrated in **Figure 1.5** [37]. The scotch-tape method yields pristine Gr with excellent electrical and physical properties, thus the discovery of single layer of Gr is of great interest [37, 38]. However, the large production of Gr does not seem feasible due to low reproducibility and time consuming and laborious procedure [38, 39]. As a result, this method is used for fundamental studies [35].

A rapid thermal decomposition of graphite or oxidized graphite in liquid medium offers the feasibility of easy scaling up. To reduce the strength of the van der Waals attractions between the graphite layers, intercalation of small molecules such as surfactants, polymers, and organic molecules can be utilized by ultrasonication, which results in graphite intercalation compounds (GICs). GICs comprise of graphite compounds with atoms or small molecules between the layers and since sp^2 hybridized system is distributed, the conductivity decreases [40]. When GICs are treated with a brief heating, it forms few-layer expanded graphite (EG). During to the thermal process gases are evolved due to the removal of intercalated small molecules and reduction of oxidized carbon atoms on graphite sheets [41]. This method can provide EG for a large-scale production with some defects on EG layers.

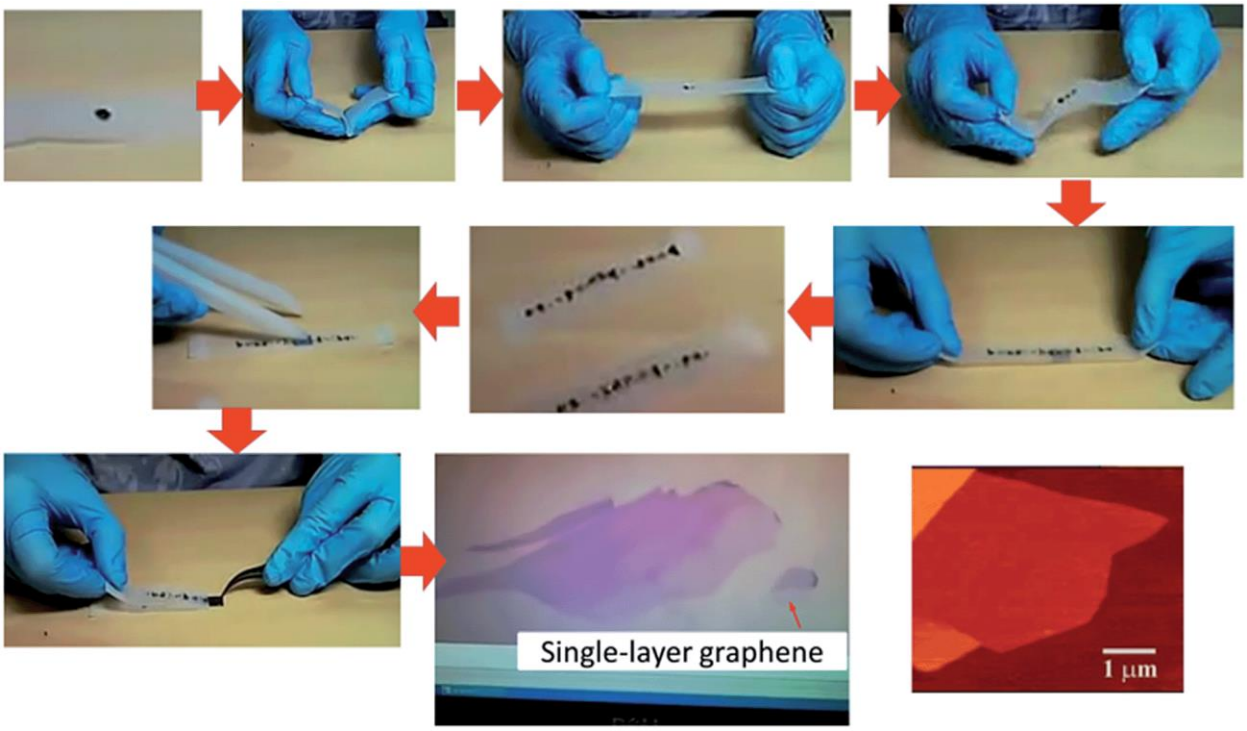

Figure 1.5 Scotch tape method to prepare single layer of graphene from HOPG [37]

To produce Gr in large scale and at low cost, chemical method can be carried out to facilitate the exfoliation of graphite by strong mineral acids and oxidizing agents and followed by subsequent exfoliation [42]. In a typical procedure, chemical species expand the graphite layers and form oxygen containing functional groups on the edge of graphite such as hydroxyl, carbonyl, epoxy, ether and peroxyl [43]. These functional groups facilitate dispersion of chemically exfoliated sheets in aqueous or organic solvents paving the way for high yield of exfoliation [44]. One of the most well-known chemical approaches today is the Hummers method, which relies on mixing concentrated H_2SO_4, $KMnO_4$, $NaNO_3$, and H_2O_2 for a successful oxidation. Many researchers have tried to modify the Hummers method to increase oxidation [45, 46]. As shown in **Figure 1.6**, Hummers method has been improved to eliminate the formation of toxic gases during chemical exfoliation [45]. Gr sheets isolated from Hummers method is called graphene oxide (GO) because

of high oxygen-containing functional groups on graphene sheets. GO, hydrophilic and dispersible in aqueous and other polar solvents, offers great opportunities for large-scale production method for Gr because it can readily form films by spin-coating, spray and drop-casting, or inkjet printing [47, 48]. GO shows unique properties in contrast to pristine graphene: relatively inexpensive, high electrical resistivity due to the oxygen-containing functional groups and sp^3 hybridized carbons and also exhibits high photoluminescence properties due to quantum confinement effect [49]. However, there is still need for improvements for chemical exfoliation method because while reducing the GO via chemical or thermal methods, irreversible lattice defects and significant oxygen groups cause poor electrical and optical behavior such as optical conductivity in contrast to pristine graphene [50].

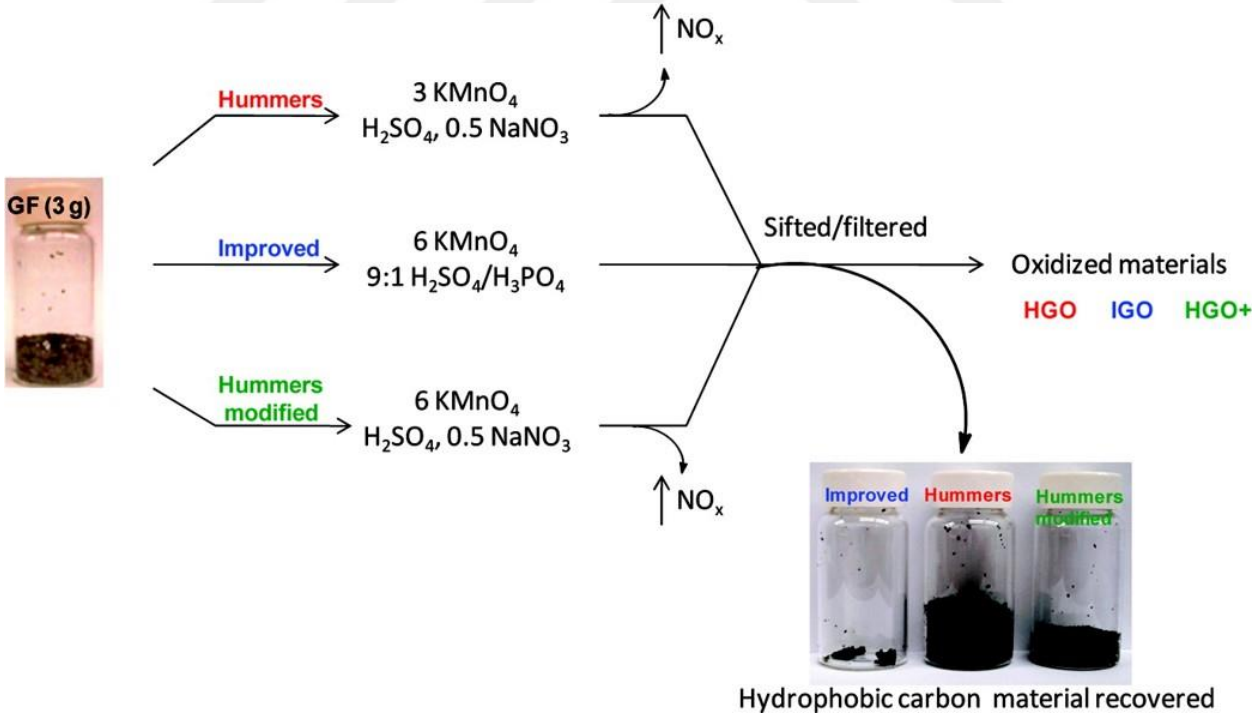

Figure 1.6 Chemical oxidation of graphite flakes (GF) via Hummers, improved Hummers, and modified Hummers methods [45].

Graphene sheets can be also obtained by unzipping CNTs and the synthesized Gr sheets (also called graphene nanoribbons (GNRs)) have open and tunable band gap in contrast to zero-band

gap, semi-metallic Gr [51, 52]. There are several reported methods introduced to unzip CNTs like chemical oxidation with sulfuric acid and potassium permanganate [53]. However, the drawback of chemical oxidation approach is the presence of oxygen-containing functional groups which destroy the quality of GNRs [54]. Beside chemical oxidation approach, variety of methods are described such as electrochemical, microwaves irradiation, electron beam, hydrothermal, plasma etching [51, 55]. Since CNTs are the starting materials, high-quality, low-cost and large-scale production of Gr is still a great challenge [56].

1.3 Principles of electrochemical exfoliation of graphite

Methods for electrochemical exfoliation of graphite are based on the intercalation of oppositely charged ions between graphite layers due to a positive or negative charge in aqueous (acidic or non-acidic) or non-aqueous electrolytes [57]. This method was not known until early 20^{th} century and the first investigation were conducted by Jnioui and co-workers during to early 1980s using concentrated H_2SO_4 as an electrolyte solution [58]. Since then, many studies have been conducted to improve this method to produce high quality Gr at an affordable cost.

1.3.1 Experimental design

A typical experimental setup involves the following: a) graphite-based working electrode, b) reference electrode, c) counter electrode d) electrolyte and e) power supply or potentiostat [59]. Typical graphite-based working electrodes are graphite foil, rod, plate, natural graphite, or HOPG). The working electrode can also be prepared by direct compressing of graphite powders into graphite plates using stainless steel meshwork [60] adhering graphite flakes onto conductive carbon tape [61] or a tungsten wire by a silver pad [62]. The Pt wire, mesh, foil, rod, copper foil

or graphite are commonly used as counter electrodes. The typical experimental arrangement setup is shown in **Figure 1.7**.

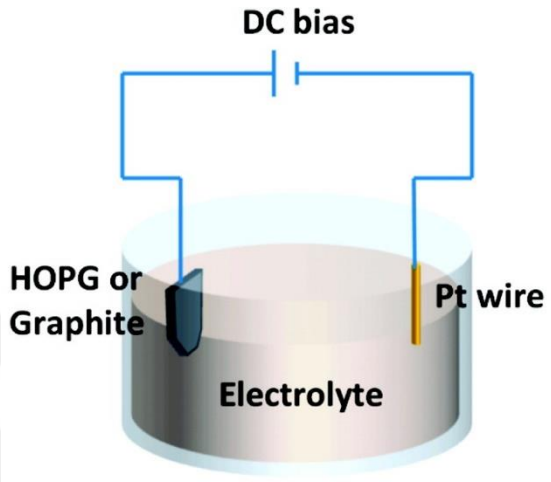

Figure 1.7 Typical experimental setup for the electrochemical exfoliation of graphite [62].

1.3.2 Mechanism

Principally, the mechanism for electrochemical exfoliation of graphite or HOPG is depending on the type of applied potential: cathodic (reduction) or anodic (oxidation) [63]. In **Figure 1.8**, the mechanism for anodic and cathodic exfoliation approaches are summarized [59]. In anodic exfoliation, when positive potential is applied in an electrolysis cell, negatively charged ions (e.g. SO_4^{-2}) are intercalated into anode, expanding the interlayer spacing between graphene sheets. During to expansion process, graphene oxide is produced which contains oxygen rich functional groups and sp^3 defects on graphene sheets [35]. Simultaneously, graphene oxide is exfoliated from graphite matrix. In cathodic exfoliation, when negative potential is applied, positively charged ions (e.g. Li^+) penetrate between graphene sheets, expanding the interlayer space. Compare to anodic expansion, cathodic expansion produces non-oxidized graphene sheets, but it also suffers from

structural defects caused by gas evolution between the layers or intercalation of electrolyte molecules such as sodium dodecyl sulfate (SDS).

After electrochemical process, depending upon applied voltage, type of electrolyte and electrodes used, there may be a need of further exfoliation or removal of graphite-like species to obtain single or few layers of graphene. Ultrasonication treatment is one of the common methods to mechanically exfoliate the electrochemically expanded graphite. Also, centrifugation may be used to remove any large agglomerates.

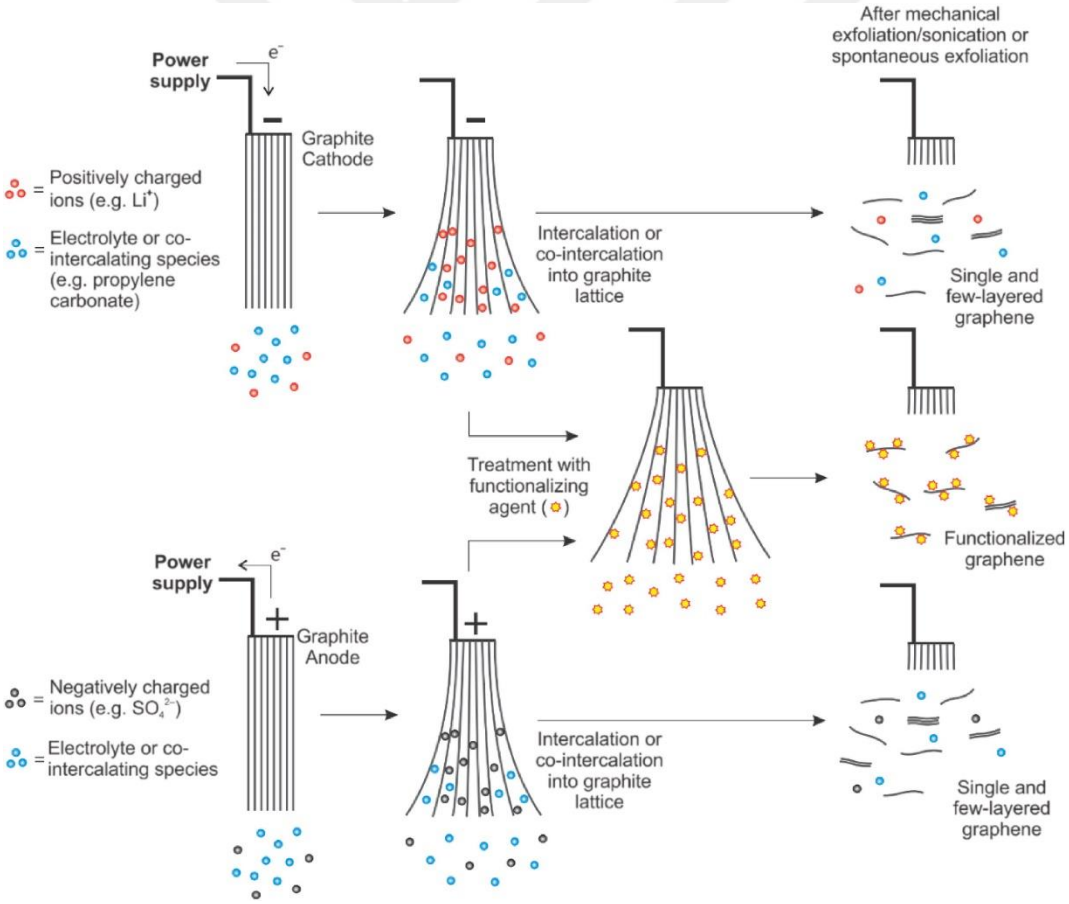

Figure 1.8 Schematic overview of mechanism for anodic and cathodic exfoliation approaches [59].

1.4 Energy Storage

Energy is a vital sustainable development issue all over the world and combustion of fossil fuels to generate energy impact negatively on the environment: emission of greenhouse gases, and acid rains, climate change [64]. Clean and renewal energy is of great interest because it can reduce the use of fossil fuels. Energy conversion/storage systems: rechargeable lithium–ion batteries (LIBs) and electrochemical capacitors play an important role while utilization of renewable energies all over the world. Electrochemical capacitors, also known as supercapacitors (SCs), are energy storage devices that show higher power density than batteries and higher energy density than conventional capacitors as shown in **Figure 1.9** while offering very stable cycling life, fast charging-discharging rate and low cost of fabrication [65-67]. However, SCs require further improvement for their low energy density compared to batteries [68, 69]. Therefore, most of the current research efforts have been focused on developing supercapacitors with a high power and energy density [70, 71].

The charge storage mechanism for SCs can be classified as electric double layer capacitors (EDLCs) or pseudocapacitors. In EDLCs, ions are adsorbed at the interfaces between the electrolyte and porous carbon electrodes (**Figure 1.10a**) [72]. While charging, anions and cations move towards positive and negative electrodes, respectively and the electrons move from the negative electrode to positive electrode [73]. During discharge, electrons, cations and anions move reversely. In contradiction of EDLCs, pseudocapacitors utilize faradaic redox reactions (**Figure 1.10b**). When a potential is applied to a pseudocapacitor, fast and reversible electrochemical reactions happen on the electrode materials which produce charges and as a result, charge transfer across the double layer take place[73, 74].

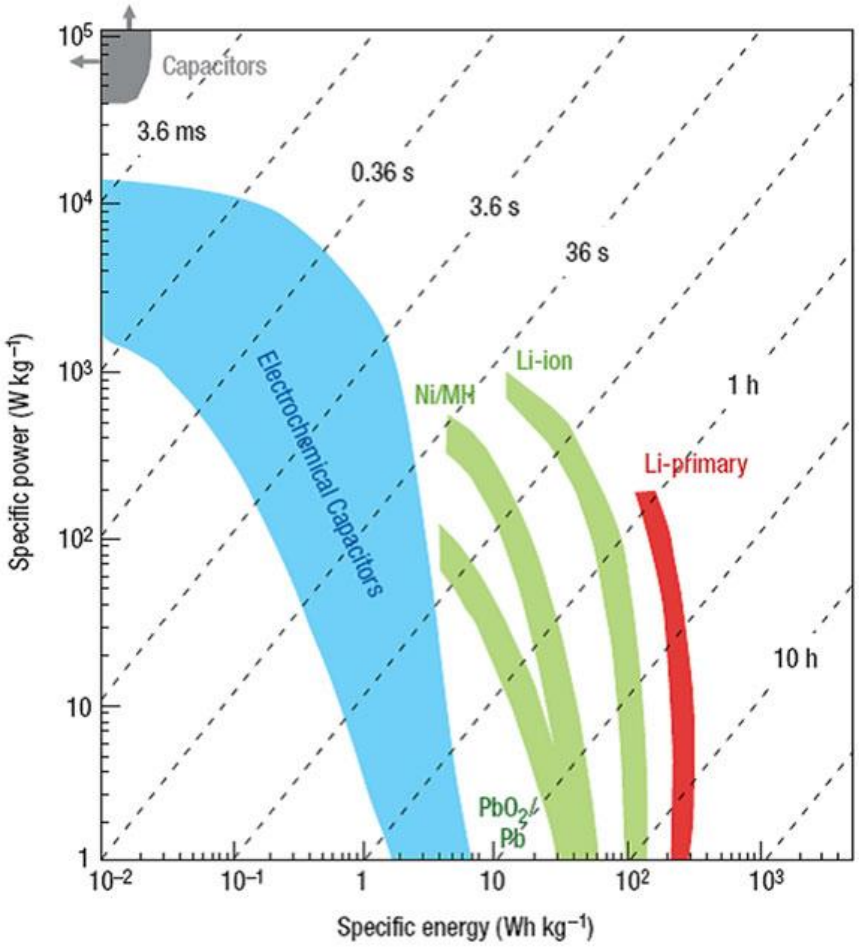

Figure 1.9 Ragone plot for various energy storage devices [67]

The performance of SCs solely depends on its electrode materials and currently, the most common substances for the electrode materials is carbon-based materials, transition metal oxides and the electrically conducting polymers [75, 76]. Carbon-based materials are widely studied due to their ease of fabrication, natural abundance, and high operating temperature range [77]. They may exhibit excellent cycling and electrochemical stability and high power density as supercapacitor electrode materials, but typically possess poor capacitance performance due to the limitation in energy storage mechanism [78, 79]. On the other hand, transition metal oxides as

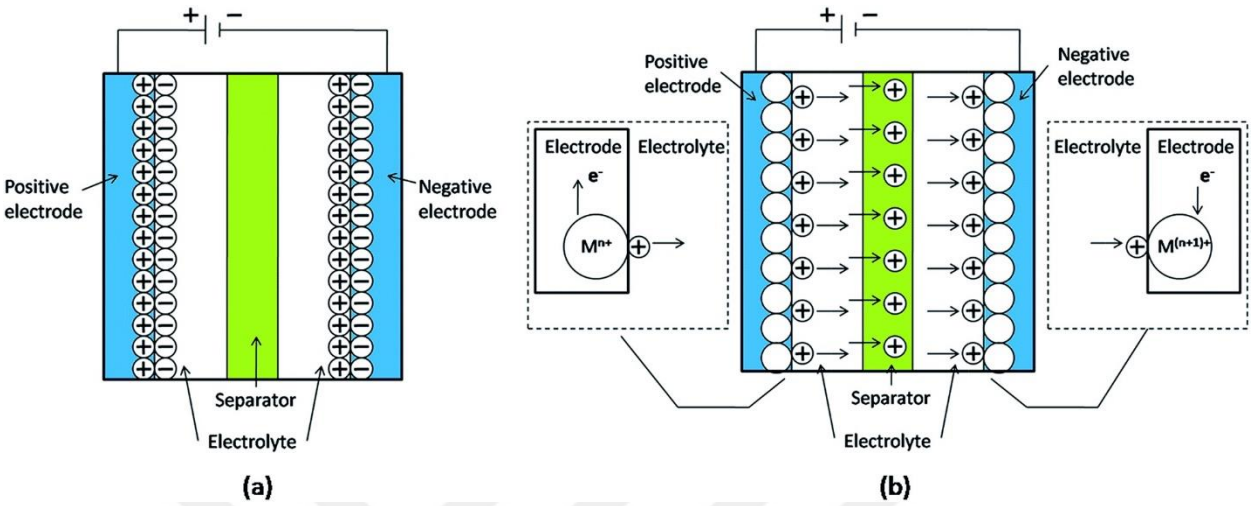

Figure 1.10 Schematic diagram of supercapacitors based on the energy storage mechanism: (a) EDLC, (b) pseudocapacitor [73]

SCs may display excellent specific capacitance due to faradic reaction during to the charge-discharge process; however, they suffer from short cycle life, low conductivity, high cost, toxic nature and the limited natural abundance [75, 80]. Moreover, conducting polymers, such as PANI, polypyrrole (PPy), and poly-3,4-ethlyenedioxythiophene (PEDOT), may show high psuedocapacitive performances, but they also suffer from rate capability [80, 81]. Thus, the most accepted approach to overcome these disadvantages of electrode materials is incorporating highly conductive carbon-based materials with conducting polymers or metal oxides [78, 82].

1.5 References

[1] A.K. Geim, K.S. Novoselov, The rise of graphene, Nat Mater 6(3) (2007) 183-191.
[2] M.J. Allen, V.C. Tung, R.B. Kaner, Honeycomb Carbon: A Review of Graphene, Chem Rev 110(1) (2010) 132-145.
[3] M.Q. Jian, H.H. Xie, K.L. Xia, Y.Y. Zhang, Chapter 15 - Challenge and Opportunities of Carbon Nanotubes, in: H. Peng, Q. Li, T. Chen (Eds.), Industrial Applications of Carbon Nanotubes, Elsevier, Boston, 2017, pp. 433-476.
[4] C. Soldano, A. Mahmood, E. Dujardin, Production, properties and potential of graphene, Carbon 48(8) (2010) 2127-2150.

[5] V. Georgakilas, J.A. Perman, J. Tucek, R. Zboril, Broad Family of Carbon Nanoallotropes: Classification, Chemistry, and Applications of Fullerenes, Carbon Dots, Nanotubes, Graphene, Nanodiamonds, and Combined Superstructures, Chem Rev 115(11) (2015) 4744-4822.
[6] A.C.H. Tsang, H.Y.H. Kwok, D.Y.C. Leung, The use of graphene based materials for fuel cell, photovoltaics, and supercapacitor electrode materials, Solid State Sci 67 (2017) A1-A14.
[7] M. Wang, X.D. Duan, Y.X. Xu, X.F. Duan, Functional Three-Dimensional Graphene/Polymer Composites, Acs Nano 10(8) (2016) 7231-7247.
[8] H. Amani, E. Mostafavi, H. Arzaghi, S. Davaran, A. Akbarzadeh, O. Akhavan, H. Pazoki-Toroudi, T.J. Webster, Three-Dimensional Graphene Foams: Synthesis, Properties, Biocompatibility, Biodegradability, and Applications in Tissue Engineering, ACS Biomaterials Science & Engineering 5(1) (2019) 193-214.
[9] A. Nieto, R. Dua, C. Zhang, B. Boesl, S. Ramaswamy, A. Agarwal, Three Dimensional Graphene Foam/Polymer Hybrid as a High Strength Biocompatible Scaffold, Adv Funct Mater 25(25) (2015) 3916-3924.
[10] V. Singh, D. Joung, L. Zhai, S. Das, S.I. Khondaker, S. Seal, Graphene based materials: Past, present and future, Prog Mater Sci 56(8) (2011) 1178-1271.
[11] C. Brodie Benjamin, XIII. On the atomic weight of graphite, Philosophical Transactions of the Royal Society of London 149 (1859) 249-259.
[12] L. Staudenmaier, Verfahren zur Darstellung der Graphitsäure, Berichte der deutschen chemischen Gesellschaft 31(2) (1898) 1481-1487.
[13] W.S. Hummers, R.E. Offeman, Preparation of Graphitic Oxide, Journal of the American Chemical Society 80(6) (1958) 1339-1339.
[14] D.R. Dreyer, S. Park, C.W. Bielawski, R.S. Ruoff, The chemistry of graphene oxide, Chem Soc Rev 39(1) (2010) 228-240.
[15] K.S. Novoselov, A.K. Geim, S.V. Morozov, D. Jiang, Y. Zhang, S.V. Dubonos, I.V. Grigorieva, A.A. Firsov, Electric field effect in atomically thin carbon films, Science 306(5696) (2004) 666-669.
[16] D.A.C. Brownson, C.E. Banks, Graphene electrochemistry: an overview of potential applications, Analyst 135(11) (2010) 2768-2778.
[17] P. Li, Z.Y. Li, J.L. Yang, Dominant Kinetic Pathways of Graphene Growth in Chemical Vapor Deposition: The Role of Hydrogen, J Phys Chem C 121(46) (2017) 25949-25955.
[18] B. Kiraly, R.M. Jacobberger, A.J. Mannix, G.P. Campbell, M.J. Bedzyk, M.S. Arnold, M.C. Hersam, N.P. Guisinger, Electronic and Mechanical Properties of Graphene-Germanium Interfaces Grown by Chemical Vapor Deposition, Nano Lett 15(11) (2015) 7414-7420.
[19] I. Pasternak, M. Wesolowski, I. Jozwik, M. Lukosius, G. Lupina, P. Dabrowski, J.M. Baranowski, W. Strupinski, Graphene growth on Ge(100)/Si(100) substrates by CVD method, Sci Rep-Uk 6 (2016).
[20] H.V. Ngoc, Y. Qian, S.K. Han, D.J. Kang, PMMA-Etching-Free Transfer of Wafer-scale Chemical Vapor Deposition Two-dimensional Atomic Crystal by a Water Soluble Polyvinyl Alcohol Polymer Method, Sci Rep-Uk 6 (2016).
[21] A. Kumar, C.H. Lee, Synthesis and Biomedical Applications of Graphene: Present and Future Trends, Advances in Graphene Science, , IntechOpen (2013).
[22] Y. Zhang, L.Y. Zhang, C.W. Zhou, Review of Chemical Vapor Deposition of Graphene and Related Applications, Accounts Chem Res 46(10) (2013) 2329-2339.
[23] X.Z. Yu, C.G. Hwang, C.M. Jozwiak, A. Kohl, A.K. Schmid, A. Lanzara, New synthesis method for the growth of epitaxial graphene, J Electron Spectrosc 184(3-6) (2011) 100-106.
[24] H. Hibino, S. Tanabe, S. Mizuno, H. Kageshima, Growth and electronic transport properties of epitaxial graphene on SiC, Journal of Physics D: Applied Physics 45(15) (2012) 154008.

[25] M. Kruskopf, D.M. Pakdehi, K. Pierz, S. Wundrack, R. Stosch, T. Dziomba, M. Gotz, J. Baringhaus, J. Aprojanz, C. Tegenkamp, J. Lidzba, T. Seyller, F. Hohls, F.J. Ahlers, H.W. Schumacher, Comeback of epitaxial graphene for electronics: large-area growth of bilayer-free graphene on SiC, 2d Mater 3(4) (2016).
[26] K.E. Whitener, P.E. Sheehan, Graphene synthesis, Diamond and Related Materials 46 (2014) 25-34.
[27] R.K.G. Prithu Mukhopadhyay, Graphite, Graphene, and Their Polymer Nanocomposites, CRC Press2012.
[28] H.I. Abdel-Shafy, M.S.M. Mansour, A review on polycyclic aromatic hydrocarbons: Source, environmental impact, effect on human health and remediation, Egyptian Journal of Petroleum 25(1) (2016) 107-123.
[29] S.D. Chakarova-Kack, A. Vojvodic, J. Kleis, P. Hyldgaard, E. Schroder, Binding of polycyclic aromatic hydrocarbons and graphene dimers in density functional theory, New J Phys 12 (2010).
[30] F. Dotz, J.D. Brand, S. Ito, L. Gherghel, K. Mullen, Synthesis of large polycyclic aromatic hydrocarbons: Variation of size and periphery, Journal of the American Chemical Society 122(32) (2000) 7707-7717.
[31] J.S. Wu, W. Pisula, K. Mullen, Graphenes as potential material for electronics, Chem Rev 107(3) (2007) 718-747.
[32] Z.S. Wu, W.C. Ren, L.B. Gao, J.P. Zhao, Z.P. Chen, B.L. Liu, D.M. Tang, B. Yu, C.B. Jiang, H.M. Cheng, Synthesis of Graphene Sheets with High Electrical Conductivity and Good Thermal Stability by Hydrogen Arc Discharge Exfoliation, Acs Nano 3(2) (2009) 411-417.
[33] C.D. Kim, B.K. Min, W.S. Jung, Preparation of graphene sheets by the reduction of carbon monoxide, Carbon 47(6) (2009) 1610-1612.
[34] W.X. Zhang, J.C. Cui, C.A. Tao, Y.G. Wu, Z.P. Li, L. Ma, Y.Q. Wen, G.T. Li, A Strategy for Producing Pure Single-Layer Graphene Sheets Based on a Confined Self-Assembly Approach, Angew Chem Int Edit 48(32) (2009) 5864-5868.
[35] A. Ambrosi, C.K. Chua, A. Bonanni, M. Pumera, Electrochemistry of Graphene and Related Materials, Chem Rev 114(14) (2014) 7150-7188.
[36] S.S. Shams, R.Y. Zhang, J. Zhu, Graphene synthesis: a Review, Mater Sci-Poland 33(3) (2015) 566-578.
[37] M. Yi, Z.G. Shen, A review on mechanical exfoliation for the scalable production of graphene, J Mater Chem A 3(22) (2015) 11700-11715.
[38] E.P. Randviir, D.A.C. Brownson, C.E. Banks, A decade of graphene research: production, applications and outlook, Mater Today 17(9) (2014) 426-432.
[39] M. Khan, M.N. Tahir, S.F. Adil, H.U. Khan, M.R.H. Siddiqui, A.A. Al-warthan, W. Tremel, Graphene based metal and metal oxide nanocomposites: synthesis, properties and their applications, J Mater Chem A 3(37) (2015) 18753-18808.
[40] M.Z. Cai, D. Thorpe, D.H. Adamson, H.C. Schniepp, Methods of graphite exfoliation, J Mater Chem 22(48) (2012) 24992-25002.
[41] G. Carotenuto, A. Longo, L. Nicolais, S. De Nicola, E. Pugliese, M. Ciofini, M. Locatelli, A. Lapucci, R. Meucci, Laser-Induced Thermal Expansion of H2SO4-Intercalated Graphite Lattice, J Phys Chem C 119(28) (2015) 15942-15947.
[42] C.C. Wang, Y.Y. Zhao, H.Y. Ge, R.S. Qian, Enhanced Mechanical and Thermal Properties of Short Carbon Fiber Reinforced Polypropylene Composites by Graphene Oxide, Polym Composite 39(2) (2018) 405-413.
[43] X.J. Qi, W.W. Song, J.W. Shi, Density functional theory study the effects of oxygen-containing functional groups on oxygen molecules and oxygen atoms adsorbed on carbonaceous materials, Plos One 12(3) (2017).

[44] A.J. Cooper, N.R. Wilson, I.A. Kinloch, R.A.W. Dryfe, Single stage electrochemical exfoliation method for the production of few-layer graphene via intercalation of tetraalkylammonium cations, Carbon 66 (2014) 340-350.
[45] D.C. Marcano, D.V. Kosynkin, J.M. Berlin, A. Sinitskii, Z.Z. Sun, A. Slesarev, L.B. Alemany, W. Lu, J.M. Tour, Improved Synthesis of Graphene Oxide, Acs Nano 4(8) (2010) 4806-4814.
[46] L.F. Lai, L.W. Chen, D. Zhan, L. Sun, J.P. Liu, S.H. Lim, C.K. Poh, Z.X. Shen, J.Y. Lin, One-step synthesis of NH2-graphene from in situ graphene-oxide reduction and its improved electrochemical properties, Carbon 49(10) (2011) 3250-3257.
[47] F. Lin, X. Tong, Y.A. Wang, J.M. Bao, Z.M.M. Wang, Graphene oxide liquid crystals: synthesis, phase transition, rheological property, and applications in optoelectronics and display, Nanoscale Res Lett 10 (2015).
[48] S. Wang, P.K. Ang, Z.Q. Wang, A.L.L. Tang, J.T.L. Thong, K.P. Loh, High Mobility, Printable, and Solution-Processed Graphene Electronics, Nano Lett 10(1) (2010) 92-98.
[49] D. Lee, J. Seo, X. Zhu, J. Lee, H.J. Shin, J.M. Cole, T.H. Shin, J. Lee, H. Lee, H.B. Su, Quantum confinement-induced tunable exciton states in graphene oxide, Sci Rep-Uk 3 (2013).
[50] J. Wei, T. Vo, F. Inam, Epoxy/graphene nanocomposites – processing and properties: a review, Rsc Adv 5(90) (2015) 73510-73524.
[51] P. Kumar, S.S.R.K.C. Yamijala, S.K. Pati, Optical Unzipping of Carbon Nanotubes in Liquid Media, J Phys Chem C 120(30) (2016) 16985-16993.
[52] A. Narita, Z.P. Chen, Q. Chen, K. Mullen, Solution and on-surface synthesis of structurally defined graphene nanoribbons as a new family of semiconductors, Chem Sci 10(4) (2019) 964-975.
[53] T.T. Zhang, S. Wu, R. Yang, G.Y. Zhang, Graphene: Nanostructure engineering and applications, Front Phys-Beijing 12(1) (2017).
[54] S. Mondal, S. Ghosh, C.R. Raj, Unzipping of Single-Walled Carbon Nanotube for the Development of Electrocatalytically Active Hybrid Catalyst of Graphitic Carbon and Pd Nanoparticles, Acs Omega 3(1) (2018) 622-630.
[55] I. Janowska, O. Ersen, T. Jacob, P. Vennegues, D. Begin, M.J. Ledoux, C. Pham-Huu, Catalytic unzipping of carbon nanotubes to few-layer graphene sheets under microwaves irradiation, Appl Catal a-Gen 371(1-2) (2009) 22-30.
[56] R. Thomas, K.P.S.S. Hembram, B.V.M. Kumar, G.M. Rao, High density oxidative plasma unzipping of multiwall carbon nanotubes, Rsc Adv 7(76) (2017) 48268-48274.
[57] J.M. Munuera, J.I. Paredes, M. Enterria, A. Pagan, S. Villar-Rodil, M.F.R. Pereira, J.I. Martins, J.L. Figueiredo, J.L. Cenis, A. Martinez-Alonso, J.M.D. Tascon, Electrochemical Exfoliation of Graphite in Aqueous Sodium Halide Electrolytes toward Low Oxygen Content Graphene for Energy and Environmental Applications, Acs Appl Mater Inter 9(28) (2017) 24085-24099.
[58] A. Jnioui, A. Metrot, A. Storck, Electrochemical production of graphite salts using a three-dimensional electrode of graphite particles, Electrochimica Acta 27(9) (1982) 1247-1252.
[59] P. Yu, S.E. Lowe, G.P. Simon, Y.L. Zhong, Electrochemical exfoliation of graphite and production of functional graphene, Curr Opin Colloid In 20(5-6) (2015) 329-338.
[60] M. Mao, M.M. Wang, J.Y. Hu, G. Lei, S.Z. Chen, H.T. Liu, Simultaneous electrochemical synthesis of few-layer graphene flakes on both electrodes in protic ionic liquids, Chem Commun 49(46) (2013) 5301-5303.
[61] K. Parvez, Z.S. Wu, R.J. Li, X.J. Liu, R. Graf, X.L. Feng, K. Mullen, Exfoliation of Graphite into Graphene in Aqueous Solutions of Inorganic Salts, Journal of the American Chemical Society 136(16) (2014) 6083-6091.

[62] C.Y. Su, A.Y. Lu, Y.P. Xu, F.R. Chen, A.N. Khlobystov, L.J. Li, High-Quality Thin Graphene Films from Fast Electrochemical Exfoliation, Acs Nano 5(3) (2011) 2332-2339.
[63] Y.C. Yang, H.S. Hou, G.Q. Zou, W. Shi, H.L. Shuai, J.Y. Li, X.B. Ji, Electrochemical exfoliation of graphene-like two-dimensional nanomaterials, Nanoscale 11(1) (2019) 16-33.
[64] C. Zhao, W. Zheng, A Review for Aqueous Electrochemical Supercapacitors, Frontiers in Energy Research 3(23) (2015).
[65] V.S. Kumbhar, M.H. Cho, J. Lee, W.K. Kim, M. Lee, Y.R. Lee, J.J. Shim, Electrosynthesis of a corn flake-like NiO nanostructure on nickel foam for polymer gel electrolyte-based high performance asymmetric supercapacitors, New J Chem 41(19) (2017) 10584-10591.
[66] S. Wang, S.M. Sun, S.D. Li, F.L. Gong, Y.N. Li, Q. Wu, P. Song, S.M. Fang, P.Y. Wang, Time and temperature dependent multiple hierarchical NiCo2O4 for high-performance supercapacitors, Dalton T 45(17) (2016) 7469-7475.
[67] P. Simon, Y. Gogotsi, Materials for electrochemical capacitors, Nat Mater 7 (2008) 845.
[68] U.M. Patil, M.S. Nam, S. Kang, J.S. Sohn, H.B. Sim, S. Kang, S.C. Jun, Fabrication of ultra-high energy and power asymmetric supercapacitors based on hybrid 2D MoS2/graphene oxide composite electrodes: a binder-free approach, Rsc Advances 6(49) (2016) 43261-43271.
[69] A. Borenstein, O. Hanna, R. Attias, S. Luski, T. Brousse, D. Aurbach, Carbon-based composite materials for supercapacitor electrodes: a review, J Mater Chem A 5(25) (2017) 12653-12672.
[70] W.D. He, C.G. Wang, F.W. Zhuge, X.L. Deng, X.J. Xu, T.Y. Zhai, Flexible and high energy density asymmetrical supercapacitors based on core/shell conducting polymer nanowires/manganese dioxide nanoflakes, Nano Energy 35 (2017) 242-250.
[71] L. Li, X. Zhang, J.J. Qiu, B.L. Weeks, S.R. Wang, Reduced graphene oxide-linked stacked polymer forests for high energy-density supercapacitor, Nano Energy 2(5) (2013) 628-635.
[72] D. Kim, G. Lee, D. Kim, J. Yun, S.S. Lee, J.S. Ha, High performance flexible double-sided micro-supercapacitors with an organic gel electrolyte containing a redox-active additive, Nanoscale 8(34) (2016) 15611-15620.
[73] F. Shi, L. Li, X.L. Wang, C.D. Gu, J.P. Tu, Metal oxide/hydroxide-based materials for supercapacitors, Rsc Adv 4(79) (2014) 41910-41921.
[74] G.P. Wang, L. Zhang, J.J. Zhang, A review of electrode materials for electrochemical supercapacitors, Chem Soc Rev 41(2) (2012) 797-828.
[75] Q.H. Wang, L.F. Jiao, H.M. Du, Y.C. Si, Y.J. Wang, H.T. Yuan, Co3S4 hollow nanospheres grown on graphene as advanced electrode materials for supercapacitors, J Mater Chem 22(40) (2012) 21387-21391.
[76] S. Bose, T. Kuila, A.K. Mishra, R. Rajasekar, N.H. Kim, J.H. Lee, Carbon-based nanostructured materials and their composites as supercapacitor electrodes, J Mater Chem 22(3) (2012) 767-784.
[77] D.M. El-Gendy, N.A.A. Ghany, E.E.F. El Sherbini, N.K. Allam, Adenine-functionalized Spongy Graphene for Green and High-Performance Supercapacitors, Sci Rep-Uk 7 (2017).
[78] L.L. Zhang, D. Huang, N.T. Hu, C. Yang, M. Li, H. Wei, Z. Yang, Y.J. Su, Y.F. Zhang, Three-dimensional structures of graphene/polyaniline hybrid films constructed by steamed water for high-performance supercapacitors, J Power Sources 342 (2017) 1-8.
[79] H.H. Wang, J.Y. Lin, Z.X. Shen, Polyaniline (PANi) based electrode materials for energy storage and conversion, J Sci 1(3) (2016) 225-255.
[80] Y. Yang, Y.L. Xi, J.Z. Li, G.D. Wei, N.I. Klyui, W. Han, Flexible Supercapacitors Based on Polyaniline Arrays Coated Graphene Aerogel Electrodes, Nanoscale Res Lett 12 (2017).
[81] N.T. Hu, L.L. Zhang, C. Yang, J. Zhao, Z. Yang, H. Wei, H.B. Liao, Z.X. Feng, A. Fisher, Y.F. Zhang, Z.J. Xu, Three-dimensional skeleton networks of graphene wrapped polyaniline nanofibers: an excellent structure for high-performance flexible solid-state supercapacitors, Sci Rep-Uk 6 (2016).

[82] L.Q. Wu, L.H. Hao, B.W. Pang, G.F. Wang, Y. Zhang, X.H. Li, MnO2 nanoflowers and polyaniline nanoribbons grown on hybrid graphene/Ni 3D scaffolds by in situ electrochemical techniques for high-performance asymmetric supercapacitors, J Mater Chem A 5(9) (2017) 4629-4637.

CHAPTER II

2 Facile and Green Synthesis of Highly Conductive Graphene Paper *

2.1 Introduction

Graphene, a single layer of carbon atoms in a honeycomb lattice, is an exceptional material owing to its high thermal conductivity (~5000 W m^{-1} K^{-1}), large theoretical specific surface area (2630 m^2 g^{-1}), high carrier concentration (up to 10^{13} cm^{-2}) and mobility (over 10^4 cm^2 V^{-1} s^{-1}), high Young's modulus (~1 TPa), and inherent hydrophobicity [1-4]. Its lightweight, high electrical conductivity, and chemical stability make graphene a promising candidate for electrode materials for flexible and wearable electronics, energy-related devices, absorbents for oil and organic solvents etc. [5-9]. Graphene can be prepared from graphite by mechanical cleavage [10], chemical exfoliation [11], thermal decomposition [12], and electrochemical exfoliation [13, 14]. Among these, electrochemical exfoliation, which is performed without the use of toxic, corrosive oxidizing/reducing agents, is a simple, rapid, inexpensive, and green method to produce graphene flakes [14, 15].

Electrochemical exfoliation strategies depend on the intercalation of ions/molecules between graphene layers because of the applied electrical current in an electrolytic cell [16]. The experimental setup for two-electrode systems commonly contain a graphite electrode (graphite rods, graphite foil, highly orientated pyrolytic graphite, graphite powders, or graphite flakes) as working electrode, a counter electrode, a power supply and an electrolyte system [16, 17]. When a positive or negative current is applied, oppositely charged ions intercalate with graphite electrode, which prompt expansion of graphite [18]. For this, two electrolyte systems have been adopted: ionic liquids and aqueous acids [19]. Depending on the electrolyte systems, the nature of

*As published in Carbon 2018, 138, 108–117.
*Patent application filed on 31-Oct-2018 (no: P180075US02)

produced graphene flakes varies. With ionic liquids, high structural quality of few layers to several layers of graphene flakes can be obtained. Although some ionic liquids are environmentally friendly, after intercalation with graphene during to exfoliation process, it disrupts the electronic properties of graphene [18]. Also, the low yield of graphene with a small lateral size (<5 μm), and high cost limit its application [20]. When using aqueous acids such as H_2SO_4 and H_3PO_4, graphene yield is higher with better structural quality and larger lateral size; however, the presence of oxygen functional groups destroys their electrical conductivity. A green approach was reported using 1M H_3PO_4 as an electrolyte solution and used pencil cores as both anode and cathode to produce graphene oxide flakes [21]. However, during exfoliation H_3PO_4 causes inevitable oxidation of graphene which results in high structural defects on the surface. Another environmentally friendly approach of Rao et al. using sodium hydroxide/hydrogen peroxide/water ($NaOH/H_2O_2/H_2O$) system results in 3-6 layers of graphene nanosheets [22]. Therefore, it is desirable to identify a proper electrolyte system that can exfoliate graphite into graphene sheet with few defects, large lateral size, high electrical conductivity, and high yield.

Graphene has been integrated into free-standing and flexible three-dimensional (3D) structures such as graphene paper [23, 24], foam [25, 26], and film [27, 28] via various methods: vacuum filtration [29], lyophilization [30], mechanical compression of graphene hydrogels [31] or aerogels [32] and simply drying on flexible substrates [33]. Free-standing and thin graphene paper (GrP) holds great promise for energy-storage devices, biosensors, actuators, shape memory devices and practical oil-absorption applications due to superior mechanical strength, and electrical conductivity [34-38]. Although self-assembly of reduced graphene oxide and its derivatives, chemically exfoliated from graphite, seem an effective strategy to prepare GrP, the method leads to serious defects and residual oxygen-containing groups on graphene sheets after the reduction of

graphene oxide [39]. The reduction method helps to restore the electrical properties, degrades graphene structure and mechanical properties, and causes GrP to be brittle and fragile [40]. Therefore, an alternative way to synthesize graphene is needed to prepare GrP with desirable characteristics.

Herein, we report a novel approach to fabricate free-standing, flexible, and highly conductive GrP and demonstrate its use in supercapacitor and as an absorbent of oil and organic solvents. A novel fabrication process for GrP is illustrated as shown **Figure 2.1**. In brief, GrP is made by synthesizing partially oxidized graphene (po-Gr) via electrochemical exfoliation of graphite using phosphate-buffered saline (PBS) to maintain constant pH and subsequently vacuum filtering and air drying. The thickness of GrP is controlled by adjusting the volume and/or concentration of po-Gr suspension used for filtration. The prepared GrP can be cut into any desired shape as if it were a regular paper.

2.2 Experimental section

2.2.1 Preparation of exfoliated graphite (EG)

As illustrated in **Figure 2.1**, po-Gr dispersion was obtained via electrochemical exfoliation. Graphite sheets were used both as anode and cathode electrodes with 0.1 M phosphate-buffered saline (PBS) solution (pH 7.0) as supporting electrolyte at room temperature. By applying 10.0 V DC (Tektronix PS280) across the graphite electrodes for 30 min, partially oxidized graphene (po-Gr) flakes were collected and washed with deionized (DI) water several times using vacuum filtration through mixed cellulose filter paper (pore size=0.2 μm). The resulting product was

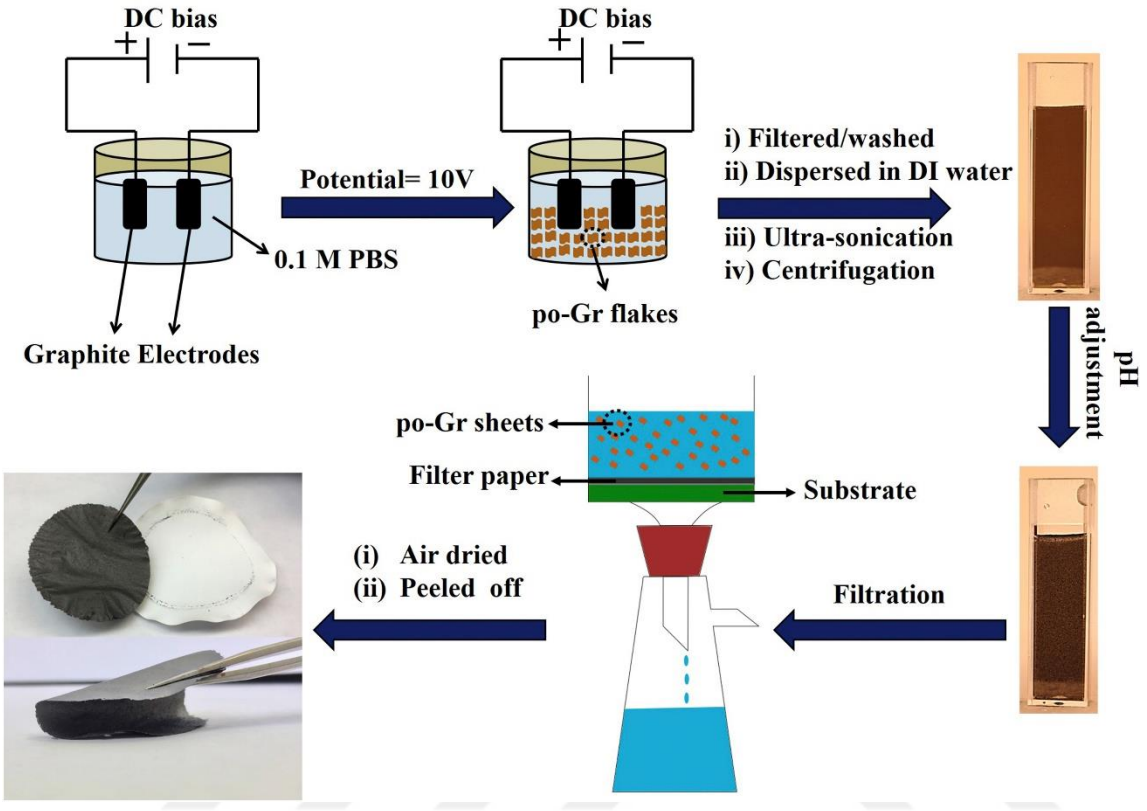

Figure 2.1 Steps in the preparation of flexible, free-standing GrP starting from graphite sheets.

dispersed in DI water by sonicating for 60 min to obtain po-Gr dispersion. The dispersion was then centrifuged at 3000 rpm for 30 min, supernatant was collected, and the concentration was adjusted to 1 mg mL^{-1}.

2.2.2 Preparation of GrP

3 mL of po-Gr (1 mg mL^{-1}) dispersion was diluted with 50 mL DI water and pH was adjusted to 3.5 using 1 M of H_2SO_4. The final solution was filtered through mixed cellulose filter paper (pore size=0.2 µm). After drying at room temperature for 6 h, the GrP was easily peeled off from filter paper.

2.2.3 Electrochemical measurements of GrP

An electrochemical workstation (660D, CH Instruments) was used for electrochemical measurements. Three-electrode system was employed to investigate the supercapacitance performance of the as-prepared electrode with Pt wire and Ag/AgCl (1 M KCl) as counter and reference electrodes, respectively. Cyclic voltammetry (CV) and galvanostatic charge/discharge (GCD) measurements were done in 1 M H_2SO_4 as electrolyte. The GrP was attached to a poly(ethylene terephthalate) (PET) substrate as a support using two-sided carbon tape with an alligator clip onto a copper foil to ensure good electrical contact as shown in **Figure A 2.1**. Electrochemical impedance spectroscopy (EIS) was performed in 0.1 M KCl containing 5 mM $[Fe(CN)_6]^{3-/4-}$ vs. Ag/AgCl over a frequency range of 0.1 Hz to 100 kHz at 0.318 V at room temperature. The first cycle of the CV measurements was always discarded.

2.2.4 Oil and organic solvents absorption experiments

The absorption capacity of GrP was studied by weighing the samples before (W_i) and after (W_t) soaking them in different oils (mineral and pump oil) or organic solvents (octane, toluene, benzene, acetonitrile, methanol and cyclohexane) as percent weight gain (Q) per the following equation:

$$Q = \frac{W_t - W_i}{W_i} \times 100 \quad (1)$$

The ability to reuse the GrP for oil absorption was studied using motor oil after removing the absorbed oil by burning the GrP in an open flame for at least 25 s and washing with acetone followed by drying at 60 °C for 5 min.

2.2.5 Material characterizations

Fourier transform infrared (FT-IR) (Spectrum 100, Perkin Elmer), Raman (LabRAM Aramis Horiba Jobin Yvon Confocal Raman Microscope) (wavelength: 532 nm), and X-ray photoelectron

(XPS) (Thermo Scientific K-Alpha) spectroscopies were used to characterize chemical composition of GrP. Thermal properties were measured with differential scanning calorimetry (DSC, TA Instruments Q20), with a heating and cooling cycle in the temperature range of 25 and 400 °C, and thermogravimetric analysis (TGA, TA Instruments Q50). The surface morphology of the samples was investigated using a field emission scanning electron microscope (FE-SEM) (LEO1530, Gemini FE-SEM, Carl Zeiss) set at 3 kV and 3 mm working distance and transmission electron microscope (TEM, Tecnai T-12). The tensile properties were measured with thin strips of GrP (0.09 mm thick, 3.18 mm wide and 9.53 mm long) in a universal testing machine (Instron 5967, 50-N load cell) at a crosshead speed of 0.5 mm min^{-1}. Sheet resistance (R_s) was measured using a four-point probe (Cascade Microtech, Inc) which uses the following equation:

$$R_s = cf * \frac{V}{I} \quad (2)$$

Where, *cf* is the correction factor, ($\frac{\pi}{\ln(2)} = 4.532$), *I* is the applied voltage, and *V* is the potential between inner contacts.

2.3 Results and discussion

2.3.1 Gr-P formation and characterization

The po-Gr sheets that get assembled on the surface of mixed cellulose filter paper is shown in **Figure 2.2a**, which is subsequently dried at room temperature for 4 h (**Figure 2.2b**) and peeled-off as free-standing GrP (**Figure 2.2c**). The fabricated GrP is mechanically stable and flexible and can be cut into any desired shape and bent into acute angles (**Figure 2.2d, e, f**). By adjusting the volume and/or concentration of po-Gr suspension, the thickness of GrP can be controlled. To demonstrate the controllable thickness, we prepared GrP with four different concentrations and

volumes. When using 1.25 mg of po-Gr suspension in 50 mL of DI water, 5-µm thick GrP was obtained (**Figure A 2.2a)**. When the concentration was doubled (2.5 mg in 50 mL DI water), GrP thickness also doubled (10 µm) (**Figure A 2.2b**) and when the volume was doubled (2.5 mg in 100 mL) we still obtained 10-µm thick GrP (**Figure A 2.2c**). Compared to other methods of fabricating paper-like graphene sheets, such as self-assembly of chemically modified graphene, our method is simple and of low-cost, which makes it suitable for widespread use. Since we do not use any binders, toxic and corrosive agents, or high temperature. This method is also environmentally friendly.

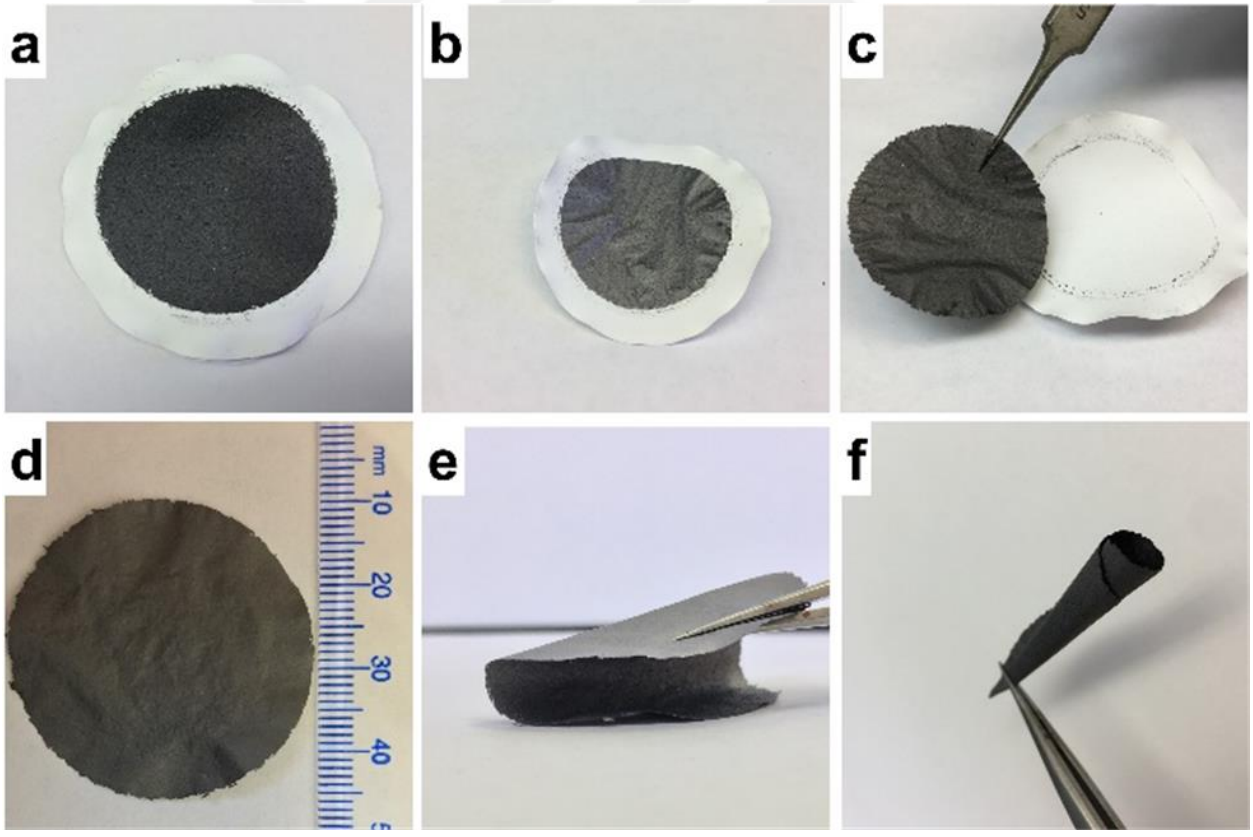

Figure 2.2 Digital images of GrP with filter paper (a) before and (b) after drying and (c) after peeling off. (d,e,f) demonstrate the flexibility of GrP.

The electrochemical exfoliation of graphite was confirmed by TEM, which shows mostly transparent monolayers of exfoliated graphene sheets (1-3 layers) (**Figure 2.3a**). When pH of the po-Gr solution was adjusted to 3.5, the po-Gr sheets aggregated because at a lower pH, the carboxyl groups on po-Gr sheets are protonated and become less hydrophilic [41]. As shown **Figure 2.3b**, these aggregates form a multilayered graphene stack. During vacuum filtration, a well-ordered layered structure was formed due to partial overlapping or coalescence of exfoliated graphene sheets, which are closely interconnected by physical crosslinking sites in the framework of the GrP because of the π-π interactions, van der Waals attraction between graphene sheets and hydrogen bonds due to oxygen containing groups on graphene sheets [42, 43]. Thus, this architecture results in compact, free-standing, and flexible GrP.

SEM micrographs of GrP reveal typical wrinkled and curved features of graphene (**Figure 2.3c**). The cross-sectional view of a torn GrP shows a ~12-µm thick uniform and well-stacked 2D layered hierarchy (**Figure 2.3d, e**). This feature is particularly beneficial for electrode materials due to the highly accessible surface area for ion and electron diffusion, which lowers charge transfer resistance and increases capacitance of the electrode [44]. The surface morphology was further studied after heat-treating the GrP at 400 °C for 3 h, which shows, besides the wrinkled and curved features, the presence of sharp edges (**Figure 2.3f**) attributed to the elimination of entrapped water.

In the DSC scan two irreversible peaks are observed during the heating cycle (**Figure 2.4a**). The first endothermic peak, between 78 °C and 133 °C, is ascribed to vaporization of residual water between the graphene sheets and the second exothermic peak at 165 °C is attributed to defunctionalization of graphene sheets [45]. These endothermic and exothermic peaks were not

observed in the subsequent cooling cycles. The TGA and derivative weight loss data (**Figure A 2.3**) agrees well with the DSC data, indicating that GrP is thermally stable.

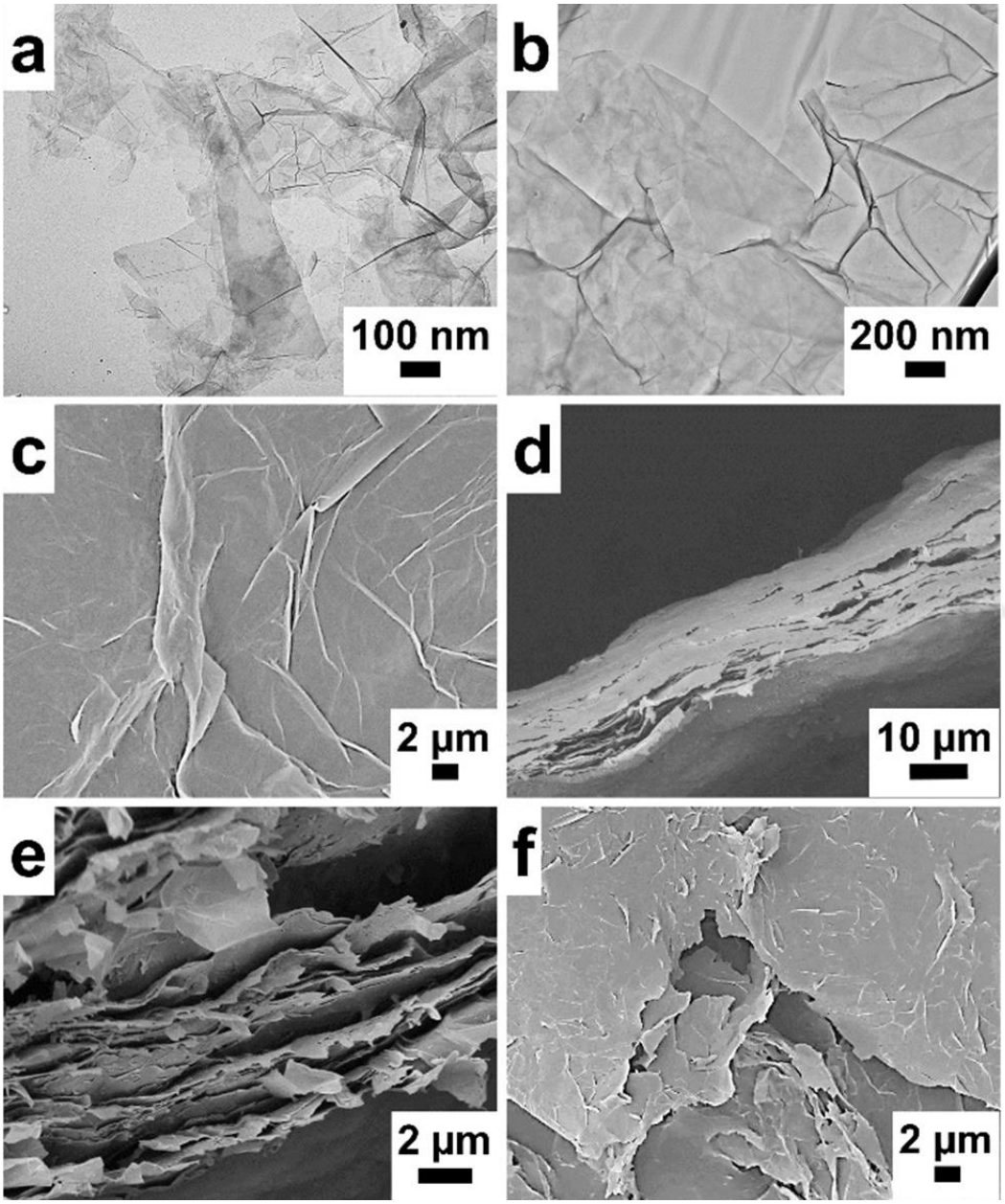

Figure 2.3 TEM images of (a) po-Gr sheets and (b) GrP and SEM images of GrP (c) at room temperature, cross sectional view of GrP at low (d) and high (e) magnifications and (f) heat-treated (at 400 °C for 3 h) GrP.

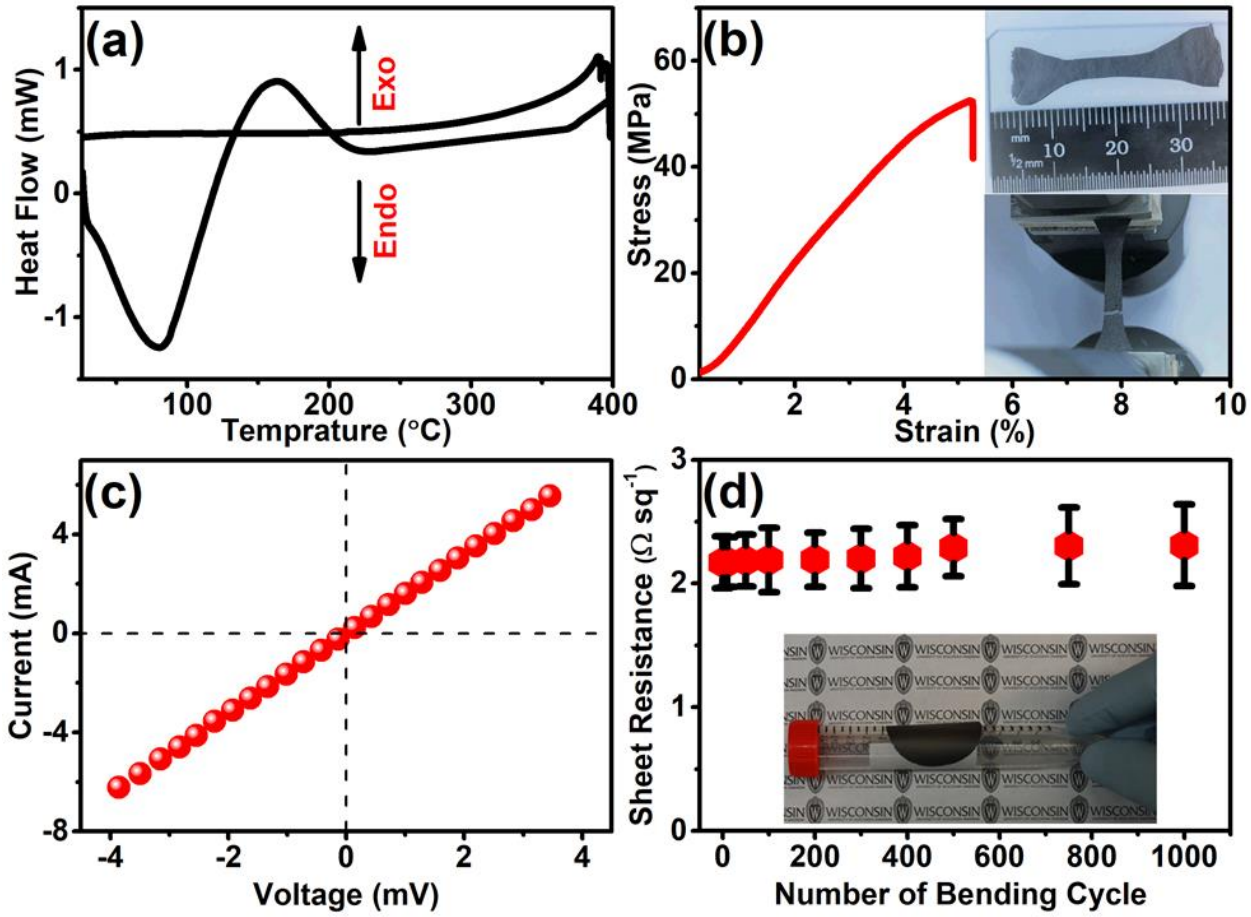

Figure 2.4 (a) DSC curves of as-prepared GrP, (b) Tensile stress-strain curve with 0.09-mm thick GrP sample, insets: specimen before (top) and after (bottom) the test (c) Current–voltage response, (d) Sheet resistance as a function of number of bending cycles (inset: photograph of GrP during a bending test).

A typical tensile stress-strain curve for GrP is shown in **Figure 2.4b**, with insets showing the test strip before and after fracture. The average tensile strength and elongation of 90-µm thick GrP sample were 52.3±2.3 MPa and 5.1±0.4%, respectively. These values suggest strong interlayer binding of individual graphene sheets due to presence of oxygen containing groups which can help in the formation of hydrogen bonds. Also, comparing the previously reported mechanical

properties (**Figure A 2.1**) our GrP is both strong and pliable and hence can be an ideal candidate for energy-related devices, which require mechanically strong and flexible materials [46-50].

The linear current-voltage (I-V) curves of GrP, obtained with a four-point probe (Cascade Microtech, Inc), indicate an Ohmic behavior, typical of conductors (**Figure 2.4c**). The sheet resistance and electrical conductivity were calculated as 2.2 Ω sq^{-1} and $3.85x10^5$ S m^{-1}, respectively which bode well for energy applications [42]. The sheet resistance remained nearly unchanged, changing by only 4%, even after 1,000 consecutive bending cycles (bending radius= 10 mm) at room temperature (**Figure 2.4d**), indicating good mechanical durability and flexibility, which is likely due to the intrinsic nature of well-stacked layers of graphene sheets.

Figure 2.5a shows FT-IR spectrum for GrP and pristine graphite sheets. While there was no significant peak in the spectrum for graphite sheets, the GrP spectrum shows peaks at ~3430 (OH stretch), 2326 (CO_2 stretch), 1725 (C=O stretch), and 1642 cm^{-1} (C=C stretch) [14]. The Raman spectra of GrP, po-Gr, and pristine graphite sheet are shown in **Figure 2.5b**. The spectrum for graphite sheet shows a very small D band at 1361 cm^{-1} corresponding to the edge-induced disorder related to the presence of sp^3 defects, a large G band around 1594 cm^{-1} due to n-plane vibration of sp^2 hybridized carbon atoms and 2D band around 2729 cm^{-1}, which is associated with two phonon lattice vibrations [13]. The spectrum for po-Gr shows a large D band at 1343 cm^{-1}, G band at 1587 cm^{-1} and a 2D band at 2687 cm^{-1}, which provide clear evidence for the presence of localized sp^3 defects in the sp^2 hybridized carbon atoms upon exfoliation and subsequent dispersion in H_2O. After pH adjustment of po-Gr dispersion and filtration, D and G bands downshifted 1340 and 1575 cm^{-1}, respectively, and 2D band upshifted to 2703 cm^{-1}.

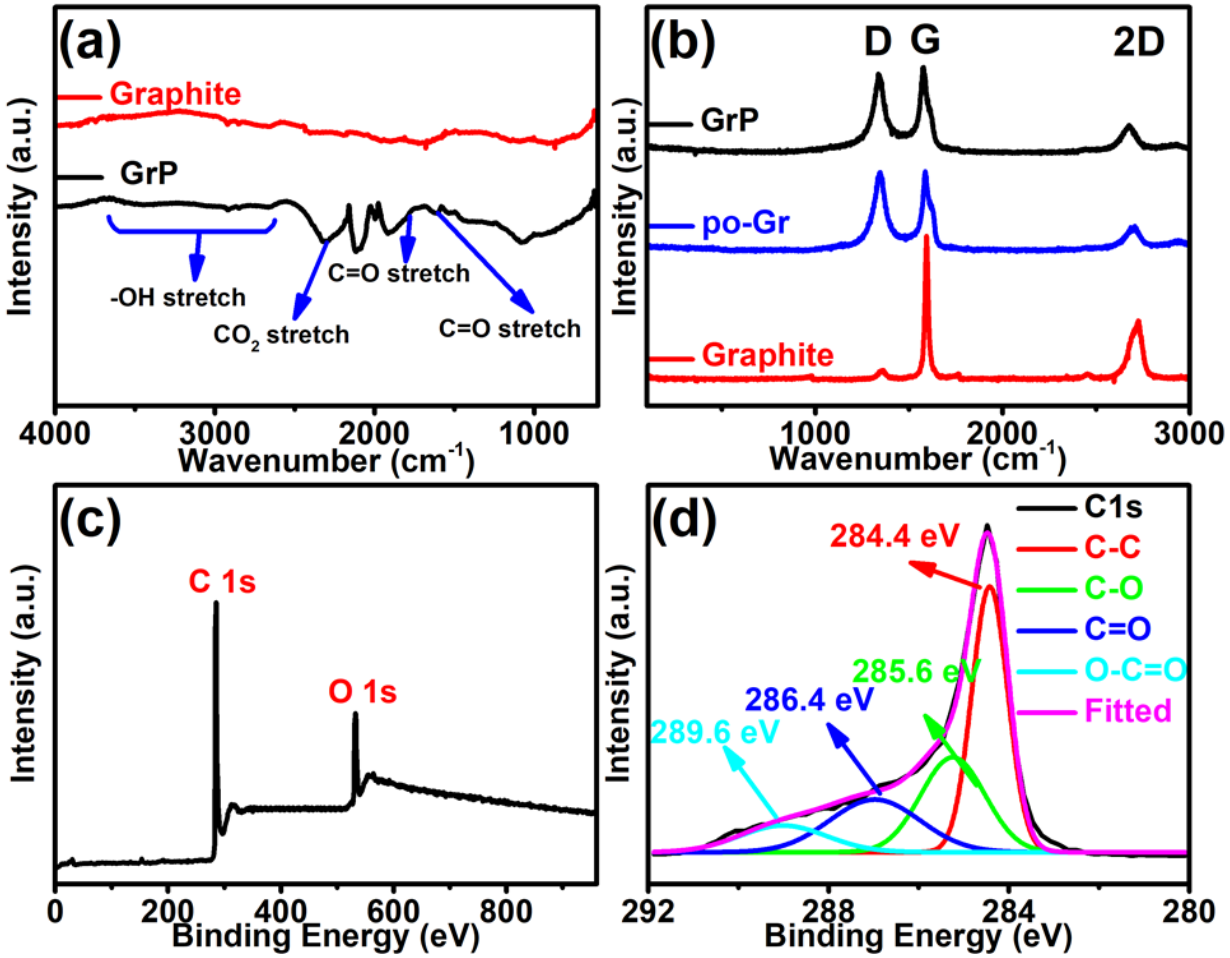

Figure 2.5 (a) FT-IR spectra of GrP and pristine graphite (b) Raman spectra of GrP, po-Gr and pristine graphite (c) wide XPS spectrum of GrP and (d) survey spectrum and high-resolution spectra for C1s.

The wide XPS spectrum of GrP (**Figure 2.5c**) shows sharp peaks at 286 and 530 eV corresponding to carbon (C1s) and oxygen (O1s), respectively. **Figure 2.5d** exhibits the C1s spectrum, which shows peaks of 284.4, 285.6, 286.4 and 289.6 eV, corresponding to C–C, C–O, C=O and O–C=O bonds, respectively. The peak at 285.6 eV is attributed to sp^3 carbon, indicating the amount of oxidized carbon species is weak. The C/O ratio is about 8.68, confirming good quality of the graphene sheets [51]. These results also indicate the use of PBS as electrolyte during to exfoliation process enhances the chemical and structural quality of individual graphene layers.

2.3.2 Electrochemical performance of GrP as a supercapacitor electrode

The CV measurements were performed in different potential windows with a fixed lower potential value (0 V) to upper potential values up to 1.8 V at 100 mV s^{-1} to test the stability and performance of the GrP at different operating potentials (**Figure 2.6a**). Usually, the larger the potential window, the higher the power density. As expected, the potential window of the GrP is extendable as large as 1.4 V without any observable oxygen evolution peak or obvious polarization. The GCD curves at different potential windows from 0.8 to 1.4 at 1 A g^{-1} are highly symmetrical up to 1.2 V (**Figure 2.6b**), which indicates high electrochemical reversibility. The CV curves of the GrP at various scan rates from 1 to 100 mV s^{-1} in the 0 – 1.0 V potential window were rectangle-like, which indicates good capacitive behavior (**Figure 2.6c**). The specific capacitance (C_p, F g^{-1}) of the GrP was calculated from CV curves as 195.8 F g^{-1} using the following equation (3):

$$C_P = \frac{\int_{V_a}^{V_c} I(V)\,dV}{mv\,(V_a - V_c)} \qquad (3)$$

where, m is the mass of active materials on the electrodes (g), V is the scan rate of CV curves (V s^{-1}) and (V_a -V_c) is the potential window (V).

The GCD curves were also obtained in the potential range of 0 – 1.0 V at different current densities. The equilateral triangle-shaped charge/discharge curves indicate high reversibility with a rapid I–V response with no IR drop (**Figure 2.6d**). The electrochemical stability of GrP was also investigated with GCD test at a current density of 4 A g^{-1}. As shown in **Figure 2.6e,** GrP retained

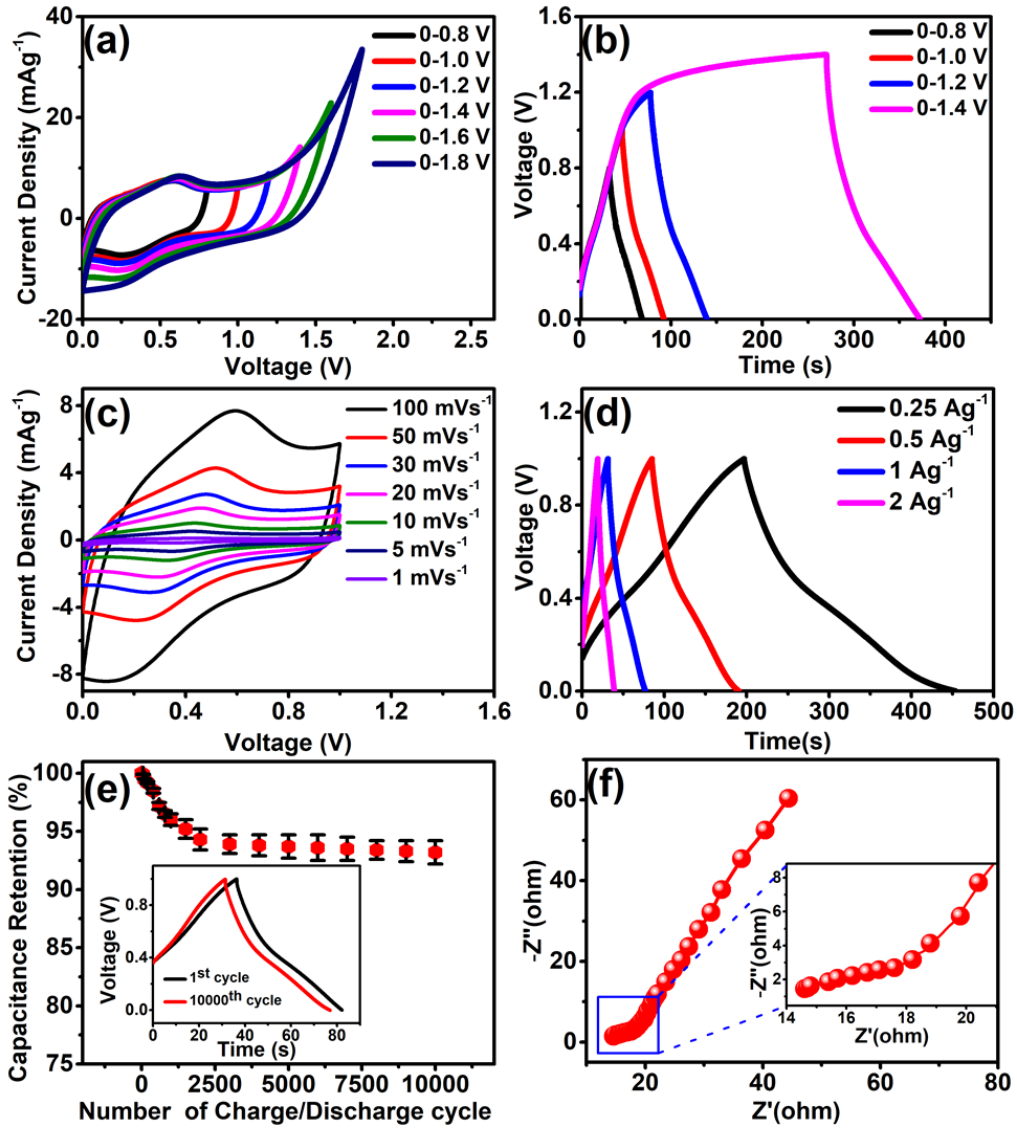

Figure 2.6 (a) CV of GrP at different potential windows in 1 M H_2SO_4 (b) GCD curves of GrP at a constant current density of 1 A g^{-1} in 1 M H_2SO_4 with different potential windows (c) CV of GrP at different scan rates in 1 M H_2SO_4 at 1, 5, 10, 20, 30, 50 and 100 mV s^{-1} (d) GCD curves of GrP at different current densities (e) Cycle life of GrP at a constant current density of 1 A g^{-1} (inset is the corresponding charge/discharge curve) (f) Nyquist plots of GrP in 0.1 M KCl solution containing 5 mM $[Fe(CN)_6]^{3-/4-}$ with frequency range from 0.1 Hz to 100 kHz (inset: details at high frequency).

93.2 % of its capacitance after 10,000 consecutive cycles; and most of the loss occurring in the first 3,000 cycles, which could be attributed to the removal of oxygenated groups on the GrP surface that induce Faradaic redox reactions and electrode/electrolyte interface wetting.[52]

The electrochemical properties of GrP were further studied with EIS. The Nyquist plots of GrP obtained with EIS exhibit a semicircle-like shape in the high frequency region and a straight line in the low frequency region (**Figure 2.6f**). The diameter of the semicircular arc corresponds to charge transfer resistance (R_{ct}), which is about 4.1 **Ω**. The X-intercept in the high frequency region corresponds to a low equivalent series resistance (R_s= ~14.5 **Ω**), and the spike in the low frequency region implies ideal electrochemical stability and more capacitance behavior. When compared to the electrochemical properties of previously reported 3D graphene materials, our GrP has substantially higher C_p and lower sheet resistance (**Table 2.1**) [29, 30, 46, 47, 49, 53-58].

2.3.3 Oil absorption performance of GrP

The absorption results reveal that the GrP is capable of soaking various organic liquids and oils up to 28 times its weight (**Figure 2.7a**). Compared to graphite, the GrP is about 15 times better (**Figure 2.7b**), and several times higher than many previously reported absorbents such as flexible macroporous polypropylene sponges [59], commercially available PP fabric [60], nanowire membranes [61] and polydimethylsiloxane (PDMS) sponge [62]. The superior oil and organic solvent absorption capability of GrP is attributed to its porous, and layered microstructure, low density, excellent mechanical property, and hydrophobicity. As shown in **Figure 2.7c**, GrP maintained its original paper-like morphology and high absorption capacity, changing by only 2%, after 10 consecutive motor oil absorption/desorption cycles, which indicates its superior stability and reusability. It is worth noting that many other 3D graphene platforms easily disintegrate during

Table 2.1 Properties of synthesized GrP with those of previously reported graphene materials

Graphene Materials[a)]	**Synthesis Method**	**Sheet Resistance (Ω sq^{-1})**	**Thickness (μm)**	**Specific capacitance (F g^{-1})**	**Ref.**
Graphene paper	Filtration/ vacuum drying	N/A [c)]	102	147	[46]
Graphene paper	Filtration/drying	N/A	N/A	120	[47]
rGO foam	Filtration/drying	>100	N/A	110	[49]
rGO	Filtration/drying	21-23	1.4	N/A	[29]
Graphene paper	Mechanical pressing of the GO[b)] aerogel	N/A	10	111	[30]
rGO film	Brush-coating/annealing	225	N/A	81.7	[53]
rGO powder	Chemical graphitization	19.6	6.5	N/A	[54]
rGO film	Gas-phase reduction of GO	8.5	6.5	N/A	[55]
Functionalized graphite	Solution casting	60	N/A	N/A	[56]
rGO film	Oven drying	15	30	180	[57]
rGO paper	Filtration/ thermal reduction	10-16	5	N/A	[58]
GrP	Electrochemical exfoliation/vacuum filtration	2.2	12	195.8	This work

[a)] rGO: reduced graphene oxide; [b)] GO: graphene oxide; [c)] N/A: not applicable

recycling [63]. Furthermore, the sheet resistance of the GrP remained nearly unchanged during the test (**Figure A 2.4**), indicating virtually unaltered mechanical, chemical, and electrical properties through repeated uses.

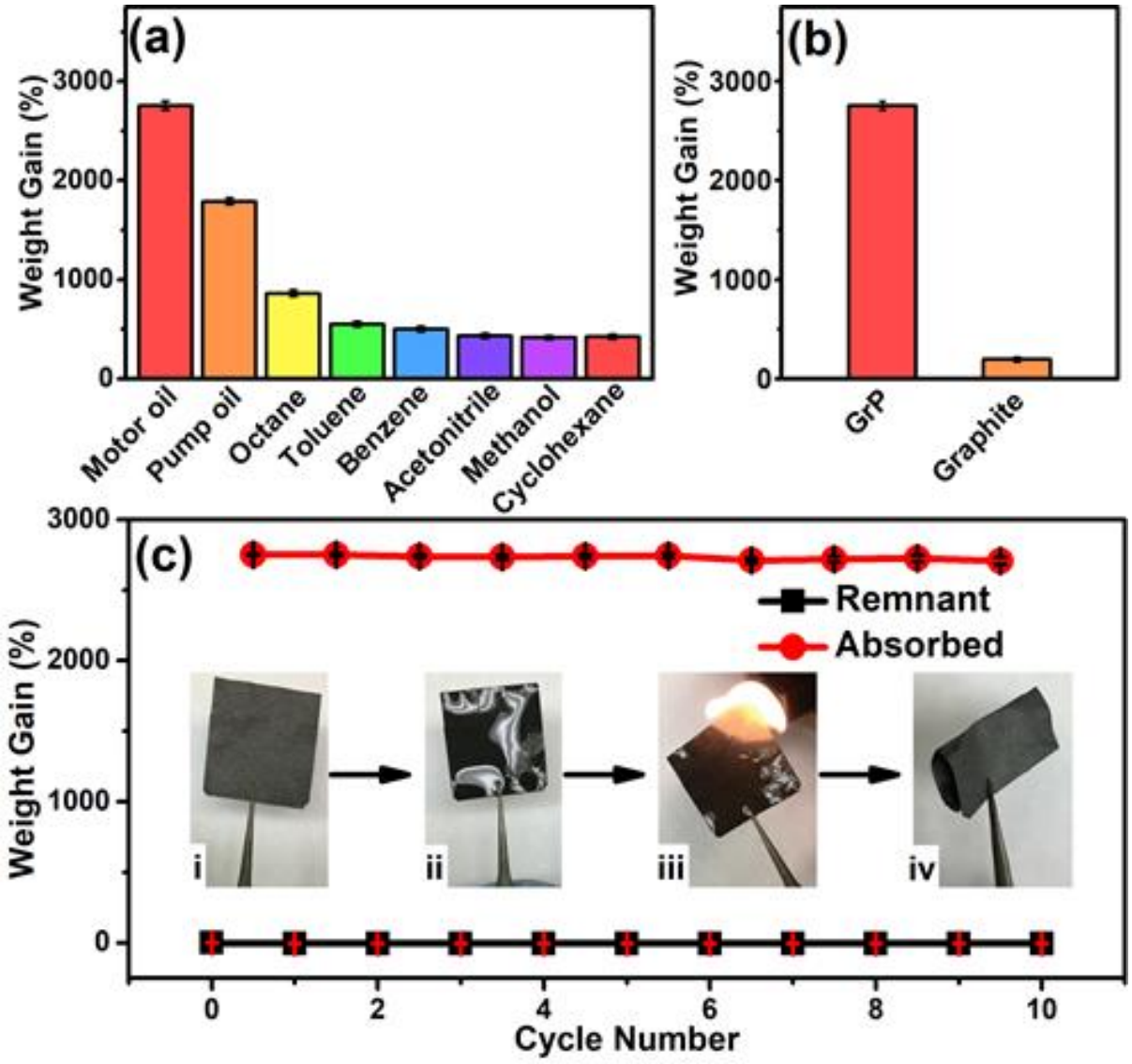

Figure 2.7 (a) Absorption capacity of GrP for various oils and organic solvents as percent weight gain (b) absorption capacity of GrP and graphite sheets for motor oil (c) absorption reusability of the GrP for motor oil. Insets are GrP (i) before and (ii) after oil absorption, (iii) oil removal step and (vi) after the removal of oil.

2.4 Conclusions

We described a simple, inexpensive and green method to fabricate free-standing, flexible, and highly conductive GrP. It is electrically very stable and with an ultralow sheet resistance (for 12-μm thick sample) of 2.2 Ω sq^{-1} even after 1,000 consecutive bending cycles (at 10 mm bending radius) and high electrical conductivity of $3.85x10^5$ S m^{-1}. The GrP exhibited an excellent capacitive performance with high specific capacitance of 195.8 F g^{-1} at 1 mV s^{-1} in 0.1 M H_2SO_4 electrolyte and outstanding stability with 93.2 % capacitance retention after 10,000 consecutive cycles. The tensile strength and peak elongation of the fabricated GrP were 52.3 ±2.3 MPa and 5.1 ±0.4%, respectively. The GrP is also an excellent oil or organic solvent absorbent with superior reusability.

2.5 Appendix: Chapter II

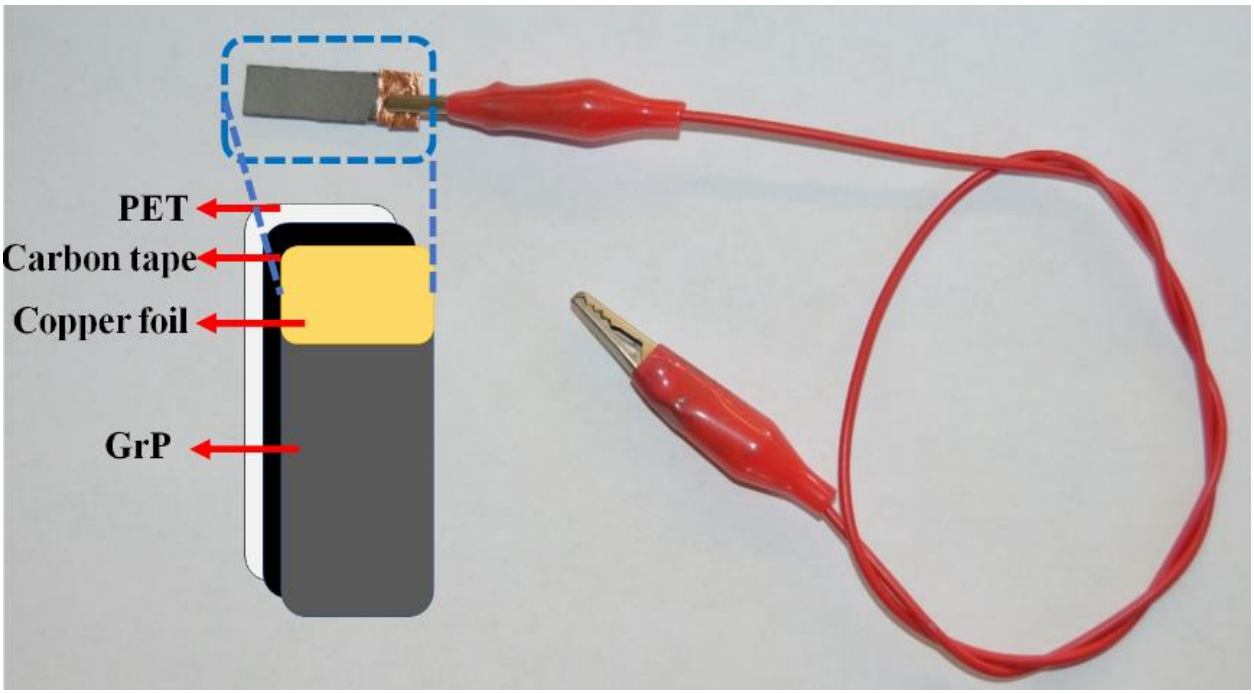

Figure A 2.1 Demonstration of GrP electrode for electrochemical measurement.

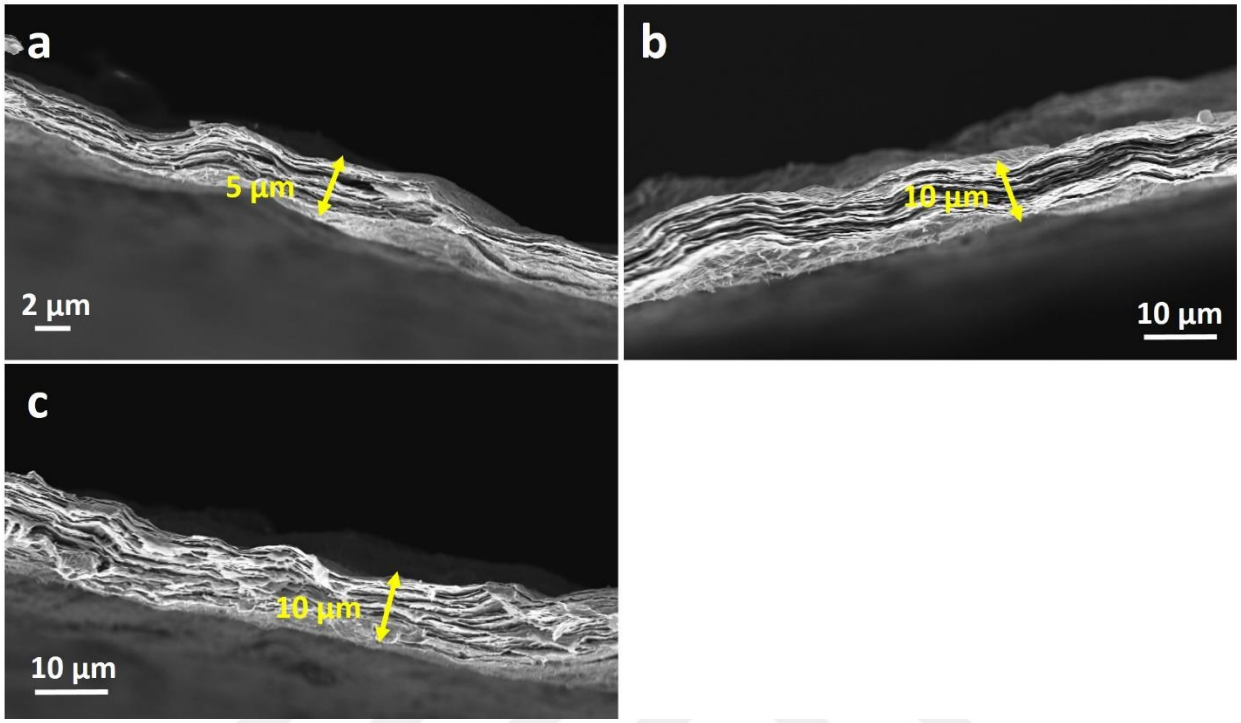

Figure A 2.2 SEM images of cross-sectional view of GrP with different concentration and volume (a) 1.25 mg of po-Gr in 50 mL DI water, (b) 2.5 mg of po-Gr in 50 mL DI water and (c) 2.5 mg of po-Gr in 100 mL DI water.

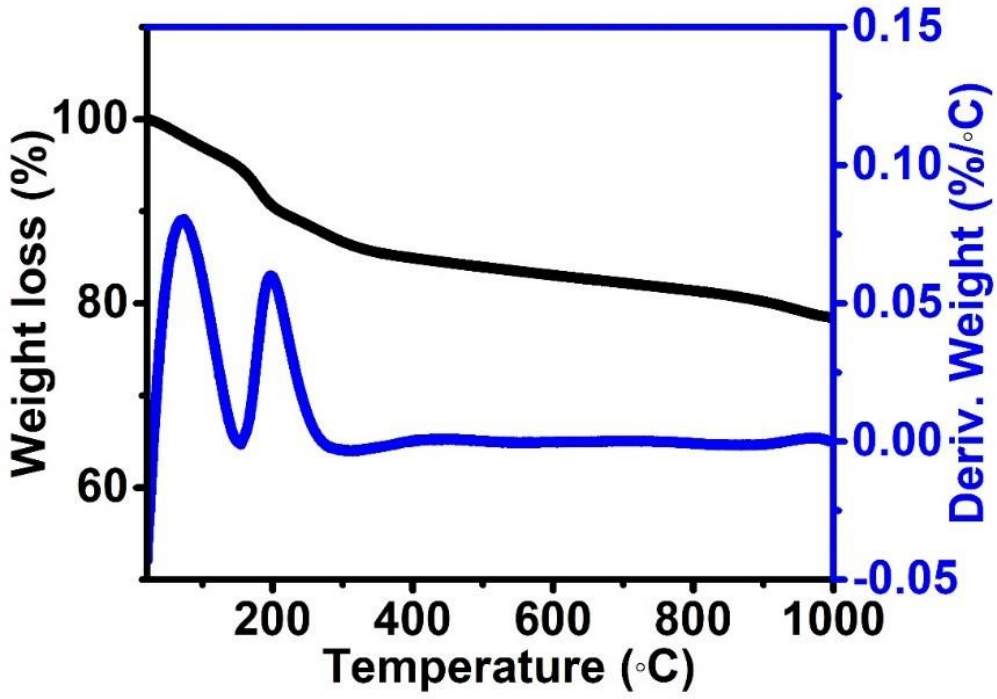

Figure A 2.3 Thermogravimetric and derivative weight loss curves of as-prepared GrP.

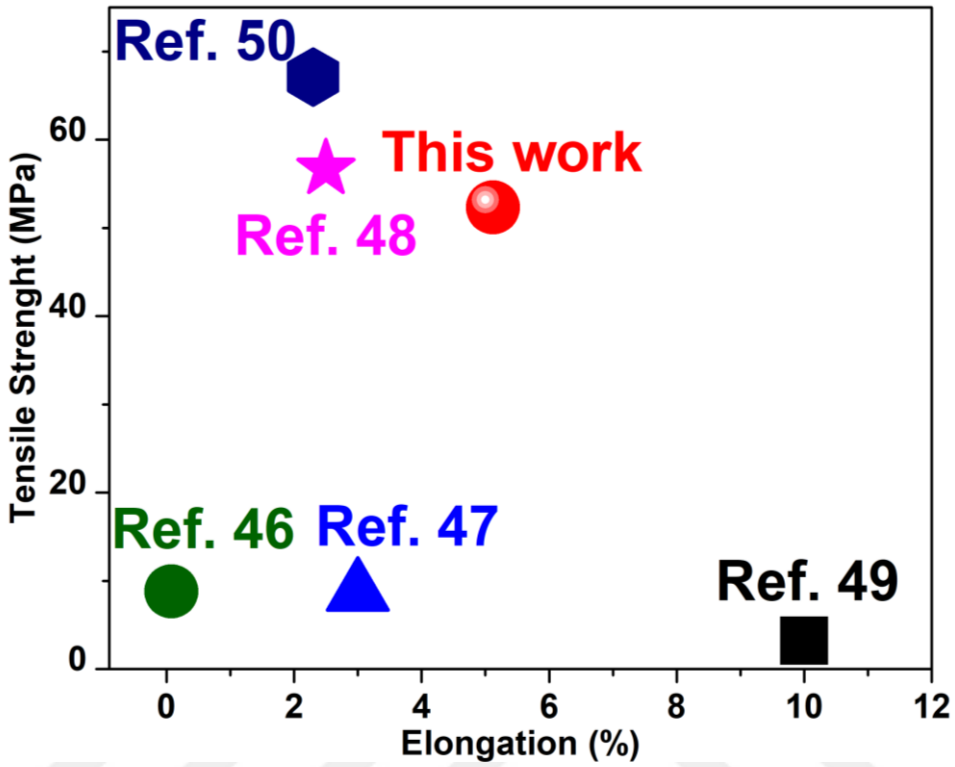

Figure A 2.2 Mechanical properties of reported 3D graphene-based material.

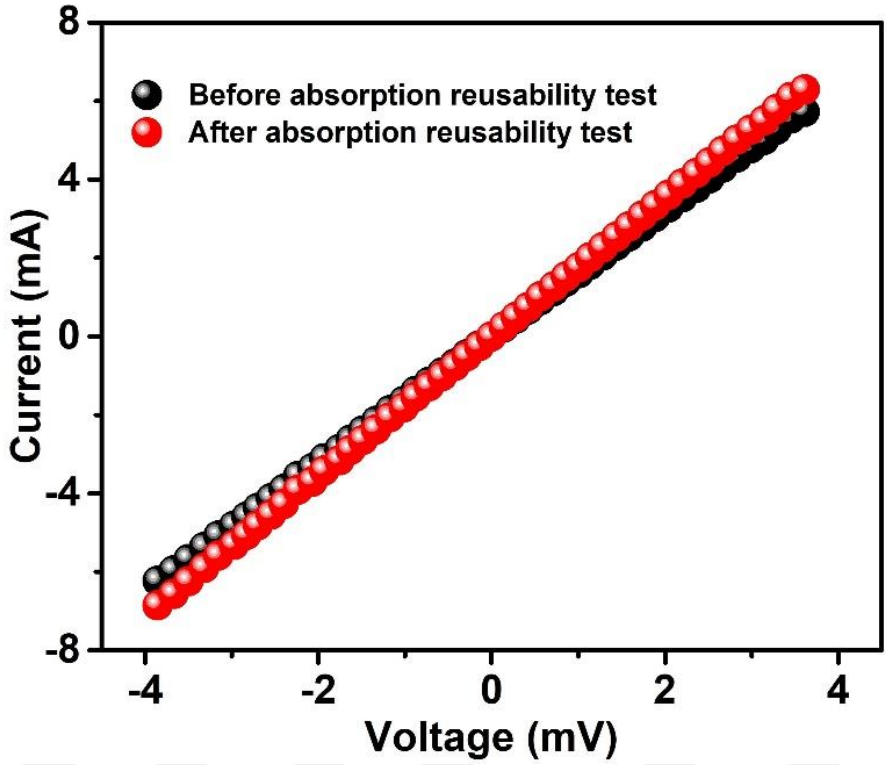

Figure A 2.4 Current–voltage response before and after the absorption reusability test.

2.6 References

[1] N.A. Kumar, M.A. Dar, R. Gul, J.B. Baek, Graphene and molybdenum disulfide hybrids: synthesis and applications, Mater Today 18(5) (2015) 286-298.
[2] M. Wang, X.D. Duan, Y.X. Xu, X.F. Duan, Functional Three-Dimensional Graphene/Polymer Composites, Acs Nano 10(8) (2016) 7231-7247.
[3] A.C.H. Tsang, H.Y.H. Kwok, D.Y.C. Leung, The use of graphene based materials for fuel cell, photovoltaics, and supercapacitor electrode materials, Solid State Sci 67 (2017) A1-A14.
[4] Y. Zhu, S. Murali, W. Cai, X. Li, J.W. Suk, J.R. Potts, R.S. Ruoff, Graphene and graphene oxide: synthesis, properties, and applications, Advanced materials 22(35) (2010) 3906-24.
[5] Q.W. Ke, J., Graphene-based materials for supercapacitor electrodes, Journal of Materiomics 2(1) (2016) 37–54.
[6] F. Bonaccorso, A. Lombardo, T. Hasan, Z.P. Sun, L. Colombo, A.C. Ferrari, Production and processing of graphene and 2d crystals, Mater Today 15(12) (2012) 564-589.
[7] B. Vedhanarayanan, B. Babu, M.M. Shaijumon, A. Ajayaghosh, Exfoliation of Reduced Graphene Oxide with Self-Assembled pi-Gelators for Improved Electrochemical Performance, ACS Appl Mater Interfaces 9(23) (2017) 19417-19426.
[8] N.O. Weiss, H. Zhou, L. Liao, Y. Liu, S. Jiang, Y. Huang, X. Duan, Graphene: an emerging electronic material, Advanced materials 24(43) (2012) 5782-825.
[9] L.M. Xu, G.Y. Xiao, C.B. Chen, R. Li, Y.Y. Mai, G.M. Sun, D.Y. Yan, Superhydrophobic and superoleophilic graphene aerogel prepared by facile chemical reduction, J Mater Chem A 3(14) (2015) 7498-7504.
[10] B. Jayasena, S. Subbiah, A novel mechanical cleavage method for synthesizing few-layer graphenes, Nanoscale Res Lett 6 (2011).
[11] L. Zhang, X. Li, Y. Huang, Y.F. Ma, X.J. Wan, Y.S. Chen, Controlled synthesis of few-layered graphene sheets on a large scale using chemical exfoliation, Carbon 48(8) (2010) 2367-2371.
[12] Z.L. Wang, D. Xu, Y. Huang, Z. Wu, L.M. Wang, X.B. Zhang, Facile, mild and fast thermal-decomposition reduction of graphene oxide in air and its application in high-performance lithium batteries, Chem Commun 48(7) (2012) 976-978.
[13] N.G. Yasri, A.K. Sundramoorthy, S. Gunasekaran, Azo dye functionalized graphene nanoplatelets for selective detection of bisphenol A and hydrogen peroxide, Rsc Advances 5(106) (2015) 87295-87305.
[14] O. Sadak, A.K. Sundramoorthy, S. Gunasekaran, Highly selective colorimetric and electrochemical sensing of iron (III) using Nile red functionalized graphene film, Biosensors & bioelectronics 89(Pt 1) (2017) 430-436.
[15] M. Mao, M.M. Wang, J.Y. Hu, G. Lei, S.Z. Chen, H.T. Liu, Simultaneous electrochemical synthesis of few-layer graphene flakes on both electrodes in protic ionic liquids, Chem Commun 49(46) (2013) 5301-5303.
[16] S. Yang, M.R. Lohe, K. Mullen, X.L. Feng, New-Generation Graphene from Electrochemical Approaches: Production and Applications, Advanced materials 28(29) (2016) 6213-6221.
[17] K. Parvez, Z.S. Wu, R.J. Li, X.J. Liu, R. Graf, X.L. Feng, K. Mullen, Exfoliation of Graphite into Graphene in Aqueous Solutions of Inorganic Salts, Journal of the American Chemical Society 136(16) (2014) 6083-6091.
[18] J.M. Munuera, J.I. Paredes, M. Enterria, A. Pagan, S. Villar-Rodil, M.F.R. Pereira, J.I. Martins, J.L. Figueiredo, J.L. Cenis, A. Martinez-Alonso, J.M.D. Tascon, Electrochemical Exfoliation of Graphite in Aqueous Sodium Halide Electrolytes toward Low Oxygen Content Graphene for Energy and Environmental Applications, Acs Appl Mater Inter 9(28) (2017) 24085-24099.

[19] C.T.J. Low, F.C. Walsh, M.H. Chakrabarti, M.A. Hashim, M.A. Hussain, Electrochemical approaches to the production of graphene flakes and their potential applications, Carbon 54 (2013) 1-21.
[20] N.G. Shang, P. Papakonstantinou, S. Sharma, G. Lubarsky, M.X. Li, D.W. McNeill, A.J. Quinn, W.Z. Zhou, R. Blackley, Controllable selective exfoliation of high-quality graphene nanosheets and nanodots by ionic liquid assisted grinding, Chem Commun 48(13) (2012) 1877-1879.
[21] J.L. Liu, H.P. Yang, S.G. Zhen, C.K. Poh, A. Chaurasia, J.S. Luo, X.Y. Wu, E.K.L. Yeow, N.G. Sahoo, J.Y. Lin, Z.X. Shen, A green approach to the synthesis of high-quality graphene oxide flakes via electrochemical exfoliation of pencil core, Rsc Advances 3(29) (2013) 11745-11750.
[22] K.S. Rao, J. Senthilnathan, Y.F. Liu, M. Yoshimura, Role of Peroxide Ions in Formation of Graphene Nanosheets by Electrochemical Exfoliation of Graphite, Sci Rep-Uk 4 (2014).
[23] Z.P. Li, Y.J. Mi, X.H. Liu, S. Liu, S.R. Yang, J.Q. Wang, Flexible graphene/MnO2 composite papers for supercapacitor electrodes, J Mater Chem 21(38) (2011) 14706-14711.
[24] L.L. Liu, Z.Q. Niu, L. Zhang, W.Y. Zhou, X.D. Chen, S.S. Xie, Nanostructured Graphene Composite Papers for Highly Flexible and Foldable Supercapacitors, Adv Mater 26(28) (2014) 4855-+.
[25] Y.J. Ping, Y.N. Gong, Q. Fu, C.X. Pan, Preparation of three-dimensional graphene foam for high performance supercapacitors, Prog Nat Sci-Mater 27(2) (2017) 177-181.
[26] W.W. Liu, J.D. Li, K. Feng, A. Sy, Y.S. Liu, L. Lim, G. Lui, R. Tjandra, L. Rasenthiram, G. Chiu, A.P. Yu, Advanced Li-Ion Hybrid Supercapacitors Based on 3D Graphene-Foam Composites, Acs Appl Mater Inter 8(39) (2016) 25941-25953.
[27] Y.L. Shao, M.F. El-Kady, C.W. Lin, G.Z. Zhu, K.L. Marsh, J.Y. Hwang, Q.H. Zhang, Y.G. Li, H.Z. Wang, R.B. Kaner, 3D Freeze-Casting of Cellular Graphene Films for Ultrahigh-Power-Density Supercapacitors, Adv Mater 28(31) (2016) 6719-+.
[28] Y.Q. Liu, B. Weng, J.M. Razal, Q. Xu, C. Zhao, Y.Y. Hou, S. Seyedin, R. Jalili, G.G. Wallace, J. Chen, High-Performance Flexible All-Solid-State Supercapacitor from Large Free-Standing Graphene-PEDOT/PSS Films, Sci Rep-Uk 5 (2015).
[29] I.K. Moon, B. Ki, S. Yoon, J. Choi, J. Oh, Lateral photovoltaic effect in flexible free-standing reduced graphene oxide film for self-powered position-sensitive detection(vol 6, 33525, 2016), Sci Rep-Uk 6 (2016).
[30] F. Liu, S. Song, D. Xue, H. Zhang, Folded structured graphene paper for high performance electrode materials, Advanced materials 24(8) (2012) 1089-94.
[31] H. Li, Y. Tao, X.Y. Zheng, Z.J. Li, D.H. Liu, Z. Xu, C. Luo, J.Y. Luo, F.Y. Kang, Q.H. Yang, Compressed porous graphene particles for use as supercapacitor electrodes with excellent volumetric performance, Nanoscale 7(44) (2015) 18459-18463.
[32] S.M. Jung, D.L. Mafra, C.T. Lin, H.Y. Jung, J. Kong, Controlled porous structures of graphene aerogels and their effect on supercapacitor performance, Nanoscale 7(10) (2015) 4386-4393.
[33] V. Strong, S. Dubin, M.F. El-Kady, A. Lech, Y. Wang, B.H. Weiller, R.B. Kaner, Patterning and Electronic Tuning of Laser Scribed Graphene for Flexible All-Carbon Devices, Acs Nano 6(2) (2012) 1395-1403.
[34] Y.Q. Zhao, D.D. Zhao, P.Y. Tang, Y.M. Wang, C.L. Xu, H.L. Li, MnO2/graphene/nickel foam composite as high performance supercapacitor electrode via a facile electrochemical deposition strategy, Mater Lett 76 (2012) 127-130.
[35] Z.Y. Zhang, F. Xiao, L.H. Qian, J.W. Xiao, S. Wang, Y.Q. Liu, Facile Synthesis of 3D MnO2-Graphene and Carbon Nanotube-Graphene Composite Networks for High-Performance, Flexible, All-Solid-State Asymmetric Supercapacitors, Adv Energy Mater 4(10) (2014).
[36] X. Huang, Z. Zeng, Z. Fan, J. Liu, H. Zhang, Graphene-based electrodes, Advanced materials 24(45) (2012) 5979-6004.
[37] C.H. Ji, K. Zhang, L. Li, X.X. Chen, J.L. Hu, D.Y. Yan, G.Y. Xiao, X.H. He, High performance graphene-based foam fabricated by a facile approach for oil absorption, J Mater Chem A 5(22) (2017) 11263-11270.

[38] J.F. Ping, Y.X. Wang, K. Fan, W.Z. Tang, J. Wu, Y.B. Ying, High-performance flexible potentiometric sensing devices using free-standing graphene paper, J Mater Chem B 1(37) (2013) 4781-4791.
[39] H. Bi, J. Chen, W. Zhao, S.R. Sun, Y.F. Tang, T.Q. Lin, F.Q. Huang, X.D. Zhou, X.M. Xie, M.H. Jiang, Highly conductive, free-standing and flexible graphene papers for energy conversion and storage devices, Rsc Advances 3(22) (2013) 8454-8460.
[40] S.F. Pei, H.M. Cheng, The reduction of graphene oxide, Carbon 50(9) (2012) 3210-3228.
[41] V.R.S.S. Mokkapati, D.Y.K. Imer, N. Yilmaz, V. Ozguz, I. Koyuncu, Protein mediated textile dye filtration using graphene oxide-polysulfone composite membranes, Rsc Advances 5(87) (2015) 71011-71021.
[42] Y.X. Xu, K.X. Sheng, C. Li, G.Q. Shi, Self-Assembled Graphene Hydrogel via a One-Step Hydrothermal Process, Acs Nano 4(7) (2010) 4324-4330.
[43] K.I. Ozoemena, S.W. Chen, Nanomaterials in Advanced Batteries and Supercapacitors Preface, Nanostruct Sci Techn (2016) V-Vii.
[44] X.B. Wang, Y.J. Zhang, C.Y. Zhi, X. Wang, D.M. Tang, Y.B. Xu, Q.H. Weng, X.F. Jiang, M. Mitome, D. Golberg, Y. Bando, Three-dimensional strutted graphene grown by substrate-free sugar blowing for high-power-density supercapacitors, Nat Commun 4 (2013).
[45] V. Patil, R.V. Dennis, T.K. Rout, S. Banerjee, G.D. Yadav, Graphene oxide and functionalized multi walled carbon nanotubes as epoxy curing agents: a novel synthetic approach to nanocomposites containing active nanostructured fillers, Rsc Advances 4(90) (2014) 49264-49272.
[46] D.W. Wang, F. Li, J.P. Zhao, W.C. Ren, Z.G. Chen, J. Tan, Z.S. Wu, I. Gentle, G.Q. Lu, H.M. Cheng, Fabrication of Graphene/Polyaniline Composite Paper via In Situ Anodic Electropolymerization for High-Performance Flexible Electrode, Acs Nano 3(7) (2009) 1745-1752.
[47] Z. Weng, Y. Su, D.W. Wang, F. Li, J.H. Du, H.M. Cheng, Graphene-Cellulose Paper Flexible Supercapacitors, Adv Energy Mater 1(5) (2011) 917-922.
[48] S.B. Ye, B. Chen, J.C. Feng, Fracture Mechanism and Toughness Optimization of Macroscopic Thick Graphene Oxide Film, Sci Rep-Uk 5 (2015).
[49] Z.Q. Niu, J. Chen, H.H. Hng, J. Ma, X.D. Chen, A Leavening Strategy to Prepare Reduced Graphene Oxide Foams, Advanced materials 24(30) (2012) 4144-4150.
[50] Y.Q. Li, T. Yu, T.Y. Yang, L.X. Zheng, K. Liao, Bio-Inspired Nacre-like Composite Films Based on Graphene with Superior Mechanical, Electrical, and Biocompatible Properties, Advanced materials 24(25) (2012) 3426-3431.
[51] H. Huang, Y. Xia, X.Y. Tao, J. Du, J.W. Fang, Y.P. Gan, W.K. Zhang, Highly efficient electrolytic exfoliation of graphite into graphene sheets based on Li ions intercalation-expansion-microexplosion mechanism, J Mater Chem 22(21) (2012) 10452-10456.
[52] Y.X. Xu, C.Y. Chen, Z.P. Zhao, Z.Y. Lin, C. Lee, X. Xu, C. Wang, Y. Huang, M.I. Shakir, X.F. Duan, Solution Processable Holey Graphene Oxide and Its Derived Macrostructures for High-Performance Supercapacitors, Nano Lett 15(7) (2015) 4605-4610.
[53] W.W. Liu, X.B. Yan, J.W. Lang, C. Peng, Q.J. Xue, Flexible and conductive nanocomposite electrode based on graphene sheets and cotton cloth for supercapacitor, J Mater Chem 22(33) (2012) 17245-17253.
[54] I.K. Moon, J. Lee, R.S. Ruoff, H. Lee, Reduced graphene oxide by chemical graphitization, Nat Commun 1 (2010) 73.
[55] M.H. Liang, J. Wang, B. Luo, T.F. Qiu, L.J. Zhi, High-Efficiency and Room-Temperature Reduction of Graphene Oxide: A Facile Green Approach Towards Flexible Graphene Films, Small 8(8) (2012) 1180-1184.
[56] I.Y. Jeon, D.S. Yu, S.Y. Bae, H.J. Choi, D.W. Chang, L.M. Dai, J.B. Baek, Formation of Large-Area Nitrogen-Doped Graphene Film Prepared from Simple Solution Casting of Edge-Selectively Functionalized Graphite and Its Electrocatalytic Activity, Chem Mater 23(17) (2011) 3987-3992.
[57] H.P. Cong, X.C. Ren, P. Wang, S.H. Yu, Flexible graphene-polyaniline composite paper for high-performance supercapacitor, Energ Environ Sci 6(4) (2013) 1185-1191.

[58] X. Zhao, C.M. Hayner, M.C. Kung, H.H. Kung, Flexible Holey Graphene Paper Electrodes with Enhanced Rate Capability for Energy Storage Applications, Acs Nano 5(11) (2011) 8739-8749.
[59] G.W. Wang, H. Uyama, Facile synthesis of flexible macroporous polypropylene sponges for separation of oil and water, Sci Rep-Uk 6 (2016).
[60] C.P. Ruan, K.L. Ai, X.B. Li, L.H. Lu, A Superhydrophobic Sponge with Excellent Absorbency and Flame Retardancy, Angew Chem Int Edit 53(22) (2014) 5556-5560.
[61] J.K. Yuan, X.G. Liu, O. Akbulut, J.Q. Hu, S.L. Suib, J. Kong, F. Stellacci, Superwetting nanowire membranes for selective absorption, Nat Nanotechnol 3(6) (2008) 332-336.
[62] S.J. Choi, T.H. Kwon, H. Im, D.I. Moon, D.J. Baek, M.L. Seol, J.P. Duarte, Y.K. Choi, A Polydimethylsiloxane (PDMS) Sponge for the Selective Absorption of Oil from Water, Acs Appl Mater Inter 3(12) (2011) 4552-4556.
[63] Z. Li, Z. Xu, Y.J. Liu, R. Wang, C. Gao, Multifunctional non-woven fabrics of interfused graphene fibres, Nat Commun 7 (2016).

CHAPTER III

3 MnO_2 nanoflowers-deposited graphene paper electrode for enhanced capacitance performance *

3.1 Introduction

Electrochemical capacitors, also known as supercapacitors, are potential energy storage devices that have attracted extensive investigations owing to their high power density, fast charging/discharging rate, long cycle life (>100,000 cycles), and low cost of fabrication [1, 2]. However, compared to other energy storage devices, supercapacitors suffer from lower energy density, which limits their extensive commercial applications [3, 4]. Much research has been directed at improving the energy density of supercapacitor electrode materials, primarily using carbonaceous composites such as graphene foam/paper, carbon nanotube (CNT) film, and carbon fiber cloth and other conducting polymers or transition metal oxides [5, 6].

Oxides of ruthenium, nickel, and manganese etc. are used as supercapacitor electrode materials. Of these, the property of manganese allows it to be present in different valence states (+2, +3, +4) and form various stable oxides (MnO, Mn_3O_4, Mn_2O_3, MnO_2) with a variety of electrochemical properties, crystal structures, morphology, porosity and textures [7]. Among them, MnO_2 has the greatest potential due to its stability and different structural forms, α-, β-, γ-, and λ-type, etc.[8]. MnO_2 is also naturally abundant, inexpensive and environmentally benign [9]. However, low electrical conductivity (10^{-5} to 10^{-6} $S \cdot cm^{-1}$), low cyclic stability, and low rate capacity have limited the applications of MnO_2 [10]. To overcome these limitations, an effective strategy is to combine carbonaceous material with manganese nanostructures [11]. Incorporating highly conductive materials such as graphene, CNTs, or conductive polymers can improve the

*Submitted to ACS Applied Nano Materials

performance of MnO_2 electrodes by increasing their chemical stability and electrical conductivity [12]. Additionally, MnO_2 nanostructures offer high accessible surface area for reversible redox reaction and reduce the electron transport distance [13]. Thus, combination of graphene and MnO_2 nanocomposite is a promising candidate for supercapacitor electrode.

Graphene, an outstanding two-dimensional (2D) carbon structure, has attracted strong considerations because of its exceptional properties such as lightweight, high electrical and thermal conductivity, high surface-to-volume ratio, high mechanical strength, chemical stability, inherent hydrophobicity, etc. [14, 15]. Graphene is also a standout amongst the most materials for flexible electronics and energy-related devices [16], because it can be integrated into flexible, interconnected and free-standing three-dimensional (3D) network structures such as paper [1], foam [17], film [18], aerogels [19], hydrogels [20], or other substrates [21]. Thus, 3D porous graphene structures are suitable platforms to fabricate flexible supercapacitors [22]. However, cost-effective and environmentally friendly methods are required to afford large-scale manufacturing of graphene and broaden its applications [23]. In this vein, graphene paper (GrP) we have fabricated [24] is an easy-to-prepare, green and low-cost substrate. Also, GrP possesses low sheet resistance, high thermal and mechanical stability, and high capacitance compared to other reported flexible and free-standing 3D graphene network structures.

Herein, we report a green, rapid, and cost-effective method to produce flexible, free-standing, and highly conductive supercapacitor electrodes made of GrP decorated with MnO_2 nanoflowers for enhanced charge storage. GrP was prepared via electrochemical exfoliation of graphite sheets, which were then self-assembled using vacuum filtration. MnO_2 nanoflowers were electrochemically deposited on GrP. The amount of MnO_2 nanoflowers used was optimized by

varying the number of electrodeposition cycles (1, 3, 5, 7, 10, 15, and 20). The electrode material obtained after 10 cycles of MnO_2 deposition on GrP (GrP/10-MnO_2), the optimal composition, exhibited an excellent capacitive performance with high specific capacitance of 385.2 $F \cdot g^{-1}$ at 1 $mV \cdot s^{-1}$ in 0.1 M Na_2SO_4 electrolyte and outstanding capacitance retention after 5,000 consecutive cycles. Taking advantage of both superior mechanical and capacitance behavior of GrP and GrP/10-MnO_2 electrodes, a flexible solid-state supercapacitor (SASc) device was assembled using GrP/10-MnO_2 and GrP as positive and negative electrode, respectively. The fabricated SASc device exhibited not only high areal capacitances of 76.8 mF cm^{-2} at a current density of 0.05 mA cm^{-2} but also excellent cycling stability of 82.2% after 5000 consecutive GCD cycles. This flexible supercapacitor can also deliver a high energy density of 6.14 $mWh \cdot cm^{-2}$ with a power density of 36 $mW \cdot cm^{-2}$. This research represents a new direction for exploring the potential of free-standing GrP and its nanocomposites in flexible energy-storage systems.

3.2 Experimental section

3.2.1 Materials

Graphite sheets were purchased from Graphitestore, Inc. (USA). Manganese (II) acetate ($Mn(CH_3COO)_2$) was obtained from Sigma-Aldrich (St. Louis, MO, USA). Sulfuric acid (H_2SO_4) was acquired from Acros chemicals (NJ, USA). Sodium sulfate (Na_2SO_4) was purchased from Fisher Chemicals (Fair Lawn, NJ, USA). Deionized (DI) water (18 MΩ·cm) was used in all experiments.

3.2.2 Preparation of GrP and GrP/x-MnO_2 electrodes

GrP was fabricated as described in detail in [24]. Polyethylene terephthalate (PET) substrates were attached to the as-synthesized GrP using two-sided carbon tape and a copper foil with and alligator

clip for a good electrical contact as shown Figure **3.1**. Then, MnO_2 was deposited onto the GrP electrodes potentiodynamically through CV cycles with a potential sweeping from 0.0 to 1.4 V at 50 mV·s-1 for different electrodeposition cycles (1, 3, 5, 7, 10, 15, and 20) in a solution containing 50 mM $Mn(CH3COO)_2$ and 100 mM Na_2SO_4 using platinum wire, Ag/AgCl (1 M KCl) and GrP electrode, as counter, reference and working electrode, respectively.

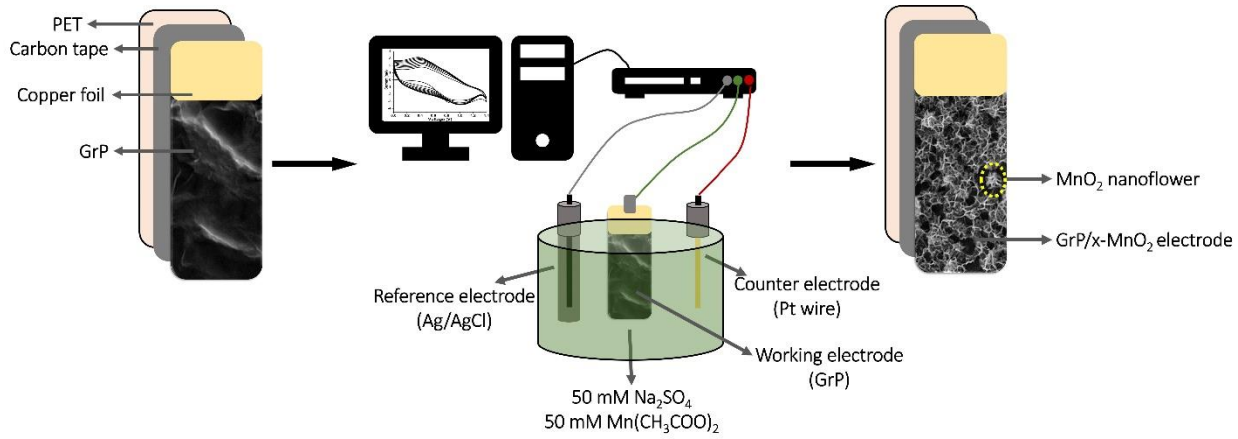

Figure 3.1 Fabrication process of GrP/x-MnO_2 electrode using GrP via electrochemical deposition

3.2.3 Electrochemical Measurements

Electrochemical measurements were performed using an electrochemical workstation (CH-660D, CH Instruments Inc., Austin, TX, USA) in a three-electrode configuration with Ag/AgCl (1 M KCl), platinum wire and GrP/x-MnO_2 as reference, counter, and working electrode, respectively. Galvanostatic charge/discharge (GCD) and cyclic voltammetry (CV) measurements were carried out at room temperature in 50 mM Na_2SO_4 as electrolyte. The electrodes were also characterized by electrochemical impedance spectroscopy (EIS) in 0.1 M KCl containing 5 mM redox couple ferrocyanide/ferricyanide ($[Fe(CN)_6]^{3-/4-}$). First cycle of the CV measurements was always discarded

3.2.4 Material Characterization

Exfoliated graphite sheets were characterized via Fourier transform infrared (FT-IR) (Spectrum 100, Perkin Elmer), X-ray photoelectron (XPS) (Thermo Scientific K-Alpha), Raman (LabRAM Aramis Horiba Jobin Yvon Confocal Raman Microscope) (wavelength: 532 nm) spectroscopies using Tektronix PS280 DC power supply in 0.1 M phosphate-buffered saline (PBS) (pH 7.0). The surface morphology studies were performed using a field emission scanning electron microscope (FE-SEM) (LEO1530, Gemini FE-SEM, Carl Zeiss) at 3 kV. Thickness of individual graphene sheets and precise diameter of MnO_2 nanoflowers deposited on GrP, were measured using an AFM (RTESP-300, Bruker). A dilute solution of graphene (0.01 $mg \cdot mL^{-1}$) was dropped onto a freshly cleaved silicon wafer surface and then rinsed with DI water or acidic solution (%5 HCl solution) three times, followed by drying at room temperature under nitrogen atmosphere. AFM images of graphene were obtained in tapping mode using a cantilever tip. Imaging was implemented using a silicon nitride cantilever, which has a nominal radius of curvature R ≈ 20 nm, spring constant of ~40 $N \cdot m^{-1}$, and the resonant frequency of ~300 kHz. The cantilever was calibrated by thermal tuning prior to use [25]. The AFM images were analyzed using the Nanoscope Analysis software (Bruker). All AFM experiments were performed at room temperature.

3.3 Results

3.3.1 Characterization of GrP and GrP/x-MnO_2

Recently, our group reported a novel synthesis method for graphene paper (GrP) which possesses low sheet resistance, high thermal and mechanical stability, and high capacitance compared to other reported flexible and free-standing 3D graphene network structures [24]. Exfoliated graphene sheets which forms GrP by self-assembly were further characterized by AFM in this letter. 2D and 3D views of the exfoliated graphene sheets are presented in **Figure A 3.1a** and

Figure A 3.2b, respectively. The enlarged view of one graphene sheet is shown in **Figure A 3.3c**. The height profile across the graphene sheet (**Figure A 3.4d**) reveals its thickness is under 5 nm. The thickness of single layer of graphene sheets, measured with AFM, has been reported as 1.5 ±0.5 nm [26]. Although a layer carbon atom is only 0.34 nm thick, a layer of graphene is thicker due to the electrostatic force between the graphene layer and the cantilever as well as the surface contaminations such as water and other surfactant molecules [26]. Taking these factors into account, we conclude that the graphene sheets we exfoliated can contain one, two, or few layers of graphene.

GrP was fabricated as described in detail in our previous report [24]. Polyethylene terephthalate (PET) substrates were attached to the as-synthesized GrP using two-sided carbon tape and a copper foil with and alligator clip for a good electrical contact as shown in **Figure 3.1**. Then, MnO_2 was deposited onto the GrP electrodes potentiodynamically through CV cycles with a potential sweeping from 0.0 to 1.4 V at 50 $mV \cdot s^{-1}$ for different electrodeposition cycles (1, 3, 5, 7, 10, 15, and 20) in a solution containing 50 mM $Mn(CH_3COO)_2$ and 100 mM Na_2SO_4 using platinum wire, Ag/AgCl (1 M KCl) and GrP electrode, as counter, reference and working electrode, respectively. As an example, CVs of GrP/10-MnO_2 exhibited two anodic peaks were observed at 0.8 and 1.1 V during the first anodic scan (**Figure A 3.5**), which corresponded to irreversible reaction of Mn^{2+}. As number of cycles increased, the anodic peak at 1.1 V and cathodic peak at 0.42 V increased due to electro-oxidation of Mn^{2+}, which confirms the successful deposition of MnO_2 on the GrP as expressed in Equations (1) - (3) [27-29]:

$$Mn^{2+} \rightarrow Mn^{3+} + e^{-} \qquad (1)$$

$$Mn^{3+} + 2H_2O \rightarrow MnOOH + 3H^{+} \qquad (2)$$

$$MnOOH \rightarrow MnO_2 + H^+ + e^- \quad (3)$$

After the deposition of MnO_2, the electrodes were thoroughly washed with 5 % HCl solution and DI water several times and air dried at 60 °C for 30 min. The electrodes were labelled as GrP/x-MnO_2 where x is the number of MnO_2 deposition cycles used in electrode preparation. The **Table A 3.1** shows the mass loading of MnO_2 for each electrode.

To verify the nature of interactions between GrP and MnO_2, FT-IR, and Raman spectra of GrP, and GrP/x-MnO_2 electrodes were obtained. In the FT-IR spectra (**Figure 3.2a**), OH stretch (~3430 cm−1), O-C=O stretch (2326 cm−1), C=O stretch (1725 cm−1), and C=C stretch (1642

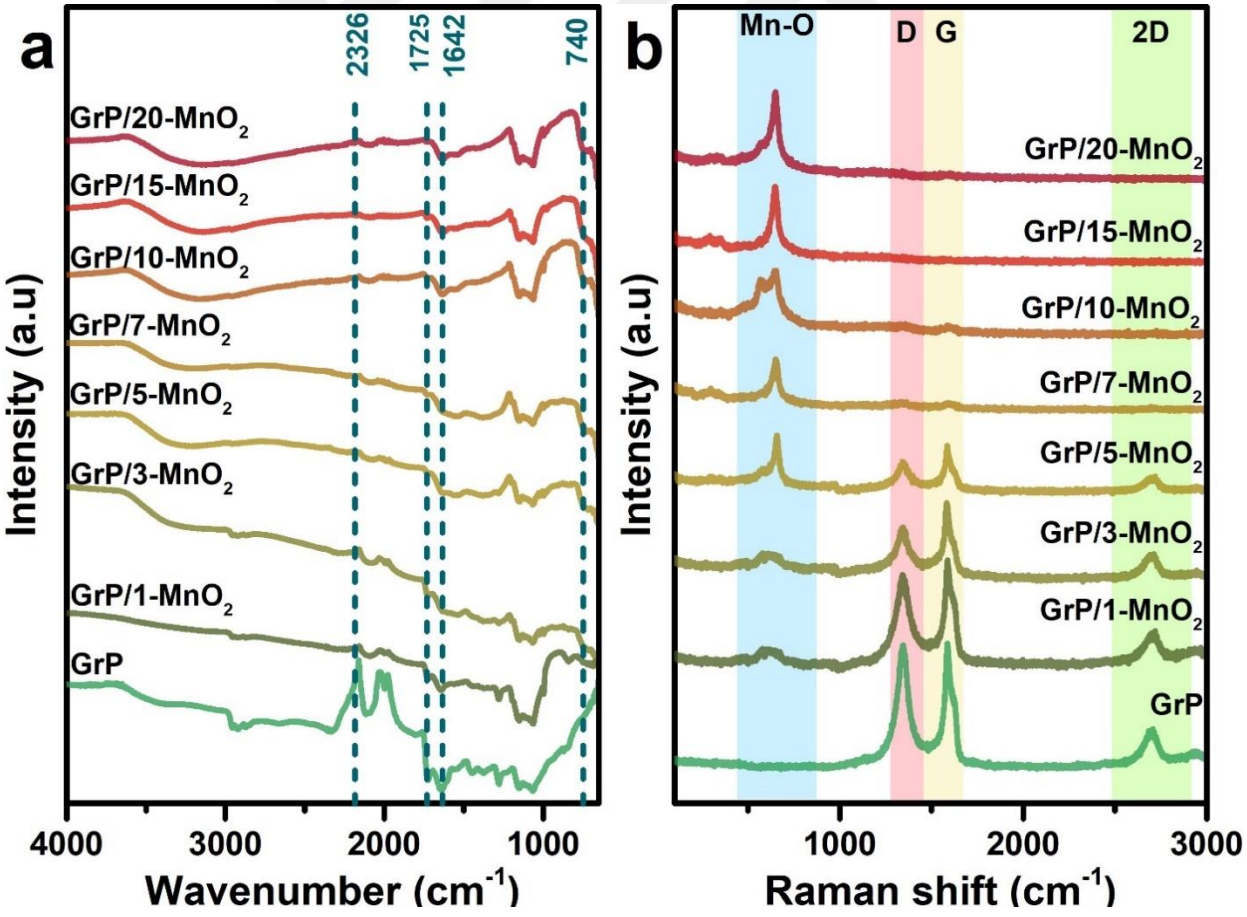

Figure 3.2 (a) FT-IR and **(b)** Raman spectra for GrP and GrP/x-MnO_2 electrodes.

cm^{-1}) peaks were observed. After deposition of MnO_2 on GrP, the peak at 740 cm^{-1} increased due to Mn-O vibration [30]. The Raman spectra (**Figure 3.2b**) of GrP and GrP/x-MnO_2 electrodes show a decrease in intensities of D band at 1343 cm^{-1}, G band at 1588 cm^{-1} and 2D band at 2710 cm^{-1} as the MnO_2 deposition cycles increased. In contrast, the intensity of the band at 643 cm^{-1} increased with the number of MnO_2 deposition, which is an indication of the MnO_2 formation on GrP [10].

Then, the GrP/10-MnO_2 were further characterized with XPS. The spectrum in **Figure 3.3a** shows the peaks of C1s, O1s, and Mn ($2p^{3/2}$, $2p^{1/2}$, 3p, 3s) for GrP/10-MnO_2, illustrating the successful formation of MnO_2 nanoflowers on the surface of GrP. The broad Mn $2p_{1/2}$ (653.8 eV) and $2p_{3/2}$ (642.0 eV) peaks in **Figure 3.3b** is due to the overlap of Mn^{3+} and Mn^{4+} ionic states. Mn $2p_{1/2}$ and $2p_{3/2}$ peaks deconvoluted into two peaks 641.1 (Mn^{3+}), 642.4 (Mn^{4+}) eV using the XPS best peak fitting with Gaussian modes. The relative percent of Mn^{3+}/Mn^{4+} ratio was calculated by peak area ratios which estimated to be about 34% on the surface of the as-prepared GrP/10-MnO_2 electrode. Additionally, the separation between Mn $2p^{3/2}$ and Mn $2p^{1/2}$ in MnO_2 was 11.8 eV, which is in good agreement with reported results [10, 13]. The high-resolution O 1s spectrum (**Figure 3.3c**) shows peaks at 529.7 and 531.6 eV, attributed to Mn-O-Mn, and Mn-O-H bonding, respectively [31]. The Mn-O-Mn/Mn-O-H ratio was also calculated by peak area ratios which found to be 1.72. It suggests that Mn is primarily exist in the oxide form (MnO_2) at the surface of GrP/10-MnO_2 electrode. The high-resolution C 1s spectrum of GrP/10-MnO_2 is shown in **Figure 3.3d**. Compared to the C 1s spectrum of GrP (**Figure A 3.8**), relatively weak peaks of oxidized carbon species (C-O and O-C=O) were observed.

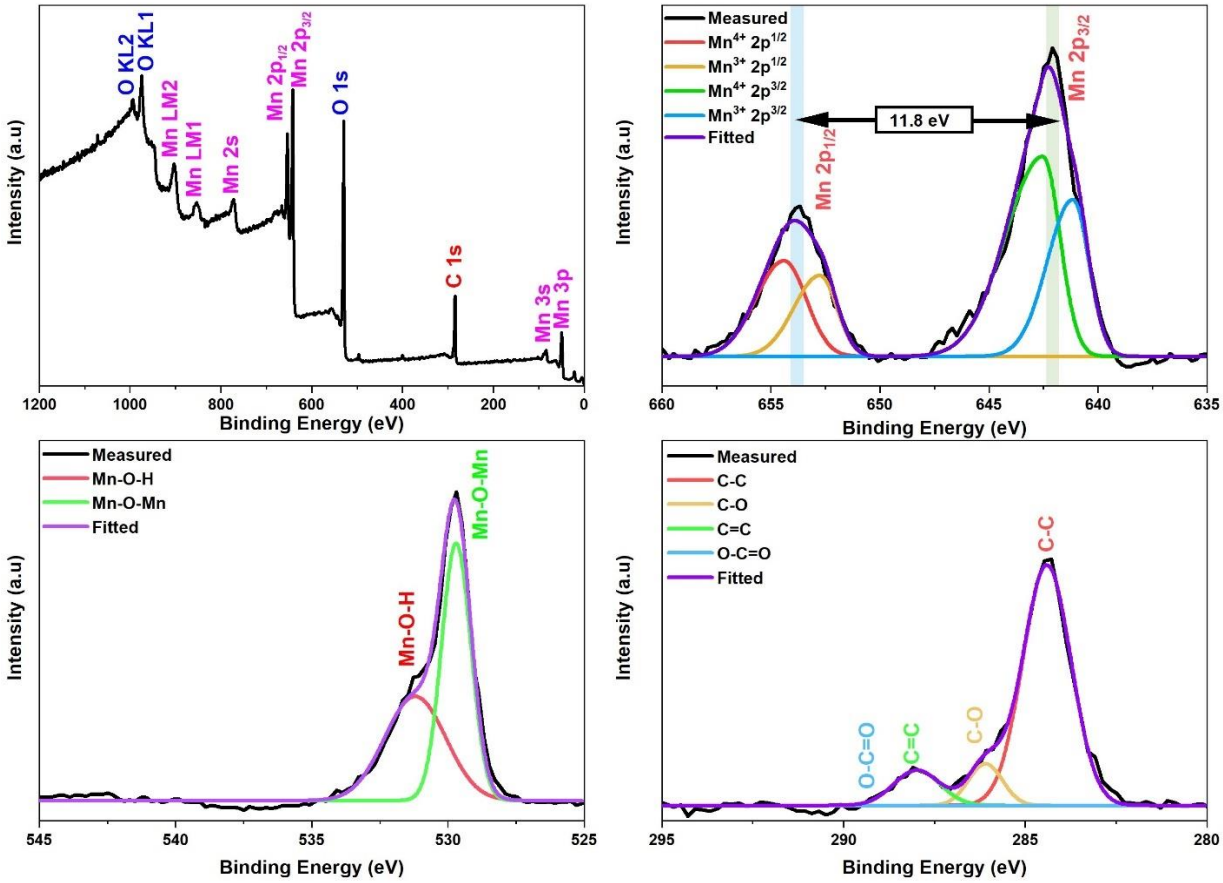

Figure 3.3 XPS spectra for the GrP/10-MnO_2 (a) survey spectrum and high-resolution spectra for (b) Mn 2p, (c) O 1s, and (d) C 1s.

The X-ray diffraction (XRD) patterns of GrP and GrP/10-MnO_2 are shown in **Figure 3.4**. The diffraction peak of GrP was observed at around 25° which can be indexed to (002) plane reflection of graphene-based materials [32]. The GrP/10-MnO_2 showed sharp diffraction peaks at 22.4°, 34.6°, 36.9°, 38.2°, 42.49°, 56.4°, and 66.4°, which could be indexed to the characteristic peaks (120), (031), (131), (230), (300), (160) and (421) plane reflections of γ-MnO_2 (JCPDS no. 14-0644), respectively [33-35]. Beside to the γ-MnO_2 peaks, the weak peaks located at ~26°, 33.9°, 37.3°, 51.6°, 55.6°, and 61.9° observed due to (11−1), (020), (200), (12−1), (022), (22−2), and (131) plane reflections of MnOOH (JPSDS no. 41-1379), respectively

[36, 37]. Both γ-MnO_2 and MnOOH data are well match with those reports in literature. The presence of (002) plane reflection of graphene in the XRD pattern of the GrP/10-MnO_2 electrode suggests the formation of the highly crystalline γ-MnO_2 and MnOOH on the surfaces of GrP.

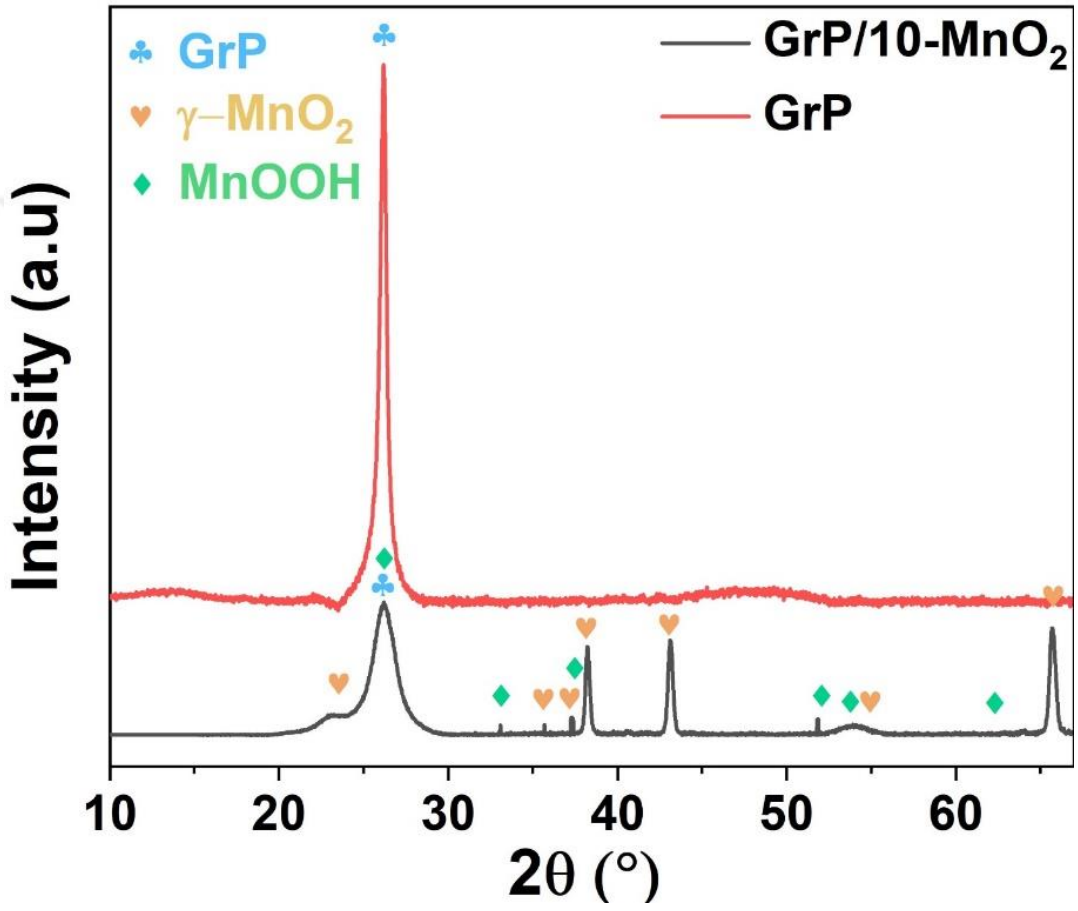

Figure 3.4 XRD spectra of GrP and GrP/10-MnO_2 electrodes.

The surface morphology of GrP and GrP/x-MnO_2 electrodes obtained with FE-SEM (**Figure 3.5**) shows an interconnected 3D porous structure with a typical rippled and crumpled morphology of GrP (**Figure 3.5a** and **Figure 3.5b**), which is favorable for loading active materials. After deposition of MnO_2, flower-like morphology with nanostructured petal-shaped

nanosheet agglomerates (**Figure 3.5c - p**), in which the size and number of MnO_2 nanoflowers are proportional to the number of deposition cycles.

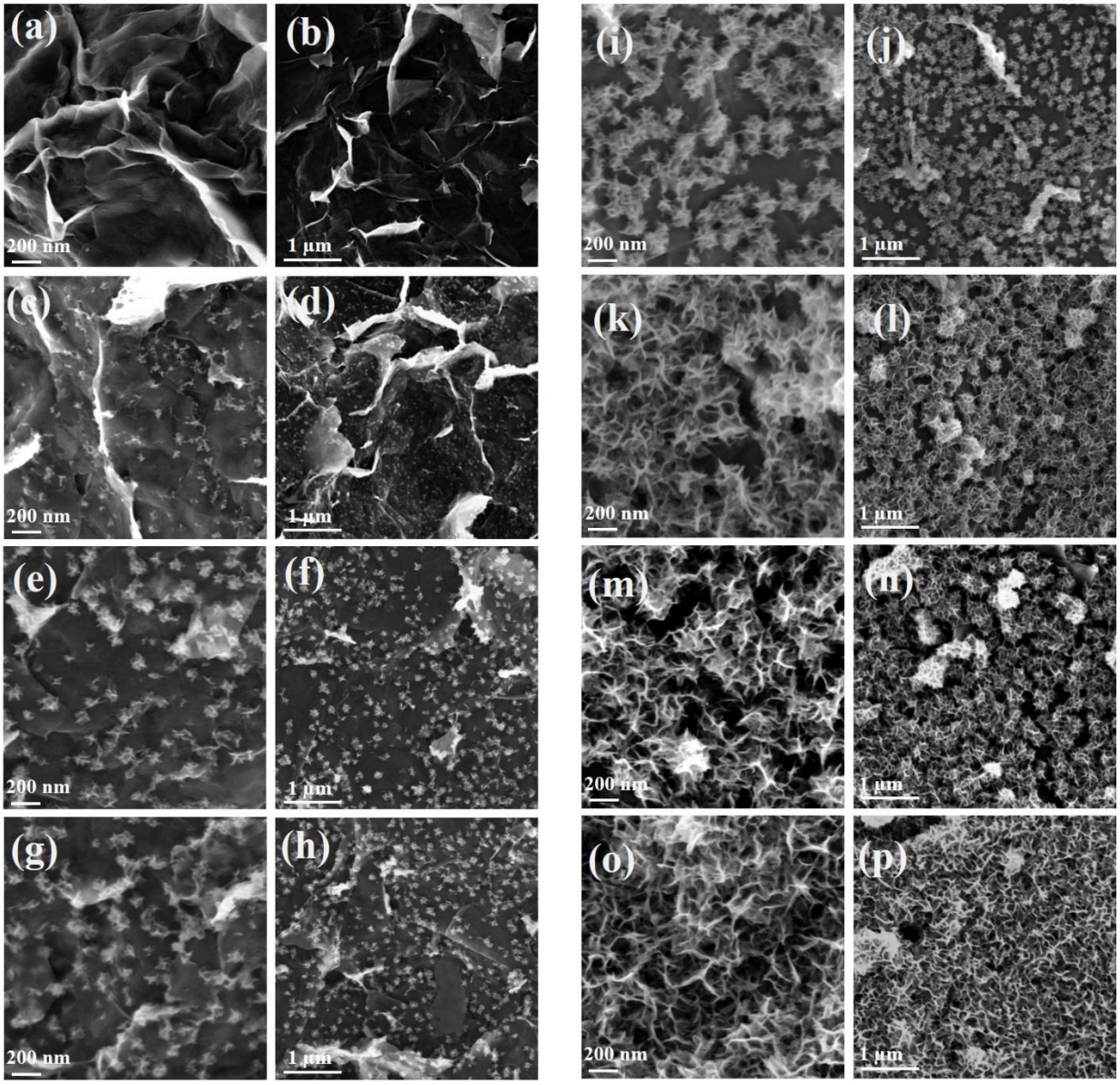

Figure 3.5 SEM images of **(a-b)** GrP **(c-d)** GrP/1-MnO_2 **(e-f)** GrP/3-MnO_2 **(g-h)** GrP/5-MnO_2 **(i-j)** GrP/7-MnO_2 **(k-l)** GrP/10-MnO_2 **(m-n)** GrP/15-MnO_2 **(o-p)** GrP/20-MnO_2 samples with different magnifications.

The size of MnO_2 nanoflowers on the GrP were further analyzed by AFM. As an example, 2D and 3D views of GrP/7-MnO_2 are presented in **Figure 3.6a** and **Figure 3.6b**, respectively. They reveal a uniform coating of MnO_2 nanoflowers onto GrP. The height profile indicates that size of individual MnO_2 nanoparticles range from 150-200 nm and their heights range from 20-24 nm (**Figure 3.6c** and **Figure 3.6d**).

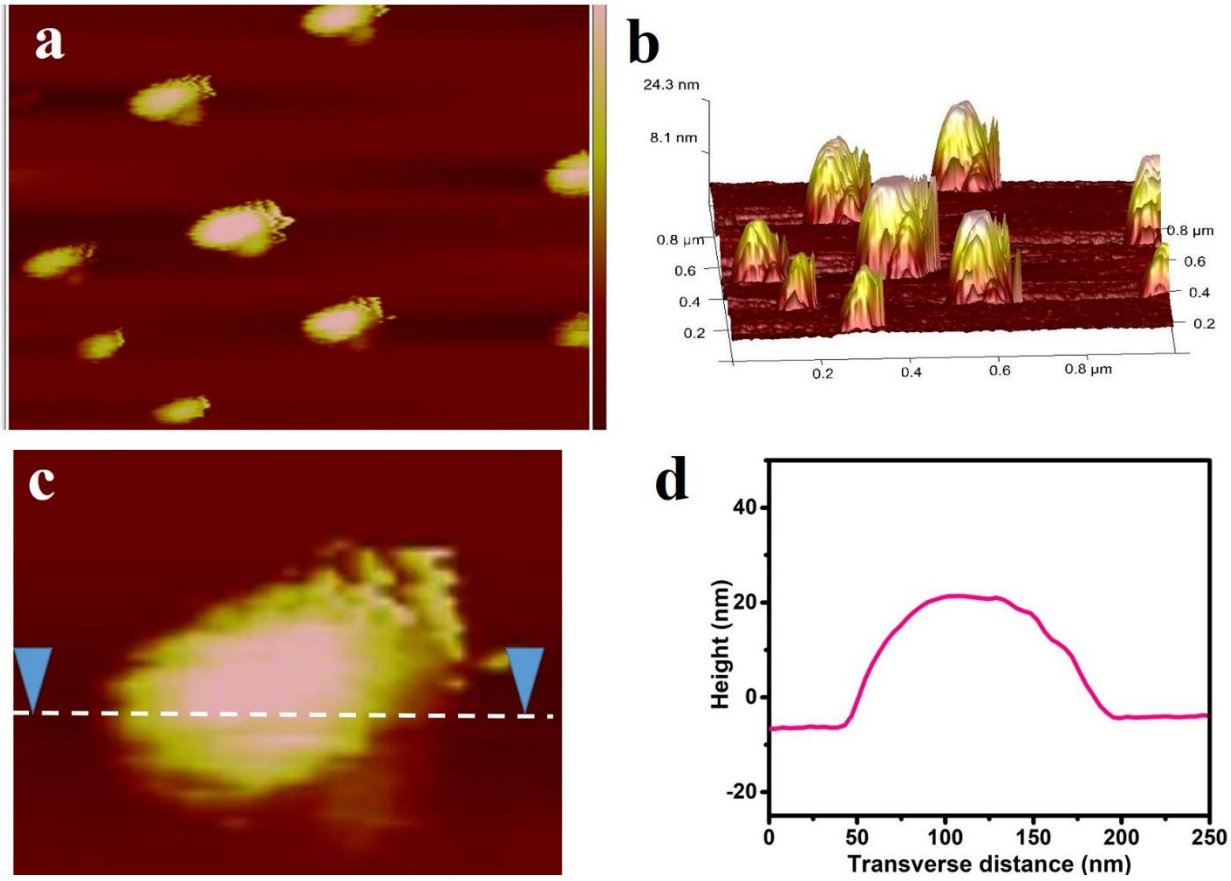

Figure 3.6 (a) 2D and **(b)** 3D AFM images of GrP/10-MnO_2. **(c)** enlarged view of MnO_2 nanoflower and **(d)** its height profile.

3.3.2 Electrochemical measurement of GrP and GrP/x-MnO_2

CV curves for GrP and GrP/x-MnO_2 electrodes at scan rates from 1 to 30 $mV \cdot s^{-1}$ are presented in **Figure A 3.9**, which exhibited rectangle-like shapes. It is important to note that the CV curves do not show any significant redox peak towards 0 V vs. Ag/AgCl, even under low scan rate (1 $mV\ s^{-1}$). This is attributed to the diffusion limited redox reactions (faradic) (e.g., reduction of Mn^{4+} to Mn^{3+}) which is slower than non-diffusion limited double layer charging process (non-faradic) [38]. To compare their electrochemical performance, CV curves at a scan rate of 5 $mV \cdot s^{-1}$ in 50 mM Na_2SO_4 solution were shown in **Figure 3.7a**. The CV curve of GrP/10-MnO_2 electrode was rectangular-shaped and enclosed the largest area, which is an indication of the best capacitive performance of all the fabricated electrodes. Then, GrP/10-MnO_2 electrode was investigated at various scan rates from 1 to 30 $mV \cdot s^{-1}$, as shown in **Figure 3.7b**. The symmetrical and horizontal CV curves indicate an ideal capacitive behavior of supercapacitors. The C_S value of GrP and GrP/x-MnO_2 electrodes can be calculated using their CV data by the following equation (4):

$$C_S = \frac{\int_{V_a}^{V_c} I(V)dV}{mv(V_a - V_c)} \qquad (4)$$

where C_S is the specific capacitance ($F \cdot g^{-1}$), m is the mass of active materials on the electrodes (g), V is the scan rate of CV curves ($V\ s^{-1}$) and (V_a -V_c) is the potential window. The results show that C_S values increase with decreasing scan rates (**Figure 3.7c** and **Figure 3.7d**), and with MnO_2 deposition up to 10 cycles. The decrease in C_S past 10 cycles of MnO_2 deposition is attributed to the poor conductivity associated with the abundance of MnO_2 coating on GrP. Additionally, GrP capacitance contribution (CC) in the GrP/x-MnO_2 electrodes are given in **Figure A *3.10***. At the lower deposition cycles, CC is very high and the CC decreases while number of deposition cycle increase. The CC of GrP is as low as 18% for GrP/10-MnO_2 electrode.

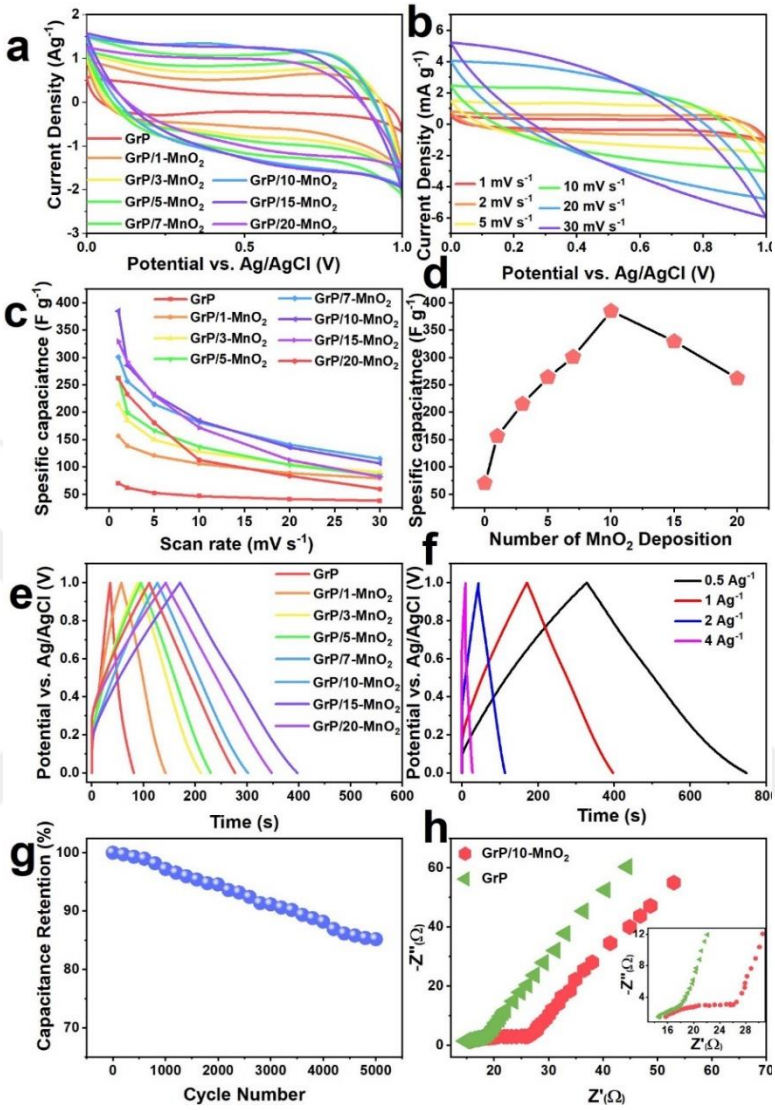

Figure 3.7 CVs in 50 mM Na_2SO_4 solution at different scan rates of **(a)** GrP and GrP/x-MnO_2 electrodes (x=number of MnO_2 deposition cycles) and **(b)** GrP/10-MnO_2. The effect of scan rate **(c)** and number of MnO_2 deposition cycles at 1 $mV \cdot s^{-1}$ **(d)** on specific capacitance of GrP and GrP/x-MnO_2 electrodes. **(e)** Galvanostatic charge/discharge curves for GrP and GrP/x-MnO_2 electrodes at a current density of 1 $A \cdot g^{-1}$ **(f)** Galvanostatic charge/discharge curves for GrP/10-MnO_2 at different current densities **(g)** Cycle life of GrP/10-MnO_2 electrodes at a current density of 4 $A \cdot g^{-1}$. **(h)** Nyquist plots of GrP and GrP/10-MnO_2 in 0.1 M KCl solution containing 5 mM $[Fe(CN)_6]^{3-/4-}$ with frequency range from 0.1 to 100,000 Hz.

The GCD curves, obtained in 50 mM Na_2SO_4 with the potential range of 0 - 0.1 V at 0.5 $A{\cdot}g^{-1}$, were used to characterize the electrochemical properties of the as-synthesized GrP and GrP/x-MnO_2 electrodes (**Figure 3.7e**). The GrP/10-MnO_2 electrode exhibited longer charge/discharge time compared to GrP and other electrodes, which is in good agreement with the CV results. The GCD curves at a current density of 0.25, 0.5, 1, and 4 $A{\cdot}g^{-1}$ were performed for GrP/10-MnO_2. As illustrated in **Figure 3.7f**, the charge–discharge curves are equilateral triangles in shape, indicating high reversibility of the hybrid material during the charge/discharge process with a rapid I-V response. Energy (E, $W{\cdot}h{\cdot}kg^{-1}$) and power density (P, $W{\cdot}kg^{-1}$) of GrP/10-MnO_2 are also calculated based on the GCD curves using Equation (5):

$$P = \frac{E}{t} = \frac{I*\Delta V}{m} \qquad (5)$$

Where, I is the applied constant current (A), ΔV potential window (V), t is the discharge time (h), and m is the mass of active materials (kg). GrP/10-MnO_2 exhibited excellent power density up to 3.72 $kW{\cdot}kg^{-1}$ at 4 $A{\cdot}g^{-1}$ and a high energy density up to 28.9 $W{\cdot}h{\cdot}kg^{-1}$ at 0.25 $A{\cdot}g^{-1}$. The electrochemical stability of GrP/10-MnO_2 electrode was studied using GCD over 5000 cycles at a current density of 4 $A{\cdot}g^{-1}$. The capacitance retention of GrP/10-MnO_2 electrode retained 85.4% of the capacitance after 5000 consecutive cycles as shown in **Figure 3.7g**. The morphology of the GrP/10-MnO_2 was tested after 5000 consecutive cycles via SEM analysis, and the morphology of MnO_2 on the surface of GrP shows no significant change as shown **Figure A 3.11**. Moreover, the capacitance behavior of GrP/10-MnO_2 are comparable to that of graphene/MnO_2 composite based systems as shown in **Table 3.1** [9-11, 13, 31, 39, 40].

Table 3.1 Comparing the capacitive characteristics of the synthesized GrP/10-MnO_2 electrode and other graphene-MnO_2 composites reported in the literature

Sample[a]	**C_s ($F \cdot g^{-1}$)**	**Current density or Scan rate**	**Capacitance retention**	**Ref.**
GMCP	256	0.5 $A \cdot g^{-1}$	74% (1000 cycles)	[10]
HRG/MnO_2	211.5	2 $mV \cdot s^{-1}$	75% (1000 cycles)	[11]
RGO/MnO_2–CNTs	304	1 $A \cdot g^{-1}$	97.5% (1200 cycles)	[13]
MnC-G	193	0.2 $A \cdot g^{-1}$	~70% (1300 cycles)	[31]
Gr-MnO_2	310	2 $mV \cdot s^{-1}$	95.4% (15000 cycles)	[39]
FRGO-p-MnO_2	188	0.25 $A \cdot g^{-1}$	89% (1000 cycles)	[40]
GrP/10-MnO_2	385.2	1 $mV \cdot s^{-1}$	85.4% (5000 cycles)	This work

a. GMCP: Graphene/MnO_2 composite papers, RGO/MnO_2–CNTs: Reduced graphene oxide (RGO)/birnessite-type MnO_2 nanoarchitectures, FRGO-p-MnO_2: poly (diallyldimethylammonium chloride) (PDDA)/RGO/MnO_2 nanosheets, HRG/MnO_2: Hydrothermally reduced graphene/MnO_2, Gr-MnO_2: Graphene/ MnO_2, MnC-G: MnO_2-coated carbon nanotubes/ reduced graphene oxide composite, MnO_2–CNT–graphene–Ni: Carbon nanotube–graphene hybrids coated Ni foam with MnO_2 immobilization.

The electrochemical properties of GrP and GrP/10-MnO_2 were further evaluated with EIS by using the redox couple $Fe(CN)_4^{4-}/Fe(CN)_6^{3-}$ as the electrolyte and **Figure 3.7h** shows the Nyquist plots of GrP and GrP/10-MnO_2. The redox couple $Fe(CN)_4^{4-}/Fe(CN)_6^{3-}$ plays an very important role in EIS, due to their electrochemical oxidation product (ferricyanide) and their inert property, namely less interaction between GrP-MnO_2 and Fe^{3+}/Fe^{2+} [41]. Herein, we adopted it as electrolyte in EIS experiment. The x-intercept in the high-frequency region corresponds to combined resistance (R_s= ~15 Ω) containing ionic resistance of electrolyte, contact resistance between electrode and current collector. The diameter of semicircular arcs corresponds to the charge transfer resistance (R_{ct}). A bigger diameter arc indicates a larger R_{ct}. The value of R_{ct} for GrP and GrP/10-MnO_2 were approximately 2.1 and 9.8 Ω, respectively. The increase in R_{ct} value after deposition of MnO_2 nanoflowers is due to the poor electrical conductivity of MnO_2. The vertical shape in the low frequency region implying ideal electrochemical stability indicates better capacitance behavior for GrP and GrP/10-MnO_2 electrodes.

3.3.3 Flexible solid-state asymmetric supercapacitor device

For portable and flexible electronics, flexible solid-state supercapacitor (SASc) devices are highly desirable. Therefore, an asymmetric SASc device was assembled using GrP/10-MnO_2 and GrP as positive and negative electrode as illustrated in **Figure 3.8a** and **Figure 3.8b**. **Figure 3.8c** shows the CV curves for the SASc device at different potential windows up to 1.6 V with a scan rate of 5 $mV \cdot s^{-1}$. The results show that potential window of the SASc device is as large as 1.2 V without any appearance of polarized phenomenon. In **Figure 3.8d**, GCD curves are very symmetrical up to 1.0 V. Based on the analysis results of GCD and CV curves in **Figure 3.8c** and **Figure 3.8d**, the SASc device was further tested at the potential windows from 0 to 1.0V

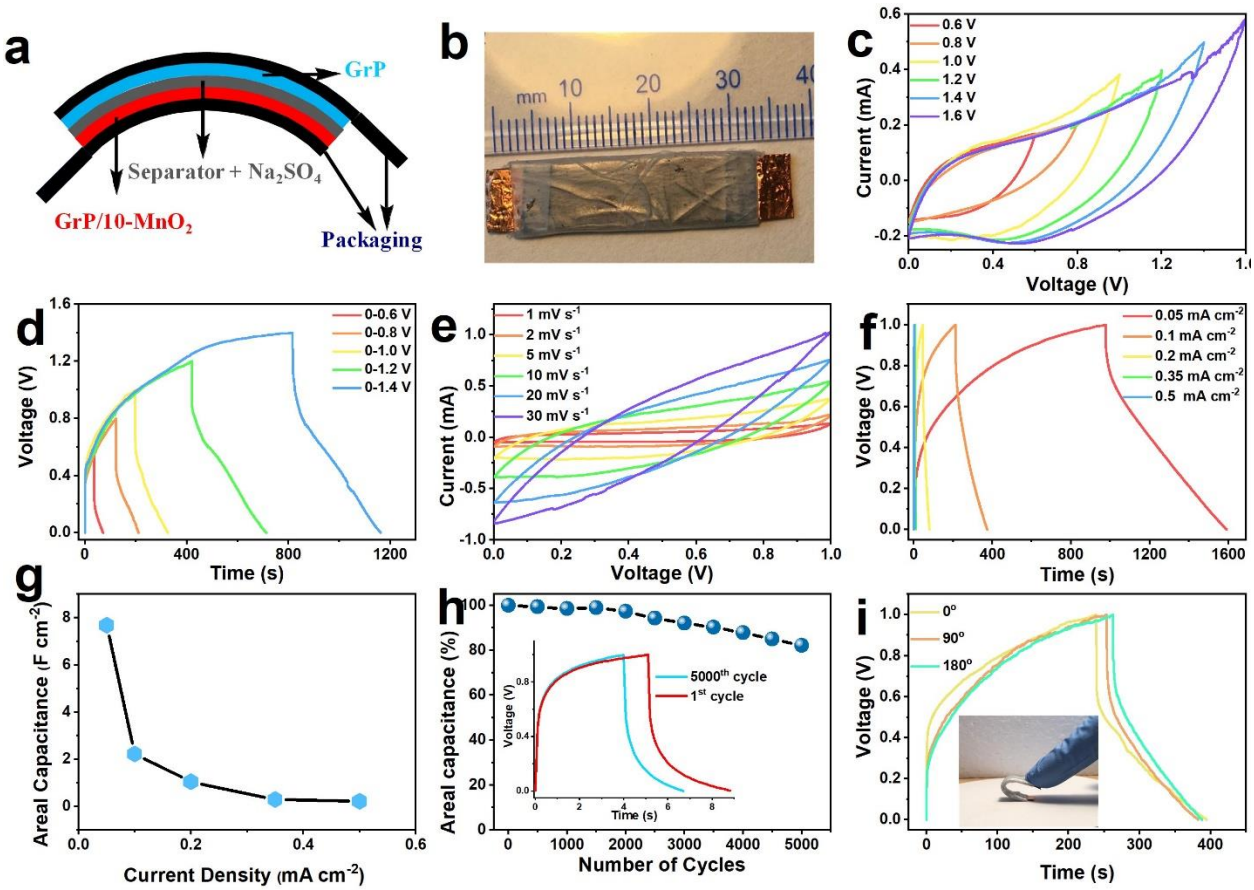

Figure 3.8 (a) Schematic diagram and **(b)** digital photographs of as-fabricated solid-state asymmetric supercapacitor (SASc) device. **(c)** CV curves of the fabricate SASc device at a scan rate of 5 $mV \cdot s^{-1}$. **(d)** GCD curves of SASc device at different potential windows at a current density of 0.10 mA cm^{-2}. **(e)** CV curves of SASc device at various scan rates with a potential window of 1 V. **(f)** GCD curves at various current densities and **(g)** their corresponding areal capacitance. **(h)** Cycle life of SASc device at a current density of 0.50 mA cm^{-2}. (i) GCD curves of SASc device under different bending angles (0˚, 90˚, 180˚) and the inset shows the digital photographs of flexible SASc at 180˚ bending angle.

with CV and GCD at different scan rate and current density, respectively. CV cycles of the flexible SASc device at various scan rates (1, 2, 5, 10, 20 and 30 mV s^{-1}) are presented in **Figure 3.8e** which shows rectangular like shape, implying a good rate capability of the SASc device and

the GCD curves at different current densities (0.05, 0.10, 0.20, 0.35 and 0.5 mA cm^{-2}) in **Figure 3.8f** show triangle-like shape, indicating the ideal capacitive characteristics of as-assembled device. The areal capacitance (C_A) of SASc are calculated based on GCD measurements in **Figure 3.8f**. C_A of flexible SASc device is calculated as [42]:

$$C_A = \frac{2It}{S\Delta V} \qquad (6)$$

Where I is the current (A), t is discharge time (s), S is the active area of a single electrode (cm^2), ΔV is the potential window (V). C_A values at various current densities are plotted in **Figure 3.8g** and the highest C_A is calculated as 76.8 mF cm^{-2} at a current density of 0.05 mA cm^{-2}.

The important parameters for SASC devices are the high energy density (E, W h·cm^{-2}) and power density (P, W·cm^{-2}). Therefore, the energy and power density of the as-assembled device is calculated as following equations (7) and (8).

$$E = \frac{1}{8}\, C_A\, (\Delta V)^2 \qquad (7)$$

$$P = \frac{E}{t} \qquad (8)$$

Where C_A is the areal capacitance (F cm^{-2}), t is the discharge time (h), ΔV is the potential window (V). The energy density of the flexible SASc device is 6.14 mWh·cm^{-2} at the power density of 36 mW·cm^{-2} which remains 50 mW·cm^{-2} at the energy density of 0.026 mWh·cm^{-2}.

High capacitance retention is an essential parameter for SASc devices. The long-term cycling performance of the as-fabricated SASc device was carried out with GCD measurements at 50 mA cm^{-2} for 5000 cycles as shown **Figure 3.8h**. The capacitance retention is about 82.2% after

Table 3.2 Comparing the capacitive characteristics of the MnO_2-carbon based electrodes for supercapacitor application

Sample[a]	**C_A ($mF \cdot cm^{-2}$)**	**Energy density**	**Power density**	**Capacitance retention**	**Ref.**
Symmetric MnO_2 nanostructure	56.3	5 $mWh \cdot cm^{-2}$	12 $mW \cdot cm^{-2}$	72.5% (1200 cycles)	[43]
Symmetric WSC	73.2	6.5 $\mu Wh \cdot cm^{-2}$	0.8 $mW \cdot cm^{-2}$	70% (5000 cycles)	[44]
CFASC	10.3	7.5 $\mu Wh \cdot cm^{-2}$	0.4 $mW \cdot cm^{-2}$	80% (10,000 cycles)	[45]
CNT/MnO_2//CNT	16.9	1.14 $\mu Wh \cdot cm^{-2}$	1.5 $mW \cdot cm^{-2}$	99% (10,000 cycles)	[46]
CF/MnO_2//CF/MoO_3	4.9	2.7 $\mu Wh \cdot cm^{-2}$	0.5 $mW \cdot cm^{-2}$	89% (3000 cycles)	[47]
MSC	0.26	19.5 $nWh \cdot cm^{-2}$	1.95 $\mu W \cdot cm^{-2}$	88% (3600 cycles)	[48]
ASC	55.8	64 $\mu Wh \cdot cm^{-2}$	1 $mW \cdot cm^{-2}$	95% (10,000 cycle)	[49]
GrP/10-MnO_2	76.8	6.14 $mWh \cdot cm^{-2}$	36 $mW \cdot cm^{-2}$	82.2 % (5000 cycles)	This work

a. symmetric WSC: Wire-type supercapacitor based on two wire-type MnO_2/multilayer graphene/Ni electrodes; CFASC: asymmetric supercapacitor composed of Fe_2O_3 with carbon fibers and MnO_2 with carbon nanotube web paper electrodes; CNT/MnO_2//CNT: asymmetric supercapacitor composed of MnO_2 carbon nanotube hybrid fiber and carbon nanotube fiber; CF/MnO_2//CF/MoO_3: asymmetric supercapacitor composed of carbon fiber with MnO_2 and carbon fiber with MoO_3; symmetric supercapacitor composed of δ-MnO_2 electrodes; ASC: asymmetric solid-state supercapacitor composed of reduced graphene with microwave treated carbon cloth and MnO_2 with microwave treated carbon cloth.

5000 consecutive GCD cycles. Compare to the results of reported graphene and MnO_2 based SASc devices in **Table 3.2**, as-assembled SASc device show high areal capacitance, excellent energy and power densities as well as comparable capacitance retention values [10, 11, 13, 31, 39, 40]. To demonstrate its practical application as a power source, two devices were connected in series as shown in **Figure A 3.12**. After charging for 15 seconds at 3.5 V, the devices powered a red LED.

For the portable and wearable energy storage devices, flexibility is of great interest. **Figure 3.8i** shows GCD measurements of the flexible SASc device at 10 mA cm^{-2} under the bending angles of 0˚, 90˚, and 180˚. The shape of curve and discharge time remained almost unchanged. The excellent flexibility of SASc device can be attributed to mechanically stable GrP and uniform deposition of MnO_2 nanoflowers onto GrP, which possess good mechanical properties.

3.4 Conclusions

In conclusion, we report a green, rapid, and cost-effective method to produce flexible, free-standing, and highly conductive supercapacitor electrodes made of GrP decorated with MnO_2 nanoflowers for enhanced charge storage. MnO_2 nanoflowers were electrochemically deposited on GrP. The amount of MnO_2 nanoflowers used was optimized by varying the number of electrodeposition cycles. The electrode material obtained after 10 cycles of MnO_2 deposition on GrP (GrP/10-MnO_2) exhibited superb capacitance performance with a high specific capacitance and outstanding stability after 5000 cycles. The assembled flexible SASc device showed not only an outstanding capacitance behavior but also an excellent long-term cycling performance. The specific power and energy density were as high as 6.14 mWh·cm^{-2} at current density of 0.05 mA cm^{-2} and 50 mW·cm^{-2} at current density of 0.5 mA cm^{-2}, respectively. The performance of this

flexible SASc device suggests the potential of GrP/10-MnO_2 composite in the field of flexible energy storage devices.

3.5 Appendix: Chapter III

Table A 3.1 Mass loading of MnO_2 for GrP/x-MnO_2 electrodes

Sample name	Mass of GrP (mg)	Mass of MnO_2 (mg)	Percent of MnO_2 in the electrode (%)
GrP	0.20	0	0
GrP/1-MnO_2	0.20	0.02	10
GrP/3-MnO_2	0.20	0.05	25
GrP/5-MnO_2	0.20	0.08	40
GrP/7-MnO_2	0.20	0.1	50
GrP/10-MnO_2	0.20	0.12	60
GrP/15-MnO_2	0.20	0.15	75
GrP/20-MnO_2	0.20	0.19	95

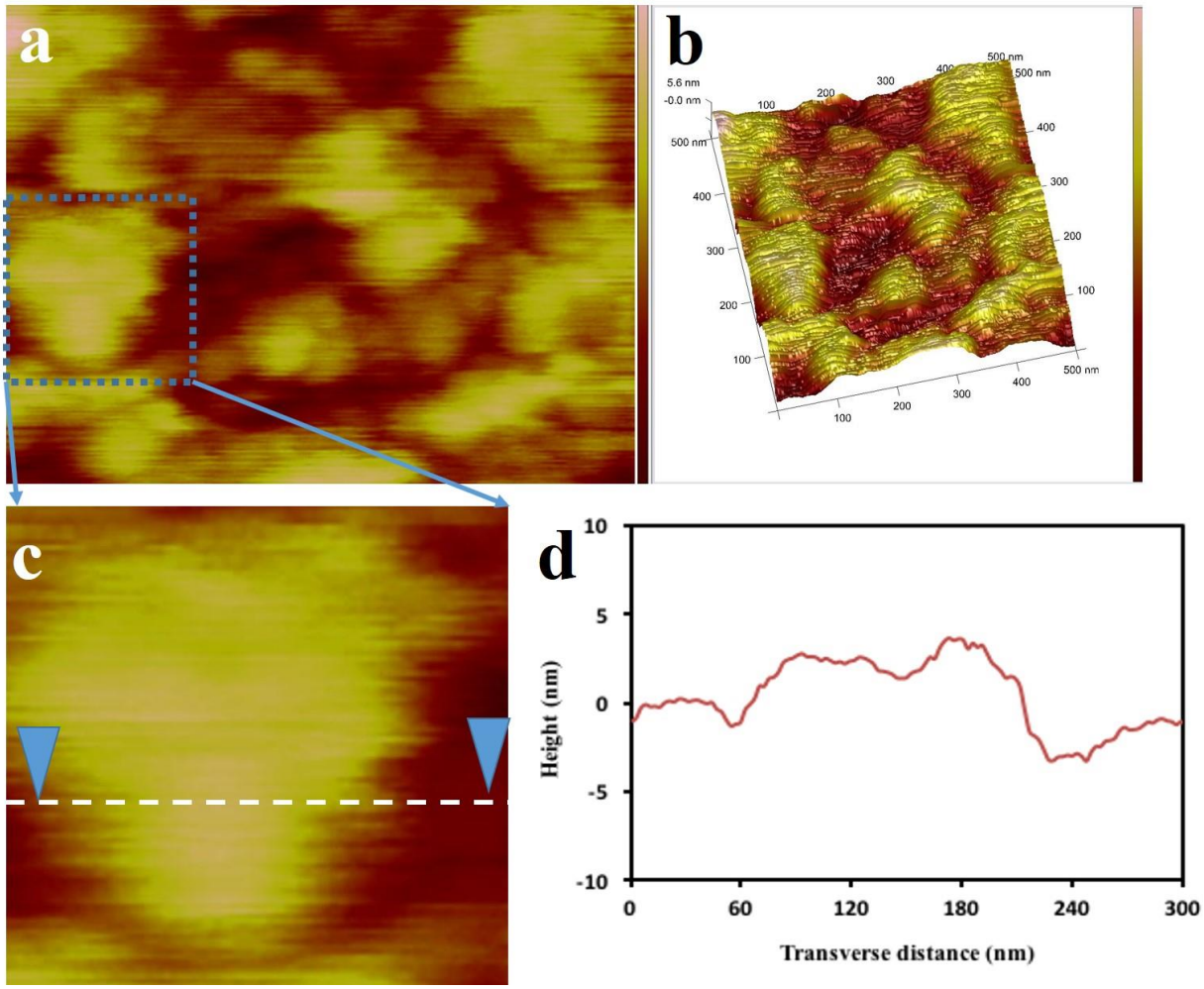

Figure A 3.6 (a) 2D and **(b)** 3D AFM images of exfoliated graphene. **(c)** enlarged view of a graphene sheet and **(d)** its height profile

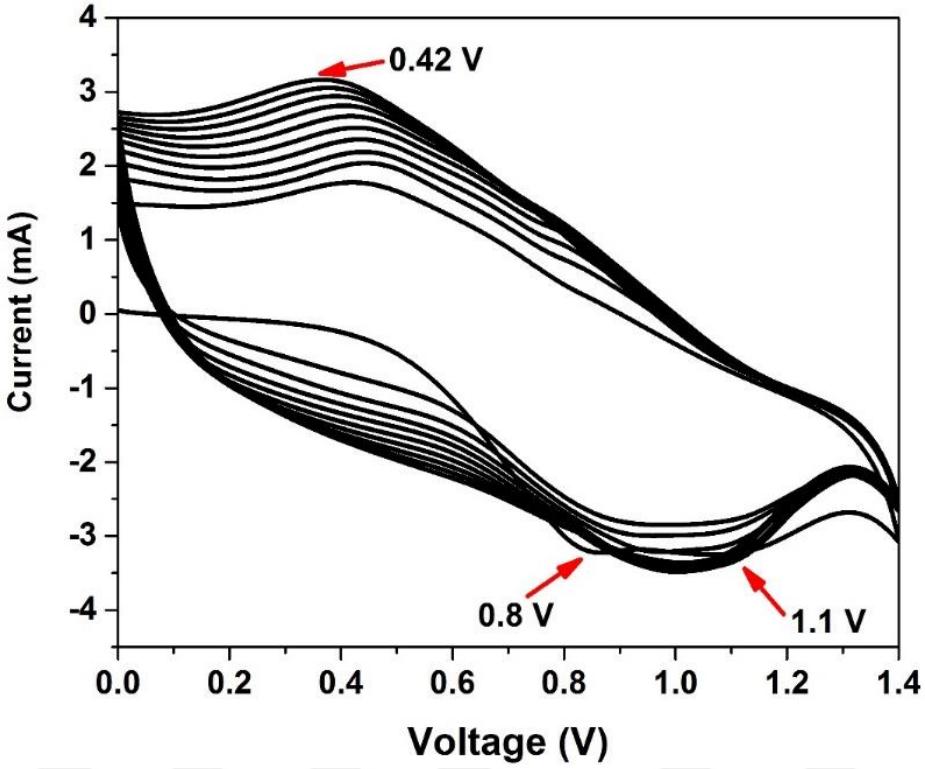

Figure A 3.7 Electrochemical deposition of MnO_2 on a GrP electrode in 50 mM $Mn(CH_3COO)_2$ and 100 mM Na_2SO_4 at scan rate of 50 $mV \cdot s^{-1}$.

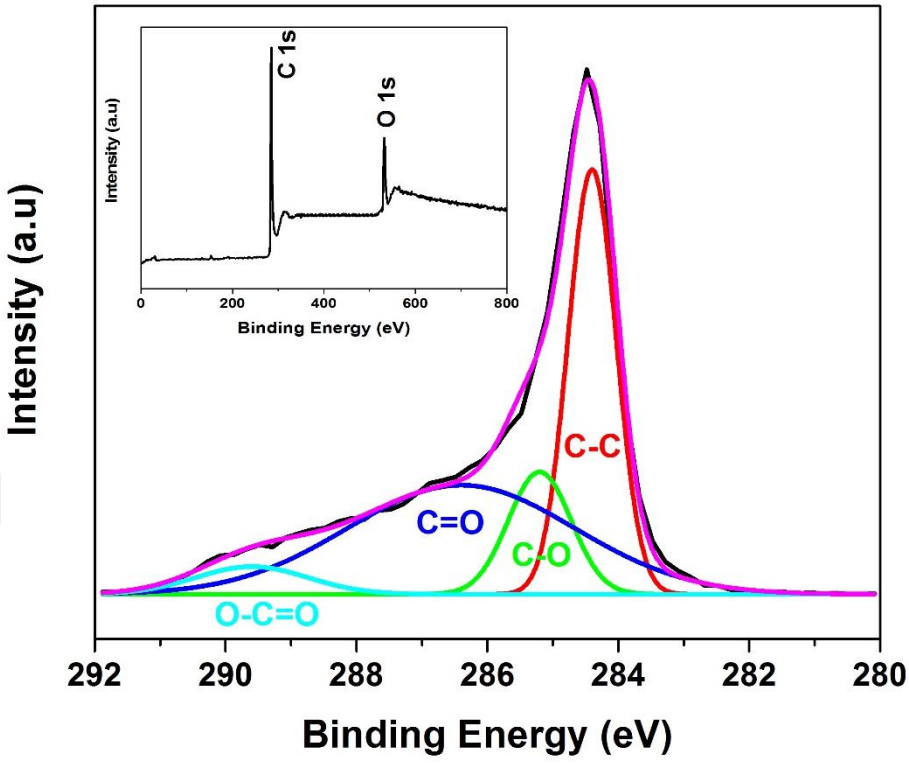

Figure A 3.8 XPS spectra of the C 1s spectra of the GrP. (inset: the wide spectrum)

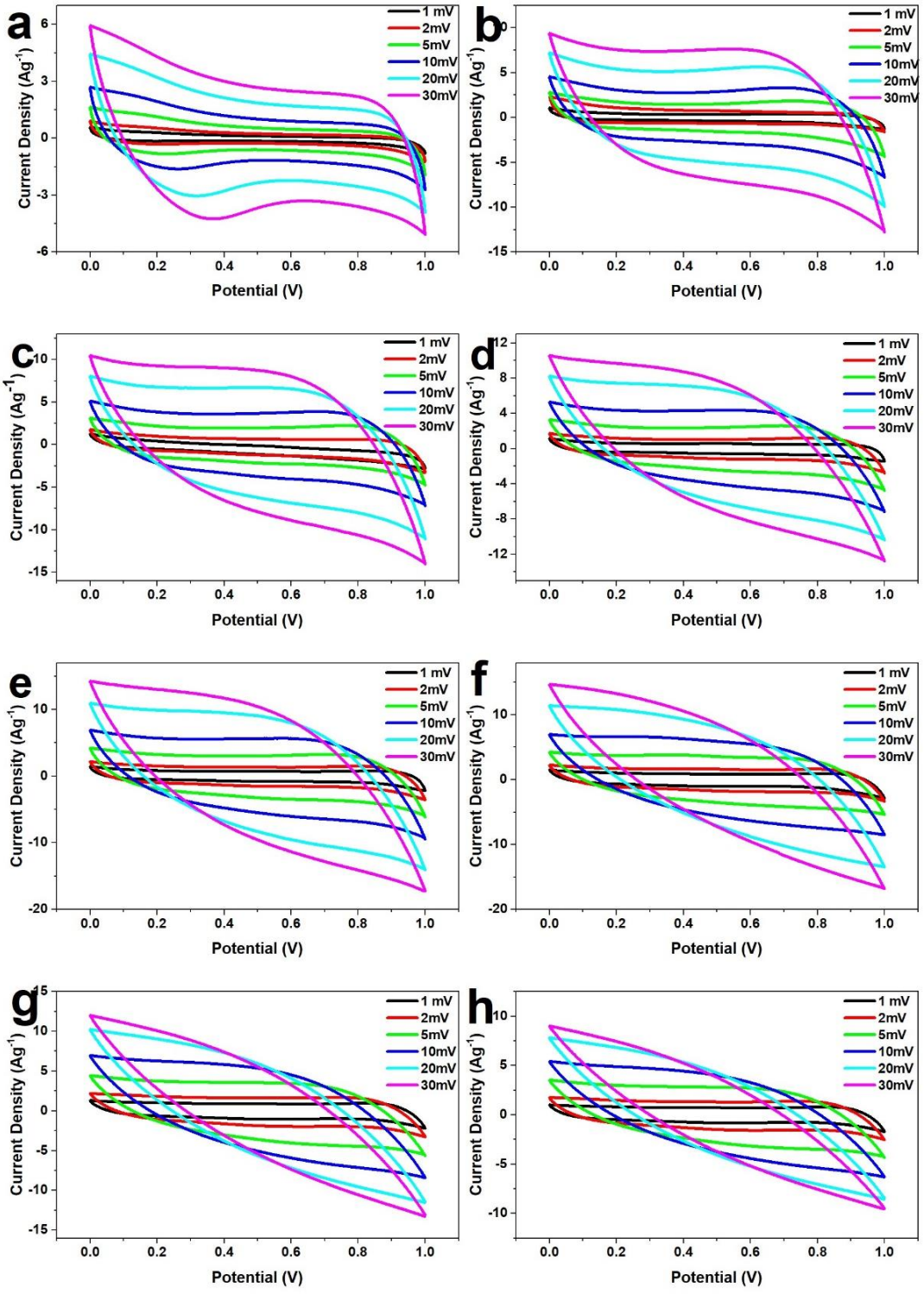

Figure A 3.9 Cyclic voltammetry of as-synthesized **(a)** GrP, **(b)** GrP/1-MnO_2, **(c)** GrP/3-MnO_2, **(d)** GrP/5-MnO_2, **(e)** GrP/7-MnO_2, **(f)** GrP/10-MnO_2, **(g)** GrP/15-MnO_2, and **(h)** GrP/20-MnO_2 electrodes

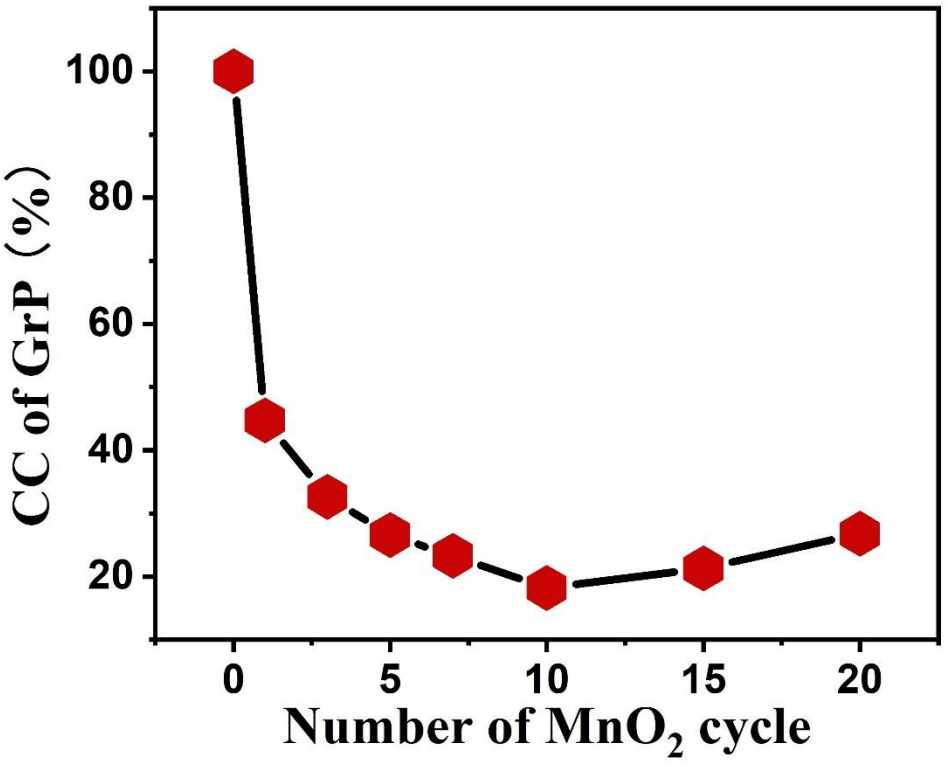

Figure A 3.10 Capacitance contribution (CC) of GrP in the GrP/x-MnO_2 electrodes.

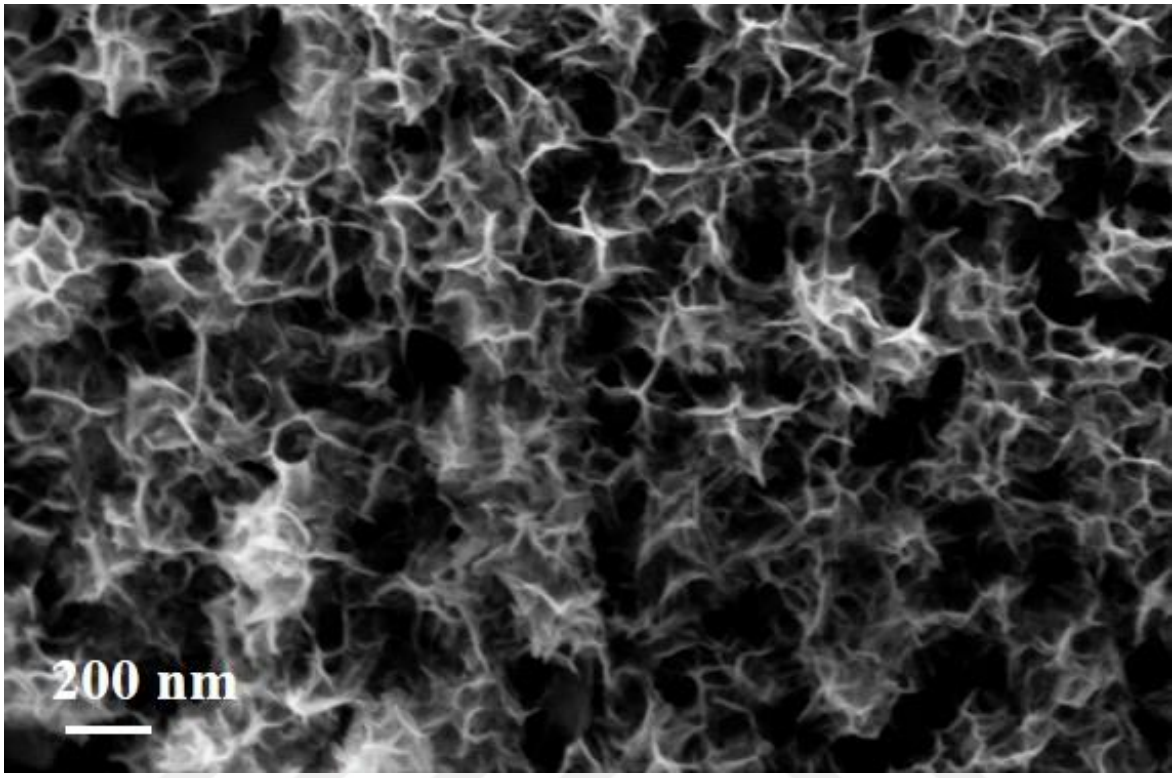

Figure A 3.11 SEM images of GrP/10-MnO_2 after over 5000 GCD cycles at a current density of 4 $A \cdot g^{-1}$.

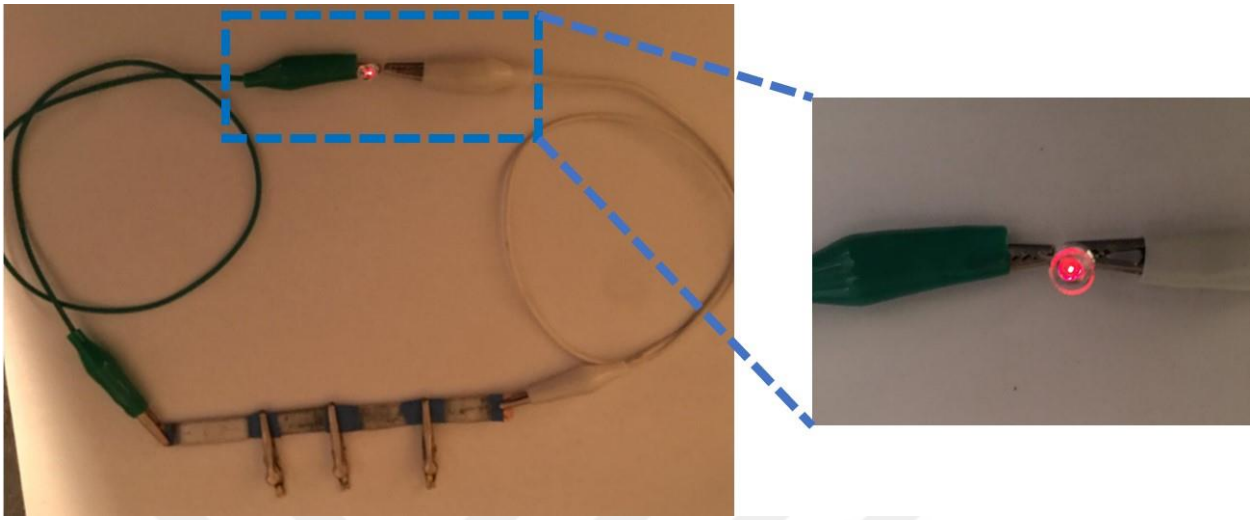

Figure A 3.12 Digital photograph of four SASc devices connected in series powering a red LED after charging for 15 seconds.

3.6 References

[1] L.L. Liu, Z.Q. Niu, L. Zhang, W.Y. Zhou, X.D. Chen, S.S. Xie, Nanostructured Graphene Composite Papers for Highly Flexible and Foldable Supercapacitors, Adv Mater 26(28) (2014) 4855-+.
[2] H.Y. Chen, S. Zeng, M.H. Chen, Y.Y. Zhang, L.X. Zheng, Q.W. Li, Oxygen Evolution Assisted Fabrication of Highly Loaded Carbon Nanotube/MnO2 Hybrid Films for High-Performance Flexible Pseudosupercapacitors, Small 12(15) (2016) 2035-2045.
[3] X. Yang, H. Niu, H. Jiang, Q. Wang, F.Y. Qu, A high energy density all-solid-state asymmetric supercapacitor based on MoS2/graphene nanosheets and MnO2/graphene hybrid electrodes, J Mater Chem A 4(29) (2016) 11264-11275.
[4] I. Hadjipaschalis, A. Poullikkas, V. Efthimiou, Overview of current and future energy storage technologies for electric power applications, Renew Sust Energ Rev 13(6-7) (2009) 1513-1522.
[5] W. Fan, Y. Shi, W. Gao, Z. Sun, T. Liu, Graphene–Carbon Nanotube Aerogel with a Scroll-Interconnected-Sheet Structure as an Advanced Framework for a High-Performance Asymmetric Supercapacitor Electrode, ACS Applied Nano Materials 1(9) (2018) 4435-4441.
[6] H.R. Naderi, P. Norouzi, M.R. Ganjali, Electrochemical study of a novel high performance supercapacitor based on MnO2/nitrogen-doped graphene nanocomposite, Appl Surf Sci 366 (2016) 552-560.
[7] W.F. Wei, X.W. Cui, W.X. Chen, D.G. Ivey, Manganese oxide-based materials as electrochemical supercapacitor electrodes, Chem Soc Rev 40(3) (2011) 1697-1721.
[8] M.U.A. Prathap, S.N. Sun, Z.J. Xu, An electrochemical sensor highly selective for lindane determination: a comparative study using three different alpha-MnO2 nanostructures, Rsc Adv 6(27) (2016) 22973-22979.
[9] G.Y. Zhu, Z. He, J. Chen, J. Zhao, X.M. Feng, Y.W. Ma, Q.L. Fan, L.H. Wang, W. Huang, Highly conductive three-dimensional MnO2-carbon nanotube-graphene-Ni hybrid foam as a binder-free supercapacitor electrode, Nanoscale 6(2) (2014) 1079-1085.
[10] Z.P. Li, Y.J. Mi, X.H. Liu, S. Liu, S.R. Yang, J.Q. Wang, Flexible graphene/MnO2 composite papers for supercapacitor electrodes, J Mater Chem 21(38) (2011) 14706-14711.
[11] Z.P. Li, J.Q. Wang, S. Liu, X.H. Liu, S.R. Yang, Synthesis of hydrothermally reduced graphene/MnO2 composites and their electrochemical properties as supercapacitors, J Power Sources 196(19) (2011) 8160-8165.
[12] X.H. Su, L. Yu, G. Cheng, H.H. Zhang, M. Sun, X.F. Zhang, High-performance alpha-MnO2 nanowire electrode for supercapacitors, Appl Energ 153 (2015) 94-100.
[13] J. Zhang, H.L. Zhang, Y.J. Cai, H.T. Zhang, Low-temperature microwave-assisted hydrothermal fabrication of RGO/MnO2-CNTs nanoarchitectures and their improved performance in supercapacitors, Rsc Adv 6(100) (2016) 98010-98017.
[14] A.C.H. Tsang, H.Y.H. Kwok, D.Y.C. Leung, The use of graphene based materials for fuel cell, photovoltaics, and supercapacitor electrode materials, Solid State Sci 67 (2017) A1-A14.
[15] R.K. Joshi, J.J. Schneider, Assembly of one dimensional inorganic nanostructures into functional 2D and 3D architectures. Synthesis, arrangement and functionality, Chem Soc Rev 41(15) (2012) 5285-5312.
[16] Q.Q. Ke, J. Wang, Graphene-based materials for supercapacitor electrodes - A review, J Materiomics 2(1) (2016) 37-54.
[17] W.W. Liu, J.D. Li, K. Feng, A. Sy, Y.S. Liu, L. Lim, G. Lui, R. Tjandra, L. Rasenthiram, G. Chiu, A.P. Yu, Advanced Li-Ion Hybrid Supercapacitors Based on 3D Graphene-Foam Composites, Acs Appl Mater Inter 8(39) (2016) 25941-25953.

[18] Y.L. Shao, M.F. El-Kady, C.W. Lin, G.Z. Zhu, K.L. Marsh, J.Y. Hwang, Q.H. Zhang, Y.G. Li, H.Z. Wang, R.B. Kaner, 3D Freeze-Casting of Cellular Graphene Films for Ultrahigh-Power-Density Supercapacitors, Adv Mater 28(31) (2016) 6719-+.
[19] S.M. Jung, D.L. Mafra, C.T. Lin, H.Y. Jung, J. Kong, Controlled porous structures of graphene aerogels and their effect on supercapacitor performance, Nanoscale 7(10) (2015) 4386-4393.
[20] V.H. Pham, J.H. Dickerson, Reduced Graphene Oxide Hydrogels Deposited in Nickel Foam for Supercapacitor Applications: Toward High Volumetric Capacitance, J Phys Chem C 120(10) (2016) 5353-5360.
[21] S. Lehtimaki, M. Suominen, P. Damlin, S. Tuukkanen, C. Kvarnstrom, D. Lupo, Preparation of Supercapacitors on Flexible Substrates with Electrodeposited PEDOT/Graphene Composites, Acs Appl Mater Inter 7(40) (2015) 22137-22147.
[22] Z.Y. Zhang, F. Xiao, L.H. Qian, J.W. Xiao, S. Wang, Y.Q. Liu, Facile Synthesis of 3D MnO2-Graphene and Carbon Nanotube-Graphene Composite Networks for High-Performance, Flexible, All-Solid-State Asymmetric Supercapacitors, Adv Energy Mater 4(10) (2014).
[23] D.W. Chang, J.B. Baek, Eco-friendly synthesis of graphene nanoplatelets, J Mater Chem A 4(40) (2016) 15281-15293.
[24] O. Sadak, A.K. Sundramoorthy, S. Gunasekaran, Facile and green synthesis of highly conducting graphene paper, Carbon 138 (2018) 108-117.
[25] G. Lee, W. Lee, S. Baik, Y.H. Kim, K. Eom, T. Kwon, Correlation between the hierarchical structures and nanomechanical properties of amyloid fibrils, Nanotechnology 29(29) (2018).
[26] L.Y. Niu, M.J. Li, X.M. Tao, Z. Xie, X.C. Zhou, A.P.A. Raju, R.J. Young, Z.J. Zheng, Salt-assisted direct exfoliation of graphite into high-quality, large-size, few-layer graphene sheets, Nanoscale 5(16) (2013) 7202-7208.
[27] C.J. Clarke, G.J. Browning, S.W. Donne, An RDE and RRDE study into the electrodeposition of manganese dioxide, Electrochim Acta 51(26) (2006) 5773-5784.
[28] M.F. Dupont, S.W. Donne, Nucleation and Growth of Electrodeposited Manganese Dioxide for Electrochemical Capacitors, Electrochim Acta 120 (2014) 219-225.
[29] A.K. Sundramoorthy, Y.C. Wang, S. Gunasekaran, Low-temperature solution process for preparing flexible transparent carbon nanotube film for use in flexible supercapacitors, Nano Res 8(10) (2015) 3430-3445.
[30] G.Q. Han, Y. Liu, E.J. Kan, J. Tang, L.L. Zhang, H.H. Wang, W.H. Tang, Sandwich-structured MnO2/polypyrrole/reduced graphene oxide hybrid composites for high-performance supercapacitors, Rsc Adv 4(20) (2014) 9898-9904.
[31] Z.B. Lei, F.H. Shi, L. Lu, Incorporation of MnO2-Coated Carbon Nanotubes between Graphene Sheets as Supercapacitor Electrode, Acs Appl Mater Inter 4(2) (2012) 1058-1064.
[32] G. Yasin, M. Arif, M. Shakeel, Y.C. Dun, Y. Zuo, W.Q. Khan, Y.M. Tang, A. Khan, M. Nadeem, Exploring the Nickel-Graphene Nanocomposite Coatings for Superior Corrosion Resistance: Manipulating the Effect of Deposition Current Density on its Morphology, Mechanical Properties, and Erosion-Corrosion Performance, Adv Eng Mater 20(7) (2018).
[33] B.T. Zhang, G. Cheng, B. Lan, X.Y. Zheng, M. Sun, F. Ye, L. Yu, X.L. Cheng, Crystallization design of MnO2 via acid towards better oxygen reduction activity, Crystengcomm 18(36) (2016) 6895-6902.
[34] J.H. Zhang, Y.B. Li, L. Wang, C.B. Zhang, H. He, Catalytic oxidation of formaldehyde over manganese oxides with different crystal structures, Catal Sci Technol 5(4) (2015) 2305-2313.
[35] S. Devaraj, N. Munichandraiah, Effect of crystallographic structure of MnO2 on its electrochemical capacitance properties, J Phys Chem C 112(11) (2008) 4406-4417.

[36] Y.S. Liu, W.Z. Li, J. Li, H.B. Shen, Y.M. Li, Y. Guo, Graphene aerogel-supported and graphene quantum dots-modified gamma-MnOOH nanotubes as a highly efficient electrocatalyst for oxygen reduction reaction, Rsc Adv 6(49) (2016) 43116-43126.
[37] S.M. Sun, S. Wang, T.C. Xia, X.F. Li, Q.X. Jin, Q. Wu, L.Z. Wang, Z.H. Wei, P.Y. Wang, Hydrothermal synthesis of a MnOOH/three-dimensional reduced graphene oxide composite and its electrochemical properties for supercapacitors, J Mater Chem A 3(42) (2015) 20944-20951.
[38] M.F. Dupont, S.W. Donne, Separating the Faradaic and Non-Faradaic Contributions to the Total Capacitance for Different Manganese Dioxide Phases, Journal of The Electrochemical Society 162(5) (2015) A5096-A5105.
[39] J. Yan, Z.J. Fan, T. Wei, W.Z. Qian, M.L. Zhang, F. Wei, Fast and reversible surface redox reaction of graphene-MnO2 composites as supercapacitor electrodes, Carbon 48(13) (2010) 3825-3833.
[40] J.T. Zhang, J.W. Jiang, X.S. Zhao, Synthesis and Capacitive Properties of Manganese Oxide Nanosheets Dispersed on Functionalized Graphene Sheets, J Phys Chem C 115(14) (2011) 6448-6454.
[41] J.M. Nugent, K.S.V. Santhanam, A. Rubio, P.M. Ajayan, Fast electron transfer kinetics on multiwalled carbon nanotube microbundle electrodes, Nano letters 1(2) (2001) 87-91.
[42] O. Sadak, M.U.A. Prathap, S. Gunasekaran, Facile fabrication of highly ordered polyaniline–exfoliated graphite composite for enhanced charge storage, Carbon 144 (2019) 756-763.
[43] X. Wang, B.D. Myers, J. Yan, G. Shekhawat, V. Dravid, P.S. Lee, Manganese oxide micro-supercapacitors with ultra-high areal capacitance, Nanoscale 5(10) (2013) 4119-4122.
[44] M. Hu, Y. Liu, M. Zhang, H. Wei, Y. Gao, Wire-type MnO2/Multilayer graphene/Ni electrode for high-performance supercapacitors, J Power Sources 335 (2016) 113-120.
[45] B. Patil, S. Ahn, S. Yu, H. Song, Y. Jeong, J.H. Kim, H. Ahn, Electrochemical performance of a coaxial fiber-shaped asymmetric supercapacitor based on nanostructured MnO2/CNT-web paper and Fe2O3/carbon fiber electrodes, Carbon 134 (2018) 366-375.
[46] P. Xu, B. Wei, Z. Cao, J. Zheng, K. Gong, F. Li, J. Yu, Q. Li, W. Lu, J.-H. Byun, Stretchable wire-shaped asymmetric supercapacitors based on pristine and MnO2 coated carbon nanotube fibers, ACS nano 9(6) (2015) 6088-6096.
[47] J. Noh, C.-M. Yoon, Y.K. Kim, J. Jang, High performance asymmetric supercapacitor twisted from carbon fiber/MnO2 and carbon fiber/MoO3, Carbon 116 (2017) 470-478.
[48] Y. Wang, Y.-Z. Zhang, D. Dubbink, E. Johan, Inkjet printing of δ-MnO2 nanosheets for flexible solid-state micro-supercapacitor, Nano energy 49 (2018) 481-488.
[49] H. Jeon, J.M. Jeong, S.B. Hong, M. Yang, J. Park, S.Y. Hwang, B.G. Choi, Facile and fast microwave-assisted fabrication of activated and porous carbon cloth composites with graphene and MnO2 for flexible asymmetric supercapacitors, Electrochim Acta 280 (2018) 9-16.

CHAPTER IV

4 Facile fabrication of highly ordered polyaniline–exfoliated graphite composite for enhanced charge storage *

4.1 Introduction

Supercapacitors are popularly used in small and portable devices, especially in those that require safe and reliable power supply and rapid charge/discharge cycles. Compared to batteries, supercapacitors afford advantages such as high power density, long cycle life, low maintenance cost, and high temperature resilience (down to -40 °C) [1-3]. However, supercapacitors suffer from lower energy density (usually ≤10 Wh kg^{-1}) [4]. To overcome this problem asymmetric (hybrid) structures are used, which result in higher energy density [5, 6].

Based on the charge storage mechanism, supercapacitors are classified as either electric double layer capacitors (EDLCs) or pseudocapacitors [7]. The capacitance of EDLCs is attributed to charge adsorption at the electrode interface of active carbon substances, while that of pseudocapacitors is based on transition metal oxides or conducting polymers [8-10]. EDLCs are stable but of low capacitance, around 100 to 200 F g^{-1} [7, 11]; whereas, pseudocapacitors offer higher capacitance due to rapid and reversible redox or faradic transformation both at the surface and within the bulk [12, 13]. Consequently, much research has been focused on combining the advantages of the EDLCs and pseudocapacitors [14]. The primary problem in using conductive polymers as supercapacitor electrode is that they undergo poor tolerance during non-stop charge/discharge cycling [14, 15].

For capacitors, the width of potential window is important, because energy storage is proportional to the applied voltage. Several researchers have attempted to extend the potential window [14, 15].

* As published in Carbon 2019, 144, 756-763.

Shen et al. reported an operating voltage window of up to 2.0 V for an asymmetric supercapacitor combining carbon materials with conductive polymers [16]. However, for electrical storage applications 3.0 V supercapacitor cells are needed to meet the higher energy requirements [16].

Among conducting polymers, polyaniline (PANI) possesses unique electrical and electronic properties, good redox reversibility, and environmental stability; PANI nanostructures additionally have superior capacitive properties [17, 18]. Therefore, to enhance the performance of electrochemical supercapacitors, carbon materials are modified with PANI, for example PANI/carbon nanotubes, PANI/mesoporous carbon, and PANI/graphite nanosheets etc. [19-22]. PANI also can act as a spacer between graphene layers, preventing them from restacking [22, 23].

The supercapacitor performance of graphene oxide (GO)-doped PANI composite was limited by the low electrical conductivity and the less-active surface area of GO [24, 25]. On the other hand, the use of PANI-graphene composite has enhanced the overall capacitive performance [9, 26]. Fan et al. prepared PANI intercalated into sulfonated graphene paper via vacuum filtration, which exhibited specific capacitance of 478 F g^{-1} at a discharge rate of 0.5 A g^{-1} [27]. The charge storage residences similarly improved when the benefits of freestanding graphene paper and PANI nanorod arrays were combined [27]. Gao et al. reported a capacitance of 442 F g^{-1} at 1 A g^{-1} for p-phenylenediamine functionalized graphene covalently grafted on PANI nanofibers [28]. A three-dimensional PANI-graphene hybrid foam electrode was also reported to have a capacitance of 346 F g^{-1} at 4 A g^{-1} [29]. Hence, PANI-graphene hybrids are excellent materials for supercapacitors. Therefore, there is still a need for an easy and rapid method to produce highly ordered structural PANI–graphene hybrids with excellent electrochemical performance on a large-scale. Herein, we report a scalable and effective strategy to synthesize exfoliated graphite-PANI (EG-PANI) hybrid

material via interfacial polymerization method at room temperature. Furthermore, a solid-state asymmetrical supercapacitor (SASc) device using EG-PANI was fabricated. The assembled device exhibited high specific areal capacitance of 80.4±2.3 mF cm^{-2} at current density of 1 mA cm^{-2}, energy density of 9.07 μW h cm^{-2} at current density of 1 mA cm^{-2}, and specific power of 4.14 mW cm^{-2} at current density of 5 mA cm^{-2}, with an excellent capacitance retention of 90.2 % after 1000 galvanostatic charge–discharge cycles. We also fabricated EG-PANI based SASc and demonstrated its potential for energy storage application by powering LEDs.

4.2 Experimental section

4.2.1 Preparation of exfoliated graphite (EG)

EG was prepared following our published method with some modifications [30]. Briefly, in a two-electrode electrolysis cell, highly pure graphite sheets (40 mm × 15 mm × 2 mm) (Graphitestore, Northbrook, IL) were used both as anode and as cathode. Both electrodes were immersed in aqueous solution of 0.1 M phosphate buffered saline (PBS) (pH 7). A positive voltage (3.0 V DC, Tektronix PS280 power supply) was applied to the anode for 30 min, which caused exfoliation of graphite at the edges. The exfoliated graphite flakes were collected, washed with deionized (DI) water, and vacuum-filtered using cellulose paper (pore size = 0.45 μm). The washed flakes were sonicated in DI water for 60 min and the supernatant of concentration 2.5 mg mL-1 was collected as EG and stored for further use.

4.2.2 Preparation of EG-PANI composite and PANI

EG-PANI was synthesized through a modified interfacial polymerization method [31]. In a typical synthesis, 200 mg of aniline was dissolved in 20 mL $CHCl_3$ and used as the organic phase. Then ammonium peroxydisulfate (APS, 50 mM) was dissolved in 10 mL of 1 M dopant acid (HCl)

solution and 5 mL of aqueous EG (2.5 mg mL^{-1}) were used as the aqueous phase. When these two solutions were transferred to a glass vial, an interface between the organic and aqueous phases was generated. After 20 h at room temperature, a dark green layer was formed at the interface, which was filtered, rinsed with DI water and ethanol several times to remove excess acid, and finally dried at 70 °C for 8 h. For comparison, PANI was also prepared without adding 5 mL of aqueous EG (2.5 mg mL^{-1}) to the aqueous phase.

4.2.3 Electrode fabrication and characterization

Glassy carbon electrode (GCE), polished with alumina powder (0.05 µm) and ultrasonicated in ethanol and DI water for 5 min, was used as the working electrode. A suspension of EG-PANI was prepared by mixing 5 mg of EG-PANI solution with a mixture of 0.1 mL of Nafion® (0.5 wt%) and 0.9 mL of water and sonicating for one hour. The GCE was modified with EG-PANI by placing 5 µL aliquot of the EG-PANI suspension on the surface and allowing it to air dry at room temperature. For comparison, GCE was modified separately with EG and PANI alone following the same procedure.

A three-electrode electrochemical cell was employed with Ag/AgCl (3 M KCl) as reference electrode, EG-PANI/GCE, EG/GCE or PANI/GCE as working electrodes, a platinum foil as counter electrode and aqueous H_2SO_4 solution (1 M) as electrolyte. The prepared working electrodes were electrochemically characterized via cyclic voltammetry (CV), electrochemical impedance spectroscopy (EIS), and galvanostatic charge–discharge (GCD) experiments. Nyquist diagrams for EG-PANI/GCE were recorded in the frequency range of 0.1 Hz to 10 kHz at an open circuit potential, using a sinusoidal potential perturbation with an amplitude of 5 mV. The EIS plots were analyzed using an equivalent circuit model with Z-view software.

4.2.4 Solid-state asymmetrical supercapacitor device fabrication

The EG-PANI suspension (20 mg) was applied on a graphite sheet (5 cm x 1.2 cm) and dried in a vacuum oven at room temperature for 12 h to fabricate positive electrode. EG was used as a negative electrode. PVA-H_2SO_4 gel electrolyte was prepared by adding 1 mL H_2SO_4 (98 wt%) in 10 mL DI water, followed by 1 g PVA powder; the resulting solution was heated to 85 °C under stirring for 10 h and then allowed to cool to room temperature [32]. To fabricate a SASc device, a filter paper soaked in PVA–H_2SO_4 gel electrolyte used as a spacer sandwiched between the positive and negative electrodes.

4.2.5 Material characterizations

EG-PANI was characterized via various techniques. These include, X-ray diffraction (XRD) (PANalytical X'PERT PRO, using CuK-alpha radiation, λ=0.1542 nm, 40 kV, 20 mA), for phase identification; X-ray photoelectron spectroscopy (XPS), for surface chemical composition and elemental distribution (Thermo Scientific K Alpha instrument); Fourier transform infrared spectroscopy (FTIR, Bruker TENSOR-27), for chemical bonds, and thermogravimetry (TGA Q50, TA) and differential scanning calorimetry (DSC Q20, TA), for thermal properties. Scanning electron microscopy (FESEM, LEO 1530-1) and transmission electron microscopy (TEM, Tecnai T-12) were used to examine the morphological characteristics. Electrochemical experiments were performed using CHI-660D electrochemical workstation (CHI Instruments Inc., USA).

4.3 Results and discussion

4.3.1 EG-PANI formation and characterization

The EG-PANI nanocomposite was prepared via a one-pot interfacial polymerization technique as illustrated in **Figure 4.1**. First, EG was prepared by electrochemical exfoliation using graphite sheets as both anode and cathode and PBS as electrolyte solution. For the interfacial polymerization, aniline monomer was dissolved in an organic phase and EG solutions were prepared in aqueous phase with oxidizing agent. When these two solutions are mixed, aniline monomers are adsorbed onto the EG sheets as nucleation sites in a short time [33]. Though various approaches have been suggested for the preparation of PANI–graphene hybrids, many on the methods are rather unsuitable for large-scale preparation with well-controlled materials properties required for use in supercapacitors. In fact, there are two barriers to the fabrication of well-controlled PANI–graphene hybrids. First, graphene has strong tendency to form immiscible aggregates in solution. Second, the development of high-grade graphene is an intricate and costly procedure. We overcame these by selecting graphite instead of graphene. Expanded graphite (EG) to enhance dispersion and initiate the growth of PANI [34, 35]. As a graphitic material, EG has drawn increasing interest from researchers. EG can be chemically functionalized with epoxides and hydroxyls, which stabilize the sheets in water.

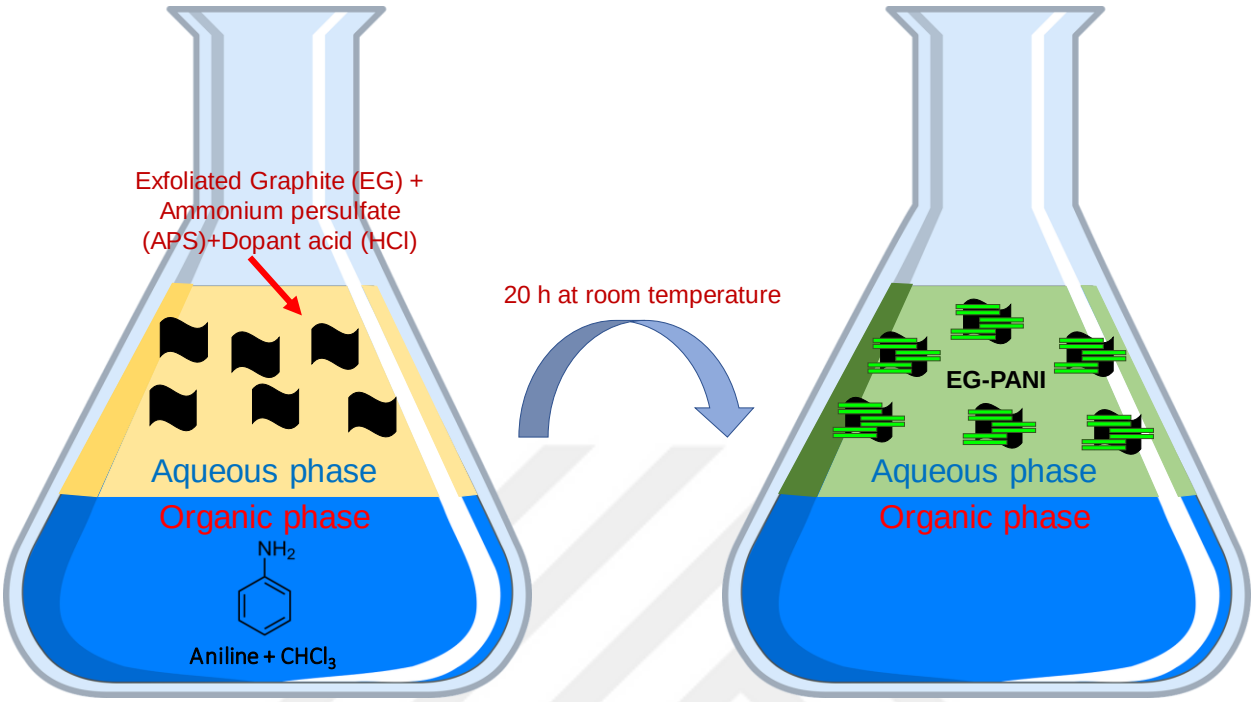

Figure 4.1 Schematic illustration of the formation process of EG-PANI hybrids via interfacial polymerization in a chloroform-water system

The phase formation of synthesized nanomaterials was examined from the XRD scans (**Figure 4.2a**). The characteristic peaks of PANI at 2θ=19.2° and 25.5° are attributed to the perpendicular (110) and parallel (100) periodicity of the polymer chain, respectively [36, 37] and the peak at 2θ=6.4° indicates its good crystallinity. The XRD pattern of EG shows a strong diffraction at 26.8° due to the graphite phase from (022) reflection. After introducing PANI, we observed broadening of the peak due the amorphous nature of EG-PANI composite, which indicates intercalation of PANI into EG nanosheets [38]. The sharp diffraction peak of EG completely disappeared in EG-PANI, which can be attributed to PANI particles dispersed around EG sheets.

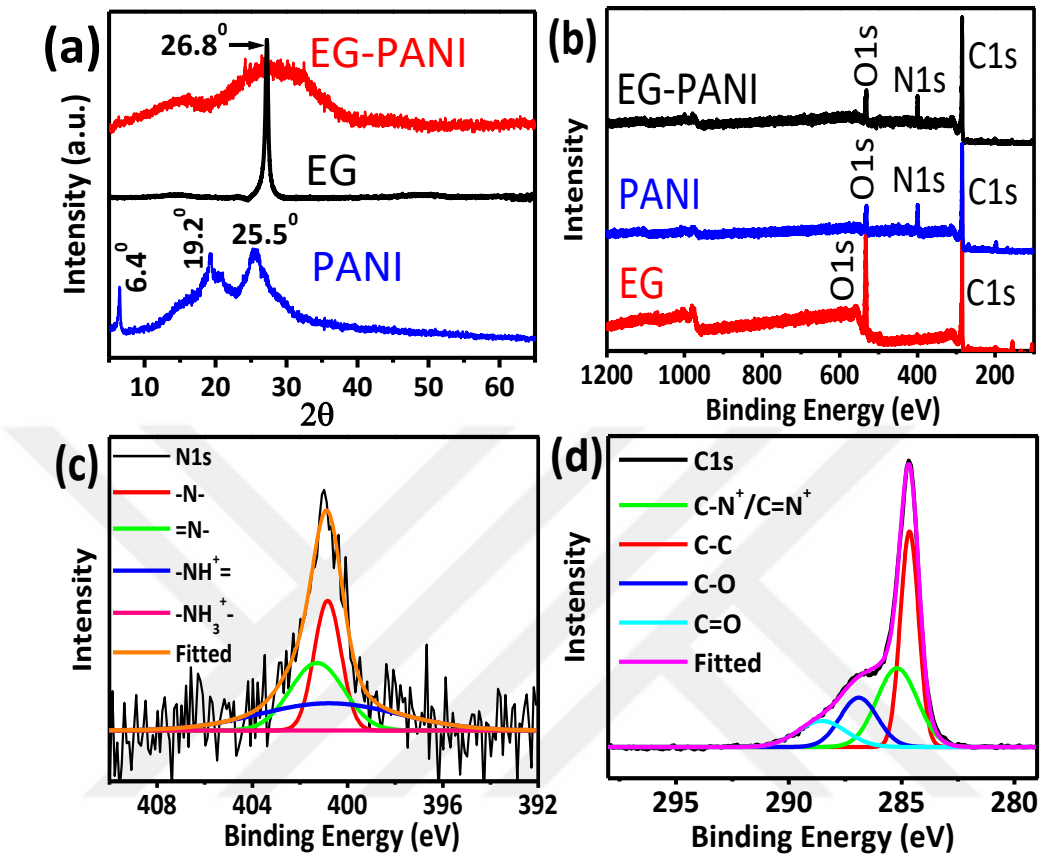

Figure 4.2 (a) XRD spectra of PANI, EG and EG-PANI (b) Wide range XPS spectra of PANI, EG and EG-PANI (c) the N1s region of EG-PANI (d) the C1s region of EG-PANI.

The chemical composition and bonding of the as-prepared materials were analyzed from their wide range XPS spectra (**Figure 4.2b**). The deconvolution of N1s peak in EG-PANI spectrum shows successful polymerization of PANI on EG sheets. The high-resolution N1s spectra of EG-PANI (**Figure 4.2c**) exhibits four peaks at 389.4, 399.9, 400.2, and 401.9 eV, which are attributed to -N=, -NH- $=NH^+=$ and $-NH_2^+-$, respectively [7]. The protonated peaks are indicative of high N-doping level (37%) of PANI in EG-PANI [39]. The high-resolution spectra of C1s (**Figure 4.2d**) show peaks at 284.6 285.2, 286.8 and 288.5 eV, attributed to C-C, $C-N^+/C=N^+$, C-O and C=O, respectively.[40] The $C-N^+/C=N^+$ peak further confirms the presence of PANI in EG-PANI.

SEM micrograph of EG exhibits a 2- to 4-μm long wrinkled sheet-like structure (**Figure 4.3a and inset**). In the HRTEM image graphite is seen expanded revealing the edges of individual sheets. The micrographs of PANI show uniform ~95 nm wide fibrous structures (**Figure 4.3b and inset**), and the micrograph EG-PANI shows that PANI nanoparticles are homogeneously and densely attached on the surface of EG sheets (**Figure *4.3*c**). The HRTEM observation confirms the intimate contact between the graphite sheets and PANI nanoparticles (**Figure 4.3d**). Since the direct redox reaction between graphene and aniline has been reported, we predict that aniline is adsorbed on the surface of EG to form aniline-modified EG via strong π–π stacking [1]. Moreover, EG retains its sheet-like structure and is surrounded by PANI nanoparticles.

The thermal stability of EG, PANI, and EG-PANI were studied by TGA at a heating rate of 10 °C min^{-1}. The TGA curves of all the materials (**Figure A 4.1**) show a mass loss during the initial heating stage (around 100 °C) due to deintercalation of water. The EG and EG-PANI show a mass loss from 150 °C to 200 °C due to defunctionalization of graphite sheets. PANI and EG-PANI begin with a rapid decomposition at around 150 °C and 190 °C, respectively until 300 °C and the mass loss was attributed to the decomposition of oxygen-containing groups. After 300 °C the mass loss was ascribed to decomposition of the PANI component in the nanocomposite [11]. The larger mass loss of EG-PANI compared to that of EG is attributed to the decomposition of PANI.

The thermal stability of EG-PANI was further investigated by differential scanning calorimetry (DSC) with heating and cooling cycles in the range of 25 °C to 400 °C (**Figure A 4.2**). An endothermic peak observed at 100 °C in the heating cycle is attributed to the loss of entrapped water, which agrees with the TGA results. An exothermic peak at 177 °C can be ascribed to defunctionalization of graphite sheets as well as decomposition of PANI [13, 41]. There is

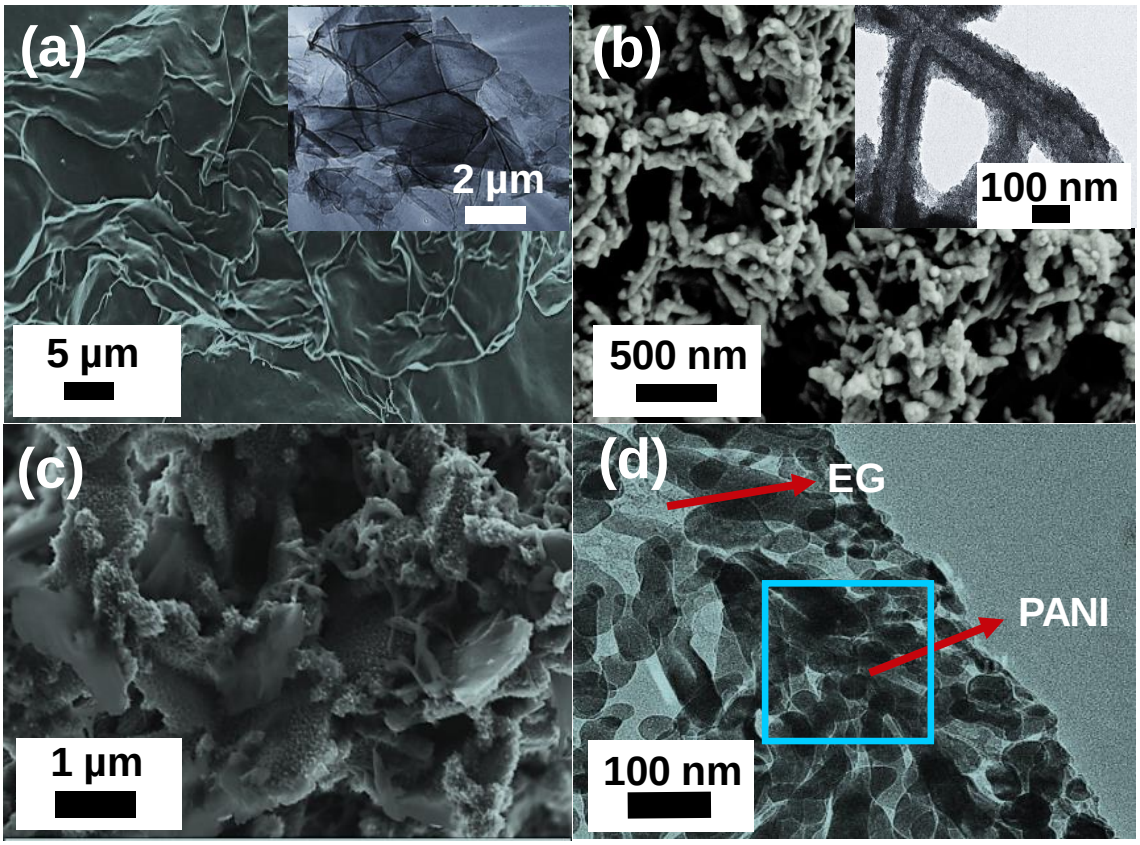

Figure 4.3 SEM images of (a) EG (inset HRTEM), (b) PANI (inset HRTEM) and (c) EG-PANI and (d) HRTEM image of EG-PANI.

evidence that a crosslinking reaction occurs between EG and PANI (emeraldine salt); thus, an increase in activation energy is required to break this interaction at the interphase [13, 42].

The absence of those peaks in the cooling cycle confirms that they are irreversible, indicating decomposition of PANI and evaporation of water.

The chemical structures of EG, PANI, and EG-PANI are characterized from their FTIR spectra (**Figure A 4.3**). In the EG spectrum characteristic bands appear for OH stretching (3432 cm^{-1}), C=O stretching (1730 cm^{-1}), C=C stretching (1642 cm^{-1}), and C-O stretching (1107-1217 cm^{-1})

[43]. The EG-PANI spectrum displays several new distinctive peaks compared to that of EG indicating successful incorporation of PANI on the surface of EG. The peaks at 1572, 1493, 1300, and 802 cm^{-1} are ascribed to the vibration of C═N, C═C, C−N, and C−H in quinoid and benzenoid rings, respectively [37, 38].

4.3.2 Electrochemical performance of EG-PANI supercapacitor

The potential of using EG-PANI for supercapacitor application was evaluated by CV, GCD and EIS techniques using a three-electrode system. The CV measurements were performed within a potential window of 0 to 0.8 V vs. Ag/AgCl in 1 M H_2SO_4 solution (**Figure 4.4a**). The CV curve of EG appears rectangle-like, whereas those of PANI and EG-PANI show two pairs of reversible redox peaks, which can be assigned to the redox transformation among leucoemeraldine-based states and emeraldine salt, and the transition among emeraldine salt and pernigraniline and their reversible transitions, respectively [31]. The area surrounded by the CV curve of EG-PANI is much larger than those of EG and PANI curves, implying higher specific capacitance of EG-PANI. The presence of PANI in the composite is the reason for the larger redox peaks observed in the EG-PANI curve.

The CV curves of EG-PANI at different scan rates from 1 to 100 mV s^{-1} are shown in **Figure 4.4b**; the quasi-rectangular shape of these curves can be attributed to the combination of EDLC and pseudocapacitance properties of EG and PANI [22]. While the peak current increased with the scan rate, the overall shape of the CV curves remained the same, which shows good reversible redox capacity and good rate capability of EG-PANI.

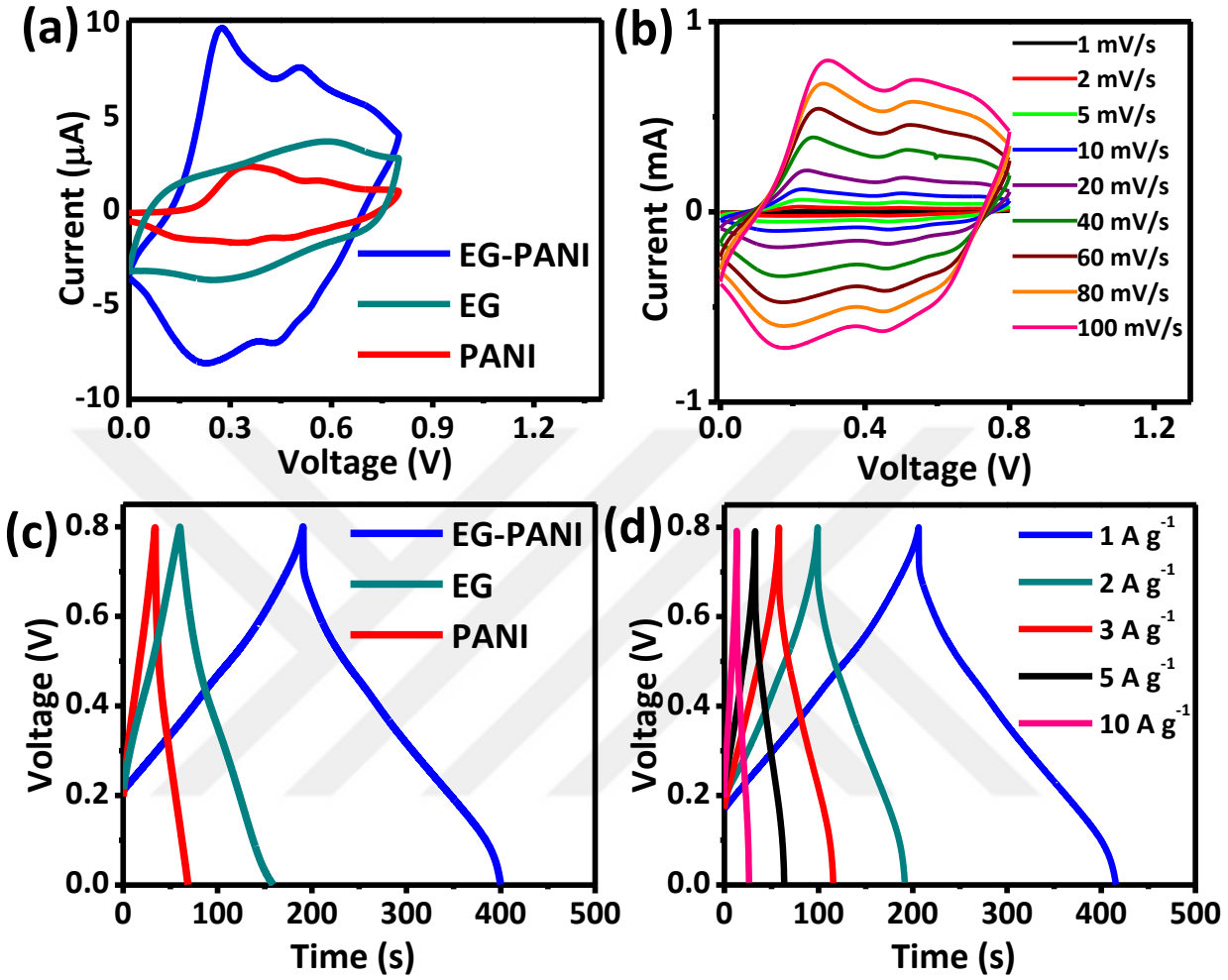

Figure 4.4 (a) CV curves of PANI, EG and EG-PANI at 1 mV s^{-1} scan rate. (b) CV curves of EG-PANI at different scan rates. (c) GCD curves for PANI, EG and EG-PANI at 1 A g^{-1} current density. (d) GCD curves of EG-PANI at different current densities.

The GCD curves of EG, PANI and EG-PANI electrodes obtained at constant current density of 1 A g^{-1} over the potential window of 0-0.8 V are presented in **Figure 4.4c**. The GCD duration for the EG-PANI is much larger than those for EG and PANI, which confirms good capacitance behavior of EG-PANI. The GCD curves of EG-PANI at current densities of 1 to 10 A g^{-1} are rather

triangular in shape (**Figure 4.4d**), implying the presence of EDLC and pseudocapacitance at the EG-PANI and electrolyte interface, which substantiates our CV results.

The electrochemical performance of EG-PANI was further analyzed via EIS in the 0.1 Hz to 10 kHz frequency range at open circuit potential with a potential amplitude of 5 mV to understand its capacitance behavior. EIS provides more information on the redox reaction resistances and equivalent series resistance of the electrode. The Nyquist plots of EG, PANI, and EG-PANI (**Figure A 4.4**) show sloped straight lines over the low-frequency region and negligible semicircle response at the high-frequency region. The line for EG-PANI composite is an effect of combined capacitance contribution from EG and PANI, implying better capacitive behavior as well as lower ion diffusion resistance than PANI; note that a vertical line with 90° phase angle represents an ideal capacitor. The Nyquist plot for EG is much steeper than for EG-PANI. This might be illuminated by the distinct morphology of this composite. Amount of PANI in EG-PANI composite are distributed homogeneously on the surface of layered graphene sheets. Thus, the ions of electrolyte do not penetrate into the particulate and access only the surface of PANI nanofibers. Suggesting that interfacial charge-transfer resistance among EG-PANI is significantly low. However, it was found that the EG and the PANI formed a uniform nanocomposite in our method with the PANI nanoparticles absorbed on the surface and/or filled between the EG sheets. When made use of as supercapacitor electrodes, such consistent framework observed high conductivities, high specific capacitance and good cycling stability during the charge-discharge process when used as supercapacitor electrodes, which can be confirmed from CV and GCD curves (**Figure 4.4a, c**) [44, 45]. The absence of the semicircle in the high frequency region is attributed to excessive ionic conductivity at the electrode/electrolyte interface. The solution resistance (R_s) values obtained from the x-intercept are fairly close for EG, PANI and EG-PANI electrodes (6.0,

3.3 and 5.8 Ω, respectively). The Nyquist plot of EG-PANI can be modelled by an equivalent circuit shown in Fig. S4 inset, where R_{ct}, W, and C_{sp} are charge-transfer (or Faraday) resistance, Warburg impedance, and pseudocapacitance, respectively.

4.3.3 Solid-state asymmetric supercapacitor device

The CV measurements of SASc device (**Figure 4.5a, b**) at various potential windows at fixed scan rate of 200 mVs^{-1} are presented in **Figure 4.5c**. The SASc exhibits an ideal capacitive behavior with rectangular-like shape even at a potential window up to 2.0 V. This large potential window of operation indicates a high-power density. The retention of rectangle-like shape of the CV curves at various scan rates (**Figure 4.5d**) indicates a good rate capability of the as-assembled device.

The specific capacitance and rate capability of the SASc at various current densities are also revealed by GCD measurements (**Figure 4.5e**). Therefore, the areal specific capacitance (C_A) of the as-assembled device is calculated as:

$$C_A = \frac{2It}{S\Delta V} \quad (1)$$

where I is the applied constant current (A), t is the discharge time (s), S is area of single electrode (cm^2), and ΔV is the potential window (V). The C_A values at different current densities are shown in **Figure 4.5g**. The C_A of SASc at 1 mA cm^{-2} is as high as 80.4±2.3 mF cm^{-2}, which is comparable with that of other graphene and PANI-based devices, including porous graphene/PANI composites

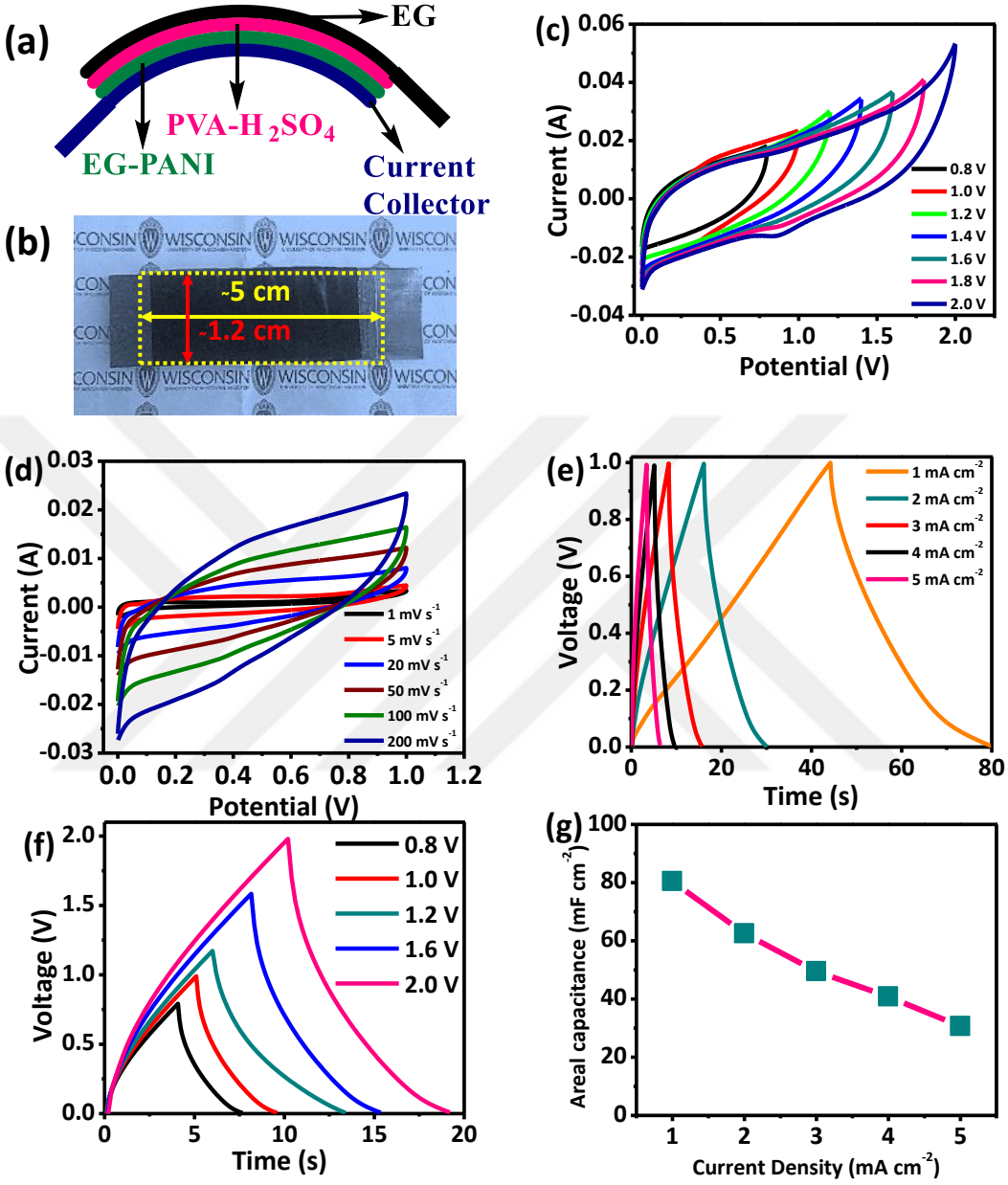

Figure 4.5 (a) Illustration of fabricated solid-state asymmetric supercapacitor (SASc), (b) its dimensions. (c) The CV curves at different potential windows at a scan rate of 200 mV s^{-1} (d) the CV curves at different scan rates within a potential window of 0 to 1.0 V. (e) GCD curves at different current densities and (f) GCD curves at different potential windows at the current density of 5 mA cm^{-2}. (g) Areal specific capacitance as a function of current density.

(67.2 mF cm^{-2} at 50 μA cm^{-2}) [46], graphite nanosheets/PANI (77.8 mF cm^{-2} at 0.1 mA cm^{-2}) [47], rGO gel (33.8 mF cm^{-2} at 1 mA cm^{-2}) [48], PANI deposited RGO fibers (66.6 mF cm^{-2} at 0.1 mA cm^{-2}) [49], and PANI deposited carbon nanotube yarn (38 mF cm^{-2} at 10 μA cm^{-2}) [50]. Moreover, GCD curves with various potential windows at a current density of 5 mA cm^{-2} were also studied as shown in **Figure 4.5f**. The results reveal that SASc cell voltage can be extended up to about 2.0 V.

The relationship between energy density (E, Wh cm^{-2}) and power density (P, W cm^{-2}) is described by Ragone plot, and are calculated as:

$$E = \frac{1}{8} C_A (\Delta V)^2 \quad (2)$$

$$P = \frac{E}{t} \quad (3)$$

Where, t is the discharge time (h), C_A is the areal specific capacitance of the SASc (F cm^{-2}), ΔV potential window (V). The energy density of the SASc device reaches 9.07 μW h cm^{-2} at power density of 0.883 mW cm^{-2} and stays 3.45 μW h cm^{-2} at power density of 4.14 mW cm^{-2}. As revealed in **Figure 4.6a**, these values are comparable to that of SASc devices with comparable frameworks reported in the literature such as graphene gel framework (4.66 μW h cm^{-2})[48], non-oxidized graphene multilayer (MLG) paper-PANI (4.10 μW h cm^{-2})[51], PANI 3D microcavity array (11 μW h cm^{-2})[52], chemical vapor deposition derived graphene fibers (1.46 μW h cm^{-2})[53], graphene quantum dots-MnO_2 (0.154 μW h cm^{-2})[54] and graphene/polyaniline woven fabric composite films (0.26 μW h cm^{-2})[55].

The long-term electrochemical stability of the fabricated SASc, evaluated by GCD for 1000 cycles at current density of 5 mA cm^{-2}, was >90.2% (**Figure 4.6b**). To demonstrate its potential

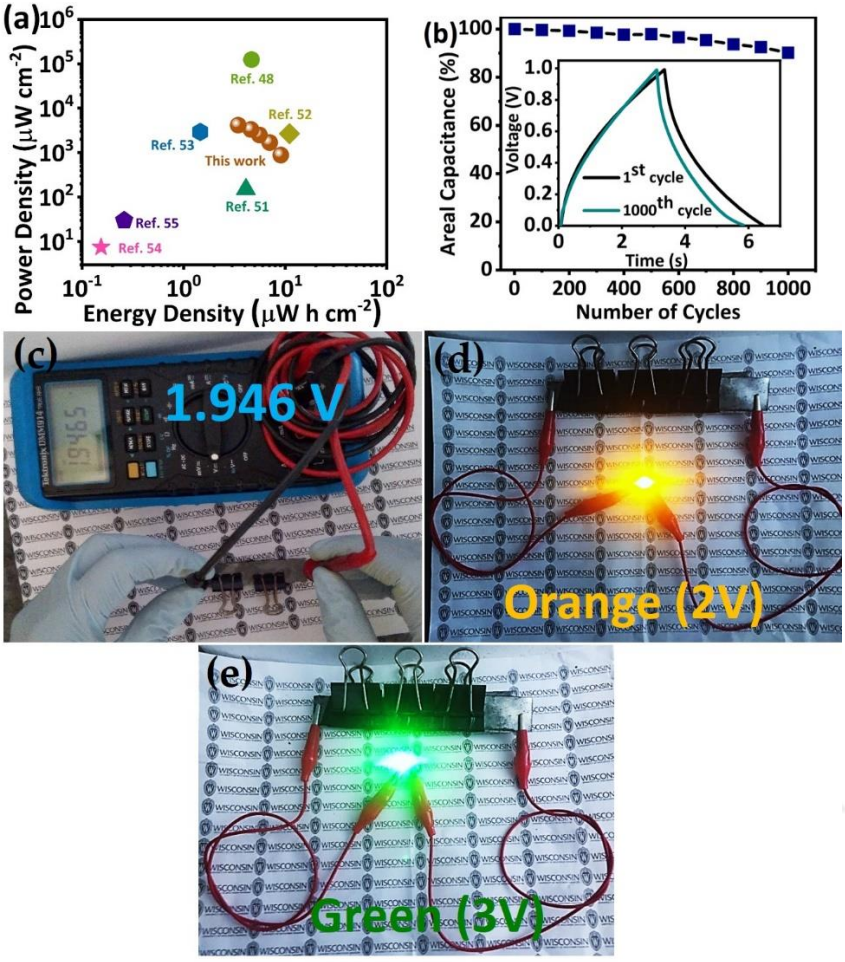

Figure 4.6 (a) Ragone plot comparing the performance of our EG-PANI SASc device with those of graphene-based supercapacitors reported in the literature. (b) Capacitance retention of SASc over 1000 cycles of GCD at current density of 5 mA cm^{-2}. (c) The output voltage (1.95 V) of a fully charged SASc. Two SASc devices connected in series powering (d) orange (forward voltage=2 V) and (e) green (forward voltage =3 V) LEDs being lit for over five minutes without loss of brightness.

application as a power source two such devices were connected in series (forward voltage of a single device= ~1.95 V) as shown in **Figure 4.6c**. The threshold voltage of orange and green LEDs are 2.0 V and 3.0 V, respectively. After charging at 3.5 V for 10 s, our device powered

orange and green LEDs, and they remained lit for more than five minutes without loss of brightness (**Figure 4.6d, e**). This superior performance of EG-PANI is a result of high mobility of electrolyte ions through the nanocomposite, which affords fast electron transport. Connecting several SASc in series and parallel combinations, one could tune the output capacitance and voltage as desired.

4.4 Conclusions

We have developed a facile method to synthesize EG-PANI nanocomposite via one-step interfacial polymerization. The EG retained its sheet-like structure and is surrounded by PANI nanoparticles. A solid-state asymmetric supercapacitor based on the EG-PANI exhibited high areal specific capacitance of 80.4±2.3 mF cm^{-2} at a current density of 1 mA cm^{-2} excellent cyclic stability of 90.2 % after 1000 GCD cycles. The maximum areal power and energy densities of SASc were 4.14 mW cm^{-2} (current density = 5 mA cm^{-2}) and 9.07 µW h cm^{-2} (current density = 1 mA cm^{-2}), respectively. The approach is quickly scalable with improved energy storage efficiency. The discharge form two SASc connected in series, after being charged for 10 s at 3.5 V, can light up different forward voltage LEDs, indicating the SASc can be connected in different parallel and/or series combinations to obtain desired power outputs. The performance of our SASc device suggests the potential of EG-PANI composite for superior energy-storage applications

4.5 Appendix: Chapter IV

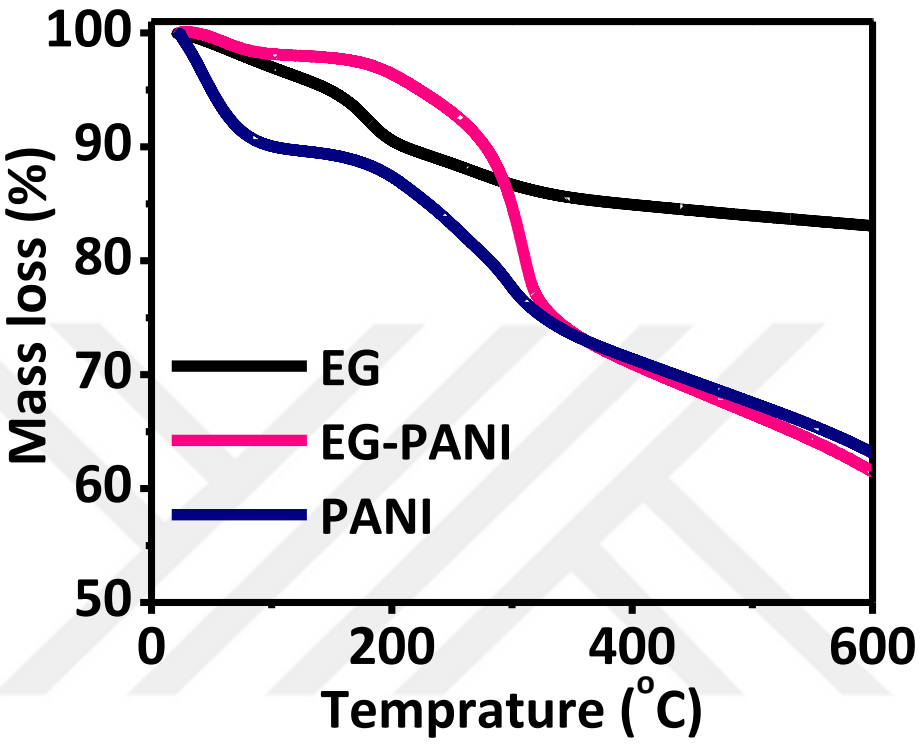

Figure A 4.1 TGA curves for EG, PANI and EG-PANI.

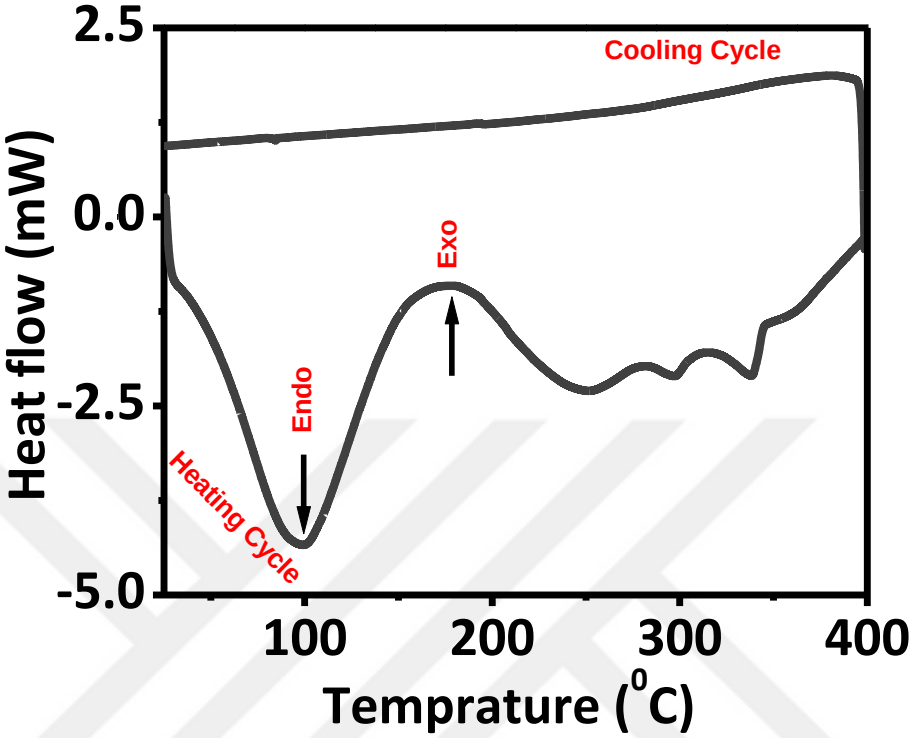

Figure A 4.2 DSC curve for EG-PANI.

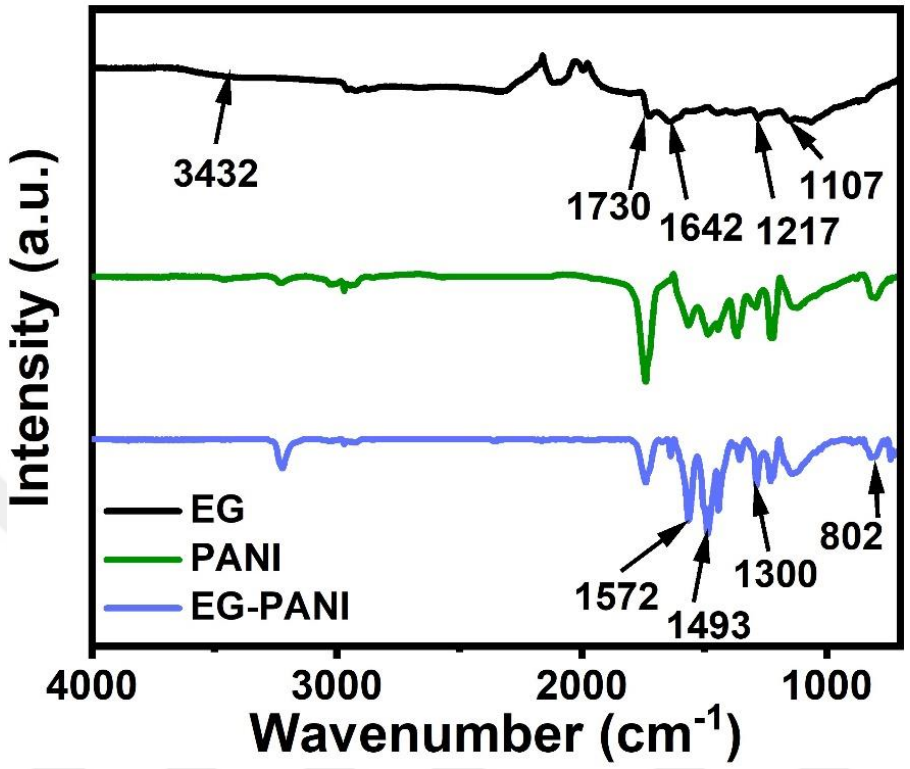

Figure A 4.3 FTIR spectra for EG, PANI and EG-PANI.

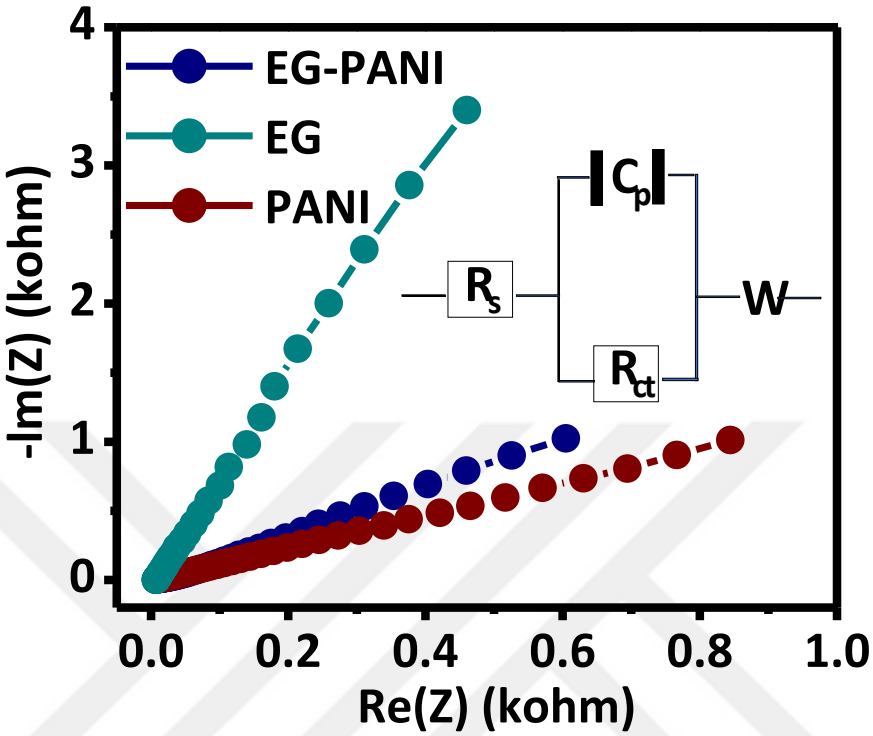

Figure A 4.4 Nyquist plots of EG, PANI and EG-PANI (inset: equivalent circuit).

4.6 References

[1] L.L. Zhang, D. Huang, N.T. Hu, C. Yang, M. Li, H. Wei, Z. Yang, Y.J. Su, Y.F. Zhang, Three-dimensional structures of graphene/polyaniline hybrid films constructed by steamed water for high-performance supercapacitors, J Power Sources 342 (2017) 1-8.
[2] G.G. Jang, B. Song, L.Y. Li, J.K. Keum, Y.D. Jiang, A. Hunt, K.S. Moon, C.P. Wong, M.Z. Hu, Microscopic vertical orientation of nano-interspaced graphene architectures in deposit films as electrodes for enhanced supercapacitor performance, Nano Energy 32 (2017) 88-95.
[3] Z.D. Huang, R. Liang, B. Zhang, Y.B. He, J.K. Kim, Evolution of flexible 3D graphene oxide/carbon nanotube/polyaniline composite papers and their supercapacitive performance, Compos Sci Technol 88 (2013) 126-133.
[4] S. Li, C. Zhao, K.W. Shu, C.Y. Wang, Z.P. Guo, G.G. Wallace, H.K. Liu, Mechanically strong high performance layered polypyrrole nano fibre/graphene film for flexible solid state supercapacitor, Carbon 79 (2014) 554-562.
[5] K. Chi, Z.Y. Zhang, J.B. Xi, Y.A. Huang, F. Xiao, S. Wang, Y.Q. Liu, Freestanding Graphene Paper Supported Three-Dimensional Porous Graphene-Polyaniline Nanoconnposite Synthesized by Inkjet Printing and in Flexible All-Solid-State Supercapacitor, Acs Appl Mater Inter 6(18) (2014) 16312-16319.
[6] M.Y. Yao, X. Zhao, L. Jin, F.Y. Zhao, J.X. Zhang, J. Dong, Q.H. Zhang, High energy density asymmetric supercapacitors based on MOF-derived nanoporous carbon/manganese dioxide hybrids, Chem Eng J 322 (2017) 582-589.
[7] Z. Tong, Y. Yang, J. Wang, J. Zhao, B.L. Su, Y. Li, Layered polyaniline/graphene film from sandwich-structured polyaniline/graphene/polyaniline nanosheets for high-performance pseudosupercapacitors, J Mater Chem A 2(13) (2014) 4642-4651.
[8] X.D. Hong, B.B. Zhang, E. Murphy, J.L. Zou, F. Kim, Three-dimensional reduced graphene oxide/polyaniline nanocomposite film prepared by diffusion driven layer-by-layer assembly for high-performance supercapacitors, J Power Sources 343 (2017) 60-66.
[9] D.W. Wang, F. Li, J.P. Zhao, W.C. Ren, Z.G. Chen, J. Tan, Z.S. Wu, I. Gentle, G.Q. Lu, H.M. Cheng, Fabrication of Graphene/Polyaniline Composite Paper via In Situ Anodic Electropolymerization for High-Performance Flexible Electrode, Acs Nano 3(7) (2009) 1745-1752.
[10] J. Yang, S. Gunasekaran, Electrochemically reduced graphene oxide sheets for use in high performance supercapacitors, Carbon 51 (2013) 36-44.
[11] L. Wang, Y.J. Ye, X.P. Lu, Z.B. Wen, Z. Li, H.Q. Hou, Y.H. Song, Hierarchical Nanocomposites of Polyaniline Nanowire Arrays on Reduced Graphene Oxide Sheets for Supercapacitors, Sci Rep-Uk 3 (2013).
[12] L.F. Lai, H.P. Yang, L. Wang, B.K. Teh, J.Q. Zhong, H. Chou, L.W. Chen, W. Chen, Z.X. Shen, R.S. Ruoff, J.Y. Lin, Preparation of Supercapacitor Electrodes through Selection of Graphene Surface Functionalities, Acs Nano 6(7) (2012) 5941-5951.
[13] M. Niranjana, L. Yesappa, S.P. Ashokkumar, H. Vijeth, S. Raghu, H. Devendrappa, Localized polarons in in situ synthesized polyaniline nanocomposite improve the morphology and the thermal and electrical conductivity, Rsc Advances 6(116) (2016) 115074-115084.
[14] L.Y. Yuan, X.H. Lu, X. Xiao, T. Zhai, J.J. Dai, F.C. Zhang, B. Hu, X. Wang, L. Gong, J. Chen, C.G. Hu, Y.X. Tong, J. Zhou, Z.L. Wang, Flexible Solid-State Supercapacitors Based on Carbon Nanoparticles/MnO2 Nanorods Hybrid Structure, Acs Nano 6(1) (2012) 656-661.
[15] E.H. Jo, H.D. Jang, H. Chang, S.K. Kim, J.H. Choi, C.M. Lee, 3D Network-Structured Crumpled Graphene/Carbon Nanotube/Polyaniline Composites for Supercapacitors, Chemsuschem 10(10) (2017) 2210-2217.

[16] J.L. Shen, C.Y. Yang, X.W. Li, G.C. Wang, High-Performance Asymmetric Supercapacitor Based on Nanoarchitectured Polyaniline/Graphene/Carbon Nanotube and Activated Graphene Electrodes, Acs Appl Mater Inter 5(17) (2013) 8467-8476.
[17] H.H. Wang, J.Y. Lin, Z.X. Shen, Polyaniline (PANi) based electrode materials for energy storage and conversion, J Sci 1(3) (2016) 225-255.
[18] C.H.B. Silva, N.A. Galiote, F. Huguenin, E. Teixeira-Neto, V.R.L. Constantino, M.L.A. Temperini, Spectroscopic, morphological and electrochromic characterization of layer-by-layer hybrid films of polyaniline and hexaniobate nanoscrolls, J Mater Chem 22(28) (2012) 14052-14060.
[19] R.H. Wang, M. Han, Q.N. Zhao, Z.L. Ren, X.L. Guo, C.H. Xu, N. Hu, L. Lu, Hydrothermal synthesis of nanostructured graphene/polyaniline composites as highcapacitance electrode materials for supercapacitors, Sci Rep-Uk 7 (2017).
[20] Q. Wu, Y.X. Xu, Z.Y. Yao, A.R. Liu, G.Q. Shi, Supercapacitors Based on Flexible Graphene/Polyaniline Nanofiber Composite Films, Acs Nano 4(4) (2010) 1963-1970.
[21] C. Meng, C. Liu, L. Chen, C. Hu, S. Fan, Highly flexible and all-solid-state paperlike polymer supercapacitors, Nano Lett 10(10) (2010) 4025-31.
[22] Y. Zhang, L.Y. Zhang, C.W. Zhou, Review of Chemical Vapor Deposition of Graphene and Related Applications, Accounts Chem Res 46(10) (2013) 2329-2339.
[23] T. Yu, P.F. Zhu, Y.C. Xiong, H. Chen, S.H. Kang, H.L. Luo, S.Y. Guan, Synthesis of microspherical polyaniline/graphene composites and their application in supercapacitors, Electrochimica Acta 222 (2016) 12-19.
[24] E. Mitchell, J. Candler, F. De Souza, R.K. Gupta, B.K. Gupta, L.F. Dong, High performance supercapacitor based on multilayer of polyaniline and graphene oxide, Synthetic Met 199 (2015) 214-218.
[25] H.L. Wang, Q.L. Hao, X.J. Yang, L.D. Lu, X. Wang, Graphene oxide doped polyaniline for supercapacitors, Electrochem Commun 11(6) (2009) 1158-1161.
[26] L.L. Wen, K. Li, J.J. Liu, Y.S. Huang, F.X. Bu, B. Zhao, Y.X. Xu, Graphene/polyaniline@carbon cloth composite as a high-performance flexible supercapacitor electrode prepared by a one-step electrochemical co-deposition method, Rsc Advances 7(13) (2017) 7688-7693.
[27] T.J. Fan, S.Z. Tong, W.J. Zeng, Q.L. Niu, Y.D. Liu, C.Y. Kao, J.Y. Liu, W. Huang, Y. Min, A.J. Epstein, Self-assembling sulfonated graphene/polyaniline nanocomposite paper for high performance supercapacitor, Synthetic Met 199 (2015) 79-86.
[28] Z.Y. Gao, F. Wang, J.L. Chang, D.P. Wu, X.R. Wang, X. Wang, F. Xu, S.Y. Gao, K. Jiang, Chemically grafted graphene-polyaniline composite for application in supercapacitor, Electrochimica Acta 133 (2014) 325-334.
[29] X.C. Dong, J.X. Wang, J. Wang, M.B. Chan-Park, X.G. Li, L.H. Wang, W. Huang, P. Chen, Supercapacitor electrode based on three-dimensional graphene-polyaniline hybrid, Mater Chem Phys 134(2-3) (2012) 576-580.
[30] O. Sadak, A.K. Sundramoorthy, S. Gunasekaran, Facile and green synthesis of highly conducting graphene paper, Carbon 138 (2018) 108-117.
[31] M.U.A. Prathap, C.I. Rodriguez, O. Sadak, J. Guan, V. Setaluri, S. Gunasekaran, Ultrasensitive electrochemical immunoassay for melanoma cells using mesoporous polyaniline, Chem Commun 54(7) (2018) 710-714.
[32] K.Q. Qin, J.L. Kang, J.J. Li, E.Z. Liu, C.S. Shi, Z.J. Zhang, X.X. Zhang, N.Q. Zhao, Continuously hierarchical nanoporous graphene film for flexible solid-state supercapacitors with excellent performance, Nano Energy 24 (2016) 158-164.
[33] A. Abdolahi, E. Hamzah, Z. Ibrahim, S. Hashim, Synthesis of Uniform Polyaniline Nanofibers through Interfacial Polymerization, Materials 5(8) (2012) 1487-1494.

[34] N.G. Shang, P. Papakonstantinou, S. Sharma, G. Lubarsky, M.X. Li, D.W. McNeill, A.J. Quinn, W.Z. Zhou, R. Blackley, Controllable selective exfoliation of high-quality graphene nanosheets and nanodots by ionic liquid assisted grinding, Chem Commun 48(13) (2012) 1877-1879.
[35] I.Y. Jeon, L.S. Tan, J.B. Baek, Synthesis and Electrical Properties of Polyaniline/Polyaniline Grafted Multiwalled Carbon Nanotube Mixture via In Situ Static Interfacial Polymerization, J Polym Sci Pol Chem 48(9) (2010) 1962-1972.
[36] M.U.A. Prathap, A.K. Chaurasia, S.N. Sawant, S.K. Apte, Polyaniline-Based Highly Sensitive Microbial Biosensor for Selective Detection of Lindane, Anal Chem 84(15) (2012) 6672-6678.
[37] M.U.A. Prathap, B. Satpati, R. Srivastava, Facile preparation of polyaniline/MnO2 nanofibers and its electrochemical application in the simultaneous determination of catechol, hydroquinone, and resorcinol, Sensor Actuat B-Chem 186 (2013) 67-77.
[38] P. Bhattacharya, S. Dhibar, G. Hatui, A. Mandal, T. Das, C.K. Das, Graphene decorated with hexagonal shaped M-type ferrite and polyaniline wrapper: a potential candidate for electromagnetic wave absorbing and energy storage device applications, Rsc Advances 4(33) (2014) 17039-17053.
[39] P.R. Somani, R. Marimuthu, A.B. Mandale, Synthesis, characterization and charge transport mechanism in conducting polyaniline/V2O5 composites, Polymer 42(7) (2001) 2991-3001.
[40] M. Usman, L.J. Pan, M. Asif, Z. Mahmood, Nickel foam-graphene/MnO2/PANI nanocomposite based electrode material for efficient supercapacitors, J Mater Res 30(21) (2015) 3192-3200.
[41] V. Patil, R.V. Dennis, T.K. Rout, S. Banerjee, G.D. Yadav, Graphene oxide and functionalized multi walled carbon nanotubes as epoxy curing agents: a novel synthetic approach to nanocomposites containing active nanostructured fillers, Rsc Advances 4(90) (2014) 49264-49272.
[42] L.R. Vargas, A.K. Poli, R.D.L. Dutra, C.B. de Souza, M.R. Baldan, E.S. Goncalves, Formation of Composite Polyaniline and Graphene Oxide by Physical Mixture Method, J Aerosp Technol Man 9(1) (2017) 29-38.
[43] O. Sadak, A.K. Sundramoorthy, S. Gunasekaran, Highly selective colorimetric and electrochemical sensing of iron (III) using Nile red functionalized graphene film, Biosens Bioelectron 89 (2017) 430-436.
[44] V. Khomenko, E. Frackowiak, F. Beguin, Determination of the specific capacitance of conducting polymer/nanotubes composite electrodes using different cell configurations, Electrochimica Acta 50(12) (2005) 2499-2506.
[45] L.X. Li, H.H. Song, Q.C. Zhang, J.Y. Yao, X.H. Chen, Effect of compounding process on the structure and electrochemical properties of ordered mesoporous carbon/polyaniline composites as electrodes for supercapacitors, J Power Sources 187(1) (2009) 268-274.
[46] Q.Q. Zhou, Y.R. Li, L. Huang, C. Li, G.Q. Shi, Three-dimensional porous graphene/polyaniline composites for high-rate electrochemical capacitors, J Mater Chem A 2(41) (2014) 17489-17494.
[47] B. Yao, L.Y. Yuan, X. Xiao, J. Zhang, Y.Y. Qi, J. Zhou, J. Zhou, B. Hu, W. Chen, Paper-based solid-state supercapacitors with pencil-drawing graphite/polyaniline networks hybrid electrodes, Nano Energy 2(6) (2013) 1071-1078.
[48] U.N. Maiti, J. Lim, K.E. Lee, W.J. Lee, S.O. Kim, Three-Dimensional Shape Engineered, Interfacial Gelation of Reduced Graphene Oxide for High Rate, Large Capacity Supercapacitors, Advanced materials 26(4) (2014) 615-619.
[49] T.Q. Huang, B.N. Zheng, L. Kou, K. Gopalsamy, Z. Xu, C. Gao, Y.N. Meng, Z.X. Wei, Flexible high performance wet-spun graphene fiber supercapacitors, Rsc Advances 3(46) (2013) 23957-23962.
[50] K. Wang, Q.H. Meng, Y.J. Zhang, Z.X. Wei, M.H. Miao, High-Performance Two-Ply Yarn Supercapacitors Based on Carbon Nanotubes and Polyaniline Nanowire Arrays, Advanced materials 25(10) (2013) 1494-1498.
[51] G. de Souza Augusto, J. Scarmínio, P.R. Catarini Silva, A. de Siervo, C.S. Rout, F. Rouxinol, R.V. Gelamo, Flexible metal-free supercapacitors based on multilayer graphene electrodes, Electrochimica Acta 285 (2018) 241-253.

[52] J. Maeng, Y.J. Kim, C. Meng, P.P. Irazoqui, Three-Dimensional Microcavity Array Electrodes for High-Capacitance All-Solid-State Flexible Microsupercapacitors, Acs Appl Mater Inter 8(21) (2016) 13458-13465.
[53] X.M. Li, T.S. Zhao, Q. Chen, P.X. Li, K.L. Wang, M.L. Zhong, J.Q. Wei, D.H. Wu, B.Q. Wei, H.W. Zhu, Flexible all solid-state supercapacitors based on chemical vapor deposition derived graphene fibers, Phys Chem Chem Phys 15(41) (2013) 17752-17757.
[54] W.W. Liu, Y.Q. Feng, X.B. Yan, J.T. Chen, Q.J. Xue, Superior Micro-Supercapacitors Based on Graphene Quantum Dots, Adv Funct Mater 23(33) (2013) 4111-4122.
[55] X.B. Zang, X. Li, M. Zhu, X.M. Li, Z. Zhen, Y.J. He, K.L. Wang, J.Q. Wei, F.Y. Kang, H.W. Zhu, Graphene/polyaniline woven fabric composite films as flexible supercapacitor electrodes, Nanoscale 7(16) (2015) 7318-7322.

CHAPTER V

5 Conclusions and Perspectives

Graphene and its derivatives are given much consideration as energy storage materials owing to their exceptional properties; high specific and surface area, high electrical and thermal conductivity, lightweight, superior mechanical properties, chemical stability. Therefore, various methods have been developed for cost-efficient and facile synthesis of graphene from graphite: mechanical cleavage, thermal decomposition, chemical exfoliation, and electrochemical exfoliation etc. Among these, electrochemical exfoliation, in this dissertation, is considered a promising approach, which does not require toxic, corrosive oxidizing/reducing agents to produce graphene flakes. Besides, this method is also simple, rapid, inexpensive and feasible for large-scale of production.

In addition, using electrochemically exfoliated graphene suspension, a free-standing flexible graphene paper (GrP) can be formed. GrP has excellent mechanical and electrical properties as well as outstanding electrochemical performance which makes them suitable for multifunctional flexible energy storage devices (Chapter II). Moreover, the addition of a pseudocapacitive material, manganese dioxide (MnO_2), greatly enhances the capacitance behavior of GrP (Chapter III). Furthermore, the addition of a protective conductive polymer shell may further improve capacitance retention as well as specific capacitance, because MnO_2 can partially dissolve in even mildly acidic or near-neutral electrolyte. This polymer layer can also help with mechanical stability and flexibility.

Despite the unique advantages and various preparation methods, graphene sheets tend to form irreversible agglomerates or restack to from graphite due to the strong interactions between π–π

electrons and van der Waals interaction. Theoretically, when the entire surface of single-layer-graphene is fully accessible to electrolyte ions, it shows excellent specific capacitance. Still, due to agglomerates and restacking, the anticipated specific capacitance, which strongly depends on the surface area, is lower than the theoretical value. To achieve high-surface-area graphene and prevent it from agglomerating and restacking to enhance its electrochemical performance, incorporation of spacers such as electrically conducting polymers and metal oxides into graphene is considered the most promising approach. In this dissertation, PANI was utilized as a spacer due to its facile synthesis, low cost, high capacitance, environmental friendliness and redox reversibility. Moreover, PANI wrapped electrochemically exfoliated graphene suspension was directly coated onto a substrate rather than making paper-like structure. The fabricated nanocomposites show high specific capacitance and stable electrochemical performance, indicating a great potential for application in supercapacitors.

There are many opportunities in this thesis for future work and directions which should be pursued. First, the size of GrP prepared in Chapter 2 is limited to size of filtration apparatus. If the appropriate filtration apparatus is used to fabricate large area GrPs, they can be employed to large scale production for supercapacitors, solar panels, or water purifications. Also, when it is used in supercapacitor application, other types of transition metal oxide or conductive polymers can be synthesized and incorporated with GrP to enhance its capacitance behavior. Moreover, in Chapter 4, drop-casting method used to deposit EG-PANI on the current collector surface. The effect of variety deposition methods and current collectors should be further studied, so that it can adoptable to flexible advanced energy storage systems.